# DETECTABILITY OF DISBONDS IN TITANIUM & CARBON FIBRE MATERIAL COMPOSITE — THE CASE OF THE CF-188 INNER WING STEPPED LAP JOINT

# ANALYSE DU JOINT DE RECOUVREMENT DE L'AILE INTÉRIEURE DU CF-188 UTILISANT LA TECHNOLOGIE D'ESSAIS NON DESTRUCTIFS ULTRASONIQUE

A Thesis submitted to the Division of Graduate Studies

of the Royal Military College of Canada

by

Myriam Rochon, RMC

Captain

In partial Fulfilment of the Requirement for the

Masters of Applied Science

September 2021

# Acknowledgements

I would like to thank my supervisor, Dr. Thomas Krause, as well as Dr. Ross Underhill for their patience, guidance and availability. I would also like to thank Steve Savage from QETE and Sgt Adams Smith from ATESS, who not only provided key information and equipment for this project, but without whom many questions would have been left unanswered.

Finally, I would like to thank my family and friends. I consider myself to be lucky, to be surrounded by people who believe in me, who are pushing to be the best version of myself and are always there to support me. Without you all I wouldn’t be here today.

# Abstract

The Inner Wing Stepped Lap Joint (IWSLJ) is a critical primary structure of the CF-188. In the past few years, it has been shown to be prone to disbonds. This thesis focuses on the inspection technique for the IWSLJ, developed in 2015 by the Canadian Armed Forces' Quality Engineering and Testing Establishment (QETE) and Aerospace and Telecommunications Engineering Support Squadron (ATESS). Three potential challenges, as well as areas of improvement are highlighted. First, the heterogeneous nature of the Carbon Fibre Reinforced Polymer (CFRP) makes ultrasonic testing challenging, as ultrasound is easily scattered and attenuated in composites. Second, the geometry of the Stepped Lap Joint adds to the complexity of the inspection. Third, the accessibility to the lap joint, while performing the inspections, makes detection of disbonds on the inner mold line difficult. In this thesis, it is shown that the use of a delay line, currently not included in the inspection procedure, improves the near-surface signal resolution seen in the CFRP and enhances the disbond detection on the inner-mold line. The current procedure is based on detection of complete disbonds, but before a material completely disbonds, an intermediate stage, called a kissing bond, occurs. Although harder to detect, kissing bonds are shown in this thesis, by tension testing, to have a significant impact on bond strength. Therefore, it would be preferable to target detection of disbonds, while they still present as kissing bonds, and before they start to grow and weaken the lap joint further.  No data is available at the moment on disbond growth. Therefore, the use of flat bottom holes as reference standards for this inspection should be reconsidered. If simulated kissing bonds are used instead of flat bottom holes, the likelihood of detecting disbonds, before they fully form, may be enhanced. Ultrasonic data obtained from conventional ultrasonic testing, which is currently not recorded, is compared with results obtained with an automated inspection system, developed by QETE, that records IWSLJ inspection data and allows the user to examine it in the form of an A, B or C-Scan. Signals from artificially produced disbonds in laboratory samples produced in this thesis work are found to simulate signals from real disbonds found on F/A-18 IWSLJ, using the automated inspection system.

# Résumé

Le joint de recouvrement de l’aile intérieure est une partie critique du CF-188. Au cours des dernières années, il fut démontré que le joint est susceptible aux décollements. Cette thèse porte sur la technique d'inspection du joint de recouvrement de l’aile intérieure, développée en 2015 par le centre d'essais d'ingénierie et de qualité et l'escadron de soutien technique en aérospatiale et en télécommunications des forces armées canadiennes. Trois défis potentiels, ainsi que des pistes de solutions sont analysés. Premièrement, la nature hétérogène du matériau composite rend les tests par ultrasons difficiles, car le son est facilement diffusé et atténué. Deuxièmement, la géométrie spécifique au joint de recouvrement ajoute à la complexité de l'inspection. Troisièmement, l'accessibilité au joint de recouvrement lors des inspections rend difficile la détection des décollements sur le joint intérieur. L'utilisation d'une ligne à retard, qui n’est actuellement pas mentionnée dans l’inspection, permet de sortir du champ proche et améliore la mauvaise résolution du signal causée par le composite, et augmente la détection de décollements sur le joint intérieur. La procédure actuelle est basée sur la détection de décollements complets. Mais avant qu'un matériau ne se décolle complètement, une étape intermédiaire, appelée décollement partiel, se produit. Bien que plus difficiles à détecter, il est démontré dans cette thèse que les décollements partiels ont un impact significatif sur la force totale du joint. Aucune information sur la vitesse de propagation des décollements n’est disponible pour l’instant. Par conséquent, il serait préférable de viser à détecter les décollements alors qu'ils sont encore partiels, et avant qu'ils ne commencent à affaiblir davantage le joint. L'utilisation de trous à fond plat comme standard pour cette inspection a donc été reconsidérée. Il serait avantageux d'utiliser plutôt les décollements partiels comme standard, car cela permettrait de détecter plus tôt les points faibles du joint. Les résultats obtenus au moyen de méthode d’essai ultrasonique conventionnel sont comparés aux résultats obtenus avec un système d’inspection automatisé. Des décollements trouvés sur des F/A-18 sont comparés aux résultats obtenus à partir de coupons fabriqués en laboratoire.

# Contents

# List of tables

# List of Figures

# List of Acronyms

| | |
|---|---|
| 1D | One Dimension |
| 2D | Two Dimensions |
| 3D | Three Dimensions |
| Al | Aluminum |
| ARMANDA | Automated Robotic Manipulator Arm for Non-Destructive Assessment |
| ATESS | Aerospace and Telecommunications Engineering Support Squadron |
| CF-188 | Canadian Fighter 188 |
| CFRP | Carbon Fibre Reinforced Polymer |
| CR | Cathode Ray |
| F/ A 18 | Fighter and Attack aircraft 18 |
| FBH | Flat Bottom Hole |
| FMC | Full Matrix Capture |
| IML | Inner Mold Line |
| IWSLJ | Inner Wing Stepped Lap Joint |
| OML | Outer Mold Line |
| PAN | polyacrylonitrile |
| PAUT | Phased Array Ultrasound Testing |
| QETE | Quality Engineering Testing Establishment |
| RAAF | Royal Australian Air Force |
| RCAF | Royal Canadian Air Force |
| TFM | Total Focusing Method |
| Ti | Titanium |
| TOF | Time of Flight |
| UT | Ultrasonic Testing |
| V | Vanadium |

# List of Symbols

| | |
|---|---|
| $c$ | Speed of sound |
| $d$ | Transducer diameter |
| $f$ | Frequency |
| $f_{re}$ | Resonant frequency |
| $f_{rm}$ | Mechanical resonant frequency |
| $k$ | Wave number |
| $t$ | Time |
| $A$ | Amplitude |
| $C_0$ | Electrical capacitance |
| $E$ | Young’s modulus |
| $L$ | Inductance |
| $M$ | Mass |
| $N$ | Near-field distance |
| $P$ | Pressure |
| $R$ | Resonance |
| $S$ | Mechanical Stiffness |
| $Z$ | Impedance |
| $\alpha$ | Attenuation coefficient |
| $\lambda$ | Wavelength |
| $\rho$ | Density |
| $\varphi$ | the angle from the centre axis of the element |
| $\omega$ | Angular frequency |
| $\zeta$ | Damping factor |

# 1. Introduction

Composite materials, like honeycomb sandwich panels and composites made of Carbon Fibre Reinforced Polymer (CFRP) and titanium, are now ubiquitous in aeronautics and many other fields due to their countless advantages, but primarily due to their weight-saving properties in comparison to their relative stiffness and strength. The various processes of binding composite to metal do not require rivets, and this is an advantage from the structural point of view as it reduces the number of sites of potential crack initiation.

However, the use of adhesives is not without risks. It can lead to disbonds and eventually critical failure. Non-destructive inspections are performed periodically with the goal of finding defects before they result in critical failure. But composite materials are difficult to inspect with the current ultrasonic technology. Indeed, fibre reinforced composites, such as CFRP, are notorious for having high acoustic attenuation and high ultrasonic noise [1]. Such structures are synthetically manufactured with heterogeneously arranged materials and/or threads, leading to nonlinear sound transmission [1]. Multiple reflections and interference caused by the multi-layered structure and the signal scattering signal caused by porosity and rich-resin areas can make signal-response difficult to decipher [2]. Choosing the right frequency, and often applying signal processing techniques, are essential to obtaining acceptable results with conventional ultrasound inspection.

Despite these drawbacks, the advantages of adhesives and composite materials outweigh the risks. This is why, in the 1970s, the Inner Wing Stepped Lap Joint (IWSLJ),made of titanium bonded to CFRP,  was selected in the construction of the F-A/18. It's high efficiency and minimal load eccentricity (the impact of applied loads to the joint is felt close to where the load is applied) made it a great choice for the requirements of the US Navy, even though this was one of the first times a bonded joint was used in a critical primary structure [3].

The F/A-18 has become a model of composite structure use. Its entire structure is about 10% composite, compared with 19% for the newer super hornet, most of it being located on the wings [4]. Since the first F/A-18s were introduced in the 1970s by the US Navy, the Royal Australian Air Force, the Royal Canadian Air Force (RCAF), the United States Navy and Swiss Air Force had all acquired operational fleet by the late 1980s. This, of course, means that a lot of effort has been put towards research and development, especially now that the F/A-18 fleet is facing increasing challenges as it approaches the end of its service life, now set for 2032. Between 2002 and 2016, reoccurring disbonds were observed in the

IWSLJ, prompting all countries to begin more careful inspections.  In 2015, the Quality Engineering and Testing Establishment (QETE) and the Aerospace and Telecommunications Engineering Support Squadron (ATESS) developed a non-destructive inspection procedure for the IWSLJ based on conventional piezoelectric Ultrasonic Testing (UT), using a flaw detector EPOCH III© or equivalent. The aim of each periodic inspection is to detect disbonds of the inner wings upper and lower skin carbon fibre / epoxy to titanium outer and inner mold lines (OML and IML), as well as skin ply delamination within the carbon fibre/epoxy solid laminate skin material [5]. In 2019, QETE developed another inspection technique, an automated ultrasonic C-Scan inspection procedure using the TecScan ARMANDA (Automated Robotic Manipulator Arm for Non-Destructive Assessment) technology [6]. Although promising, this new technology is not yet available to all non-destructive evaluation technicians and remains located at QETE.

## 1.1. Objective and Motivation

This thesis focuses specifically on a conventional UT inspection procedure developed in 2015, using the ultrasonic flaw detector EPOCH 600©. Although the EPOCH allows the user to take screen captures of inspection results, it is currently not possible to record in real time entire inspections. Nevertheless, the EPOCH is used in this thesis to examine disbonds at a CFRP-Titanium interface. Results are compared with data obtained from the automated inspection system ARMANDA, which does record inspections and give the user additional ways to look at the data. The impact of kissing bonds on bond strength is looked at through the ASTMD1002- Shear strength of single lap joint [7]. The possibility to detect kissing bonds, either with the EPOCH or the ARMANDA, is investigated.   The relevance of the Flat Bottom Holes (FBH), used in the procedure's calibration block, is also studied. Flat bottom holes have been used for years to simulate defects for calibration and training purposes. There is a general consensus in the industry that FBHs are the best way to simulate most critical defects, such as lamellar defects and cracks. But the most accepted limitation of the flat-bottom-hole standard is its shortcoming in simulating real defects [8]. Disbonds, although similar in many ways to cracks, can behave very differently when appearing as kissing bonds.  This thesis attempts to create artificial kissing bonds, that could then potentially be used in place of FBHs, while helping to identify challenges, and potential solutions, associated with the inspection of the IWSLJ.  Ultrasound behaviour in thin layers of CFRP is alsostudied, as the most critical steps of the IWSLJ have very thin layers of CFRP covering the titanium splice plate.

To summarize, the goals of this thesis are:

1) Investigate the possibility of detecting kissing bonds where only a partial failure of the adhesive has occurred;

2) Evaluate the Epoch UT instrument based inspection against the automated Armanda inspection system; and

3) Examine various ultrasonic parameters including effects of near field inspection, attenuation, transducer frequency and internal reflections affecting the inspection of the IWSLJ.

# 2. Literature Review

The IWSLJ is a fairly complex aircraft part to inspect, not only because it is a composite made of fibre-reinforced polymer and titanium, but also due to its shape. To study the IWSLJ and the current inspection procedure, a good understanding of carbon fibre, epoxy and titanium mechanical and acoustic properties is developed, as well as a basic knowledge of ultrasonic testing. Two common techniques, pulse echo and through transmission, are looked at in detail. The three principal ways of presenting the information obtained from an ultrasonic inspection are explained. Finally, the newest development in ultrasonic technology, such as phased array, full matrix capture and nonlinear ultrasonic inspection are briefly described, as they may enhance or supplement future IWSLJ inspection technologies.

## 2.1. The Composite Material Structure

The CF-188 inner wing stepped lap joint is composed of titanium alloy (Ti-6Al-4V) and a carbon fibre/ epoxy solid laminate.  Figure 1 shows where the joint is located on the upper skin (there is an identical one on the lower skin) and presents a cross-sectional view of the joint, where the steps, the carbon fibre and the titanium are identified. This particular geometry, especially over steps 1 and 2 where the carbon fibre is at its thinnest, has been proven to be subject to disbonds [6] and is closely monitored by the RCAF and ATESS via periodic inspections.

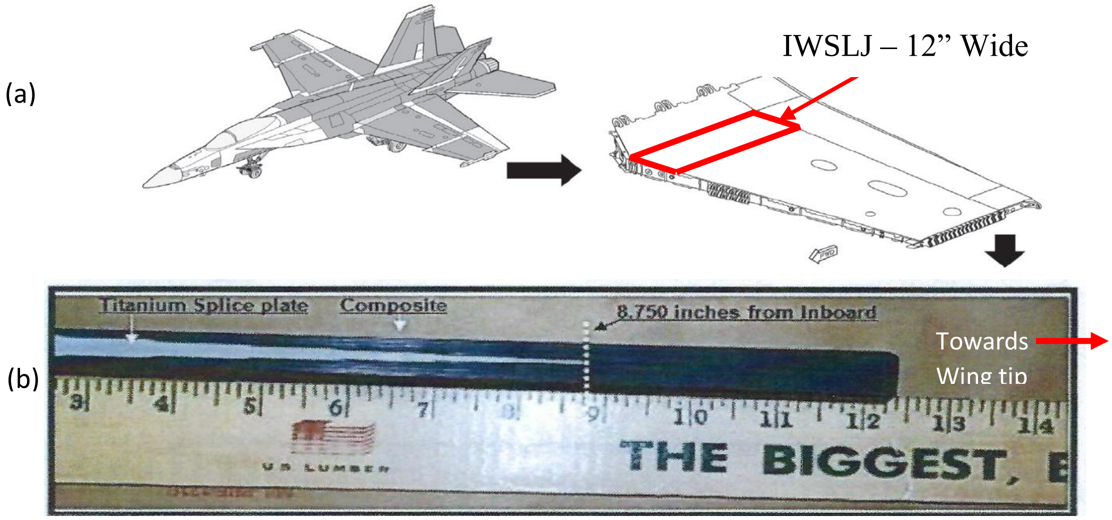

Figure 1. (a) Location of the upper wing IWSLJ on the CF-188 and (b) cross-Sectional view [6].

## 2.2. Disbonds and Delamination

Despite all the advantages of composite structures, the use of adhesives is not without risks. A disbond is the failure of an adhesive (FM-300 film adhesive in the case of the lap joint) to properly adhere to an adherent (titanium — carbon fibre / epoxy), while delamination is the failure of some of the layers within the fibre-reinforced polymer itself to properly adhere together. These types of defects can have a detrimental impact on the structural integrity of any part where composites are used, as will be discussed in Section 2.5. Therefore, it is important to understand how disbonds and delaminations form and the impact they can have on the structural life of a component. The diagram presented as Figure 2 shows potential causes of disbonds and highlights that the three most common are the condition of the raw material, operators, and equipment or related technical problems [9]. Disbonds caused by the raw material condition can be explained mostly by the quality of the material. For example, if the quality of the material is poor and a crack initiates within it, it could lead to disbonds when the crack reaches the surface, where the adhesive is present. The state of the surface at the moment of adhesion can also lead to disbonds, if moisture is trapped, for example. Since the appearance of disbonds is unpredictable, periodic non-destructive evaluations are important so that defects can be detected before they can grow to a critical length.

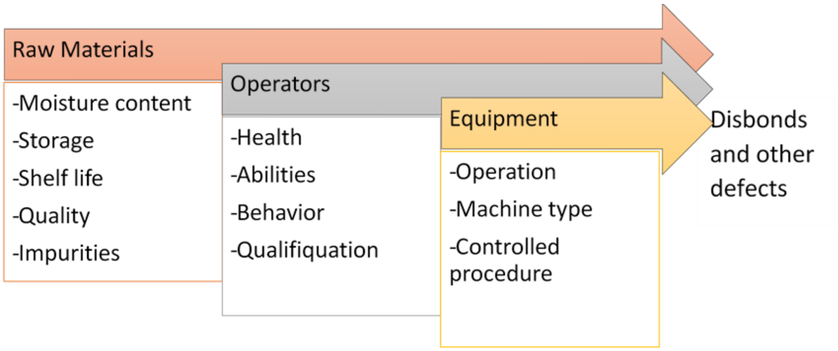

Figure 2. List of possible causes of Disbonds.

When looking at Figure 1, it is obvious that more composite is present towards the wing tip, while the thickest part of the titanium is closer to the fuselage. Knowing that the CF-188 wings will “flap” up and down as it flies, the thin composite area closest to the fuselage is more at risk of disbonding, due to a lever effect. In this specific case, delaminations are possible, because, as will be explained in Section 2.4.2, the forces acting on the wing will not be parallel to the carbon fibres, but they are not orthogonal either. The total strength of the composite might be affected by these forces slightly, but the biggest risk in the case of an aircraft wing would be damage caused by impact. Bullets, birds, or even other aircraft, are all possible risks for the composite’s integrity.

A stress analysis of the stepped-lap joint, explored in detail in Section 2.6, yields the following conclusions: the joint consists of a series of single-lap joints and has a nonuniform shear stress distribution with high stresses at the ends of each step. One key factor to the origin of the shear stresses, other than the geometry of the lap joint, is the stiffness imbalance [4] between the carbon fibre/epoxy composite (E=141 GPa [10]) and the titanium (E=114 GPa [5]), a stress distribution is generated in the adhesive, as pictured in Figure 3 [4]. The end step (Step 9, pointing towards the wing tip) was designed to account for the higher-than-average load transfer, overloading and to prevent failure at the end of the overlap. The outermost step (Step 1, closest to the fuselage) was designed to be sufficiently thin to reduce peel stresses and to prevent interlaminar tension [4]. In addition to the end step and the outermost step, the other factor that could enhance joint performance is the length of the overlaps. However, it was demonstrated that the load-carrying capability of a stepped-lap joint cannot be improved indefinitely by increasing the overlap length [4]. The middle steps (Steps 2 to 6) significantly contribute to the load transfer, hence increasing the joint efficiency, when compared to load transfer in the middle of a uniform lap joint [4].

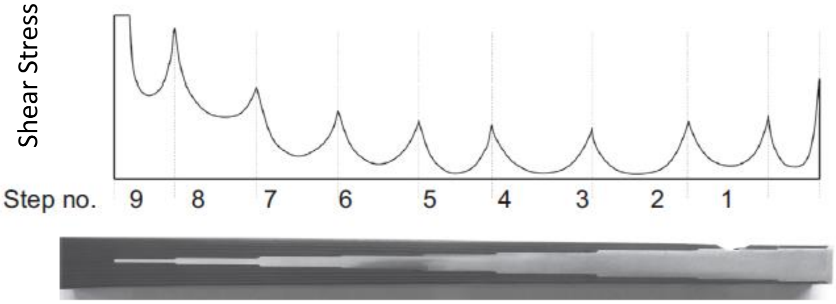

Figure 3. Representative adhesive shear stress distribution for stiffness unbalance in stepped lap joint [4].

Another important factor, not mentioned in the studies introduced in Section 2.6, is the formation of kissing bonds. By definition, kissing bonds are similar to a complete disbond, in the sense that they are characterized by partial failure of the adhesive holding two adherents together, instead of complete failure of the adhesive as occurs for full disbonds. This suggest, as this thesis will show, that kissing bonds are harder to detect, while having a critical impact on bond strength. Figure 4 below illustrates the difference between a kissing bond and a disbond on the bond line.

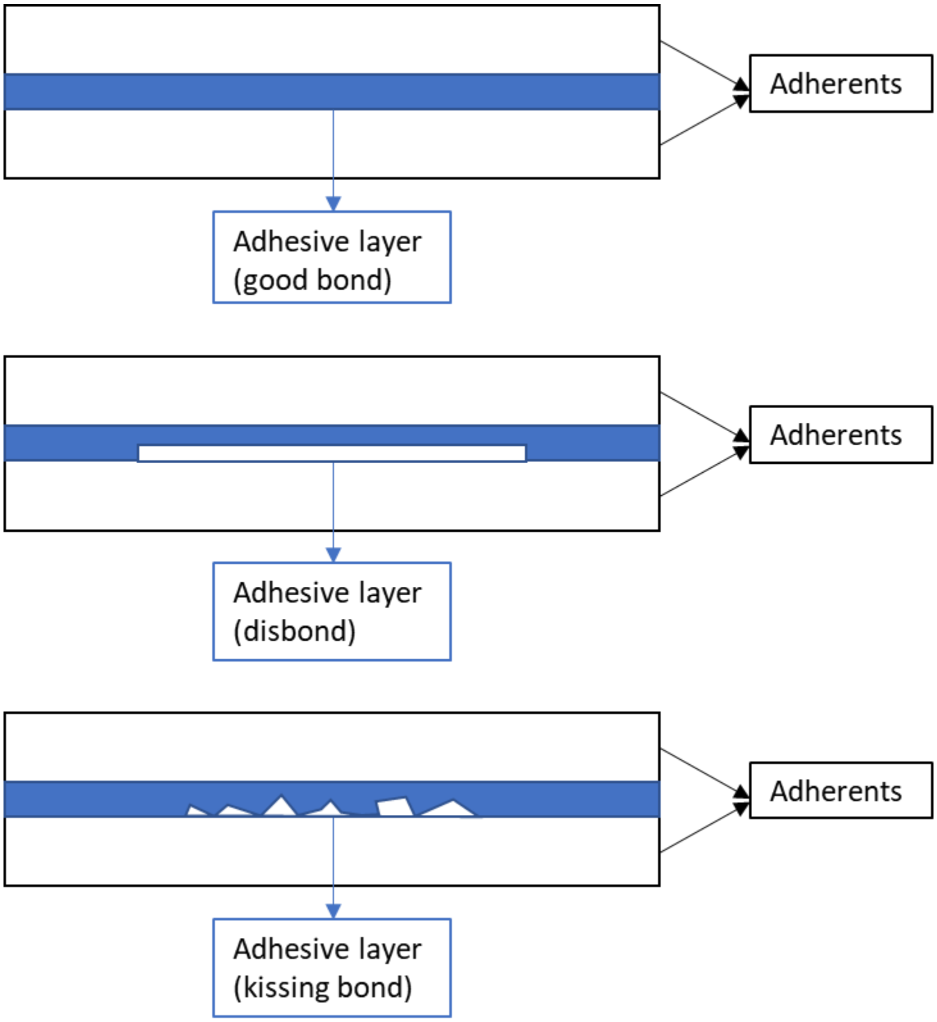

Figure 4. Representation of a good bond, a disbond and a kissing bond.

## 2.3. Properties of Titanium

Titanium based alloys really started to be considered a key material of aircraft engines after the Second World War, because of its high strength-to-weight ratio. It eventually became useful for aircraft structure as well. The Dupont company was the first to commercially produce titanium, starting in 1948. Even today, the aerospace industry is still the main consumer of titanium [11]. There exists now more than 100 titanium alloys, but only 20 to 30 have been commercialized. Of these, Ti-6Al-4V (6%wt Aluminum, 4%wt Vanadium) covers more than 50% of commercial usage. Another 20 to 30% are unalloyed titanium. In fact, Ti-6Al-4V, also referred to as Grade 5, is by far the most common alloy and can mostly be found in the aerospace industry for structural parts subject to variable loads and high cyclically changing strain rates [12] such as the lap joint, but also in medical applications, for implants and prostheses due to its high corrosion resistance and strength-to-weight ratio.

Titanium is more ductile than carbon fibre, and will plastically deform before breaking, whereas fibres are stronger, but also more brittle. As will be discussed later, the difference in the elastic moduli can cause problems when titanium is bonded to the stiffer fibre-reinforced composite, subject to active stresses.

## 2.4. Properties of Carbon Fibre Reinforced Polymer

Fibre reinforced polymers are common, and mostly dependent on the type of fibres chosen for their assembly. However, the polymer matrix still has an important role to play in the mechanical properties of the finished composite, and this is why each component of the composite is looked at separately below.

### 2.4.1. Carbon Fibre

The properties of carbon fibres are highly dependent on the fibre structure. At ambient conditions, stable crystalline carbon is known as graphite [13], but carbon fibres are usually not totally crystalline. The areas of non-crystallinity do not present the three-dimensional ordered arrangement of hexagonal carbon networks that is characteristic of graphite [13]. This causes a disturbance among the layers and creates imperfect alignments, resulting in complex-shaped voids that act as stress raisers and points of weakness leading to a reduction in strength properties [14].

Chung [15] compared three different types of fibres. Two pitch-based carbon fibres, Thornel (P-100 and P-120) by Performance Products and Carbonic (HM50, HM60, HM80) by Kashima Oil **Co** and one PAN-based carbon fibre, made by Toray. Commercial carbon fibres are made only with pitch or polyacrylonitrile (PAN) as the precursor. However, the manufacturing process is different for each and gives the fibres different mechanical properties. The main difference being that PAN fibres are wet-spun and pitch fibres are melt-spun [15].

Chung [15] provided the following table in her book, as a way to compare two pitch-based and one PAN based carbon fibre. However, since the PAN-based carbon fibre AS4, manufactured by Hextow® is the one being used on the F/A-18 [4], its properties [16] were added to Table 1 for comparison purposes.

Table 1. Mechanical properties of various pitch and PAN based carbon fibres

| | Sample Name | Tensile Strength (GPa) | Tensile Modulus (GPa) | Elongation (%) |
|---|---|---|---|---|
| Pitch based | Thornel P-100 [15] | 2.2 | 690 | 0.3 |
| | Carbonic HM50 [15] | 2.8 | 490 | 0.6 |
| PAN based | Torayca M46 [15] | 2.4 | 450 | 1 |
| | HexTow AS4 [16] | 2.3 | 231 | 1.8 |

From Table 1, it can be observed that all fibres are low strength, except for Carbonic, which has a superior crack resistance due to its folded layer structure. The PAN based fibres have a lower tensile modulus, due to the fact that PAN is not as graphitizable as pitch [15]. Since fewer oriented fibres tend to exhibit greater degrees of elongation, it explains why the two PAN-based fibres present the highest percent elongation.

### 2.4.2. Polymer Matrix Carbon Fibre Composite

Many materials can be used as a matrix for fibre composites, including metals and ceramics. Of all possible options, polymers are probably the cheapest and the easiest to manufacture [15]. Among polymers, epoxy is perhaps the most common choice and is the one being used with the AS4 fibres on the CF-188. Epoxy has an excellent combination of mechanical properties and corrosion resistance, is dimensionally stable, exhibits good adhesion, and is relatively inexpensive [15].

The matrix serves several purposes. It acts as a protective coating for the fibres; Thermosets like epoxy have a low molecular weight in liquid state, before curing, allowing for a greater mobility during processing so that the resins can quickly wet the surface of the fibres [15]. The resin then protects the fibres from mechanical abrasion or chemical reaction with the environment, while also separating them from one another [13]. More importantly, the matrix binds the fibres together, thus serving as a medium by which external stresses are transmitted and distributed to the fibres [13]. Only a very small portion of the stress will actually be carried by the matrix, under the condition that the adhesive bond between the fibre and the matrix is high. The strength of the bond will prevent fibre pull out and maximize the transmission of the stresses between the relatively weak matrix and the strong fibres. However, this also means that fibre-reinforced polymers are strongest in the direction of the fibre. Most fibres composites do not provide reinforcement through the thickness and are dependent on their matrix to carry loads in that direction, but matrices are not nearly as strong as the fibres [17]. In the case of the F/A-18, the AS4 carbon fibres have a modulus of 33.5 msi (231 GPa) [16], while the epoxy has a modulus of approximately 615 ksi (4.2 GPa) [10]. This means that transverse stresses are more likely to result in defects inside a composite, such as delamination, as will be discussed in Section 2.5. Figure 5 shows the impact of off-axis loading on the maximum strength of AS4/3501-6 graphite/epoxy [17]. The further from the longitudinal axis the loading is, the weaker the material becomes. This also means that the direction of the fibres will matter when a fibre-reinforced polymer is adhered to another component. In the case of the Stepped lap joint, the use of 0° plies at the interface has shown to increase the joint efficiency and minimize premature adherent failure due to transverse microcracking [4]. In other words, the fibres have to be lined up with the titanium in such a way as to absorb and distribute most of the load the structure will endure.

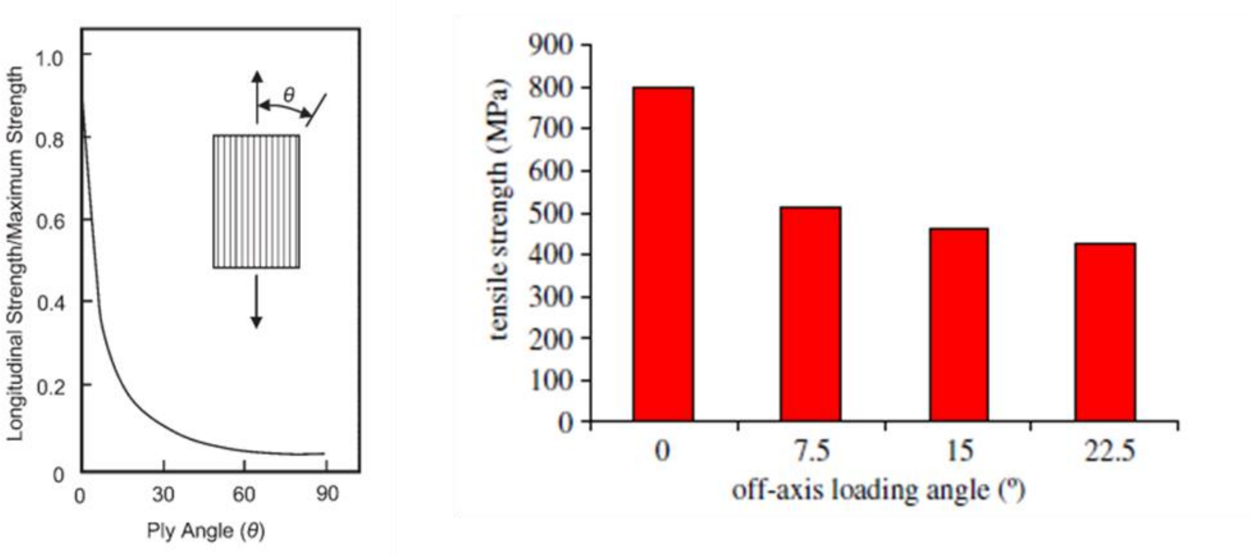

Figure 5. Impact of off-axis loading on tensile strength on CFRP (a) as a function of ply angle [18] (b) tensile strength of AS4/Epoxy CFRP vs. loading angle [17].

## 2.5. Flexible Adhesives in Bonded Structures

There exist an incredibly large variety of adhesives. Kuczmaszewski [19] in his book on metal-to-metal adhesive bonding, lists 25 different families, ranging from starch adhesives to bond paper and cardboard to silicon adhesives used in bonding transformers and other pieces of equipment operating at high temperature [19]. The varieties that are of interest for this thesis are the epoxy adhesives, used to bond metals, ceramics, glass, concrete, wood, rubber and polymer plastics [19]. In some cases, epoxy resins can also be used to bond fibres of a fibre-reinforced polymer, as described in Section 2.4.2.

One the most acknowledged benefits of adhesive joining over riveting is its weight saving property. But one of the key advantages of adhesives reside in their superior fatigue resistance. Adhesively bonded structures have been proven to have a fatigue life up to twenty times better than riveted structures on otherwise identical parts [20]. Epoxies are also characterized by good strength properties and chemical resistance once cured, rendering them inert to most media, and are thus approved for use in the food processing industry [19]. But mainly, epoxies are known for the possibility of bonding small elements, the facility of joining large surfaces relatively quickly, while simultaneously sealing the assembled structure. The equipment required to perform joining is simple, which also means cost effective [19]. However, cured epoxy resins are often sensitive to their environment. They present a high capacity of water uptake, and exposure to high temperature causes a reduction in strength [21]. The behaviour of adhesive joints depends on many different factors. The environment, but also the specific type of epoxy used, as well as the nature of the adherent, will affect the properties of the bond. Therefore, researchers agree [19, 21] that each structure has to be studied separately.

### 2.5.1. Adhesive Properties and Modes of Failure

The strength of an adhesive bond can be attributed to four factors; 1) surface roughness, which increases the effective area being bonded, 2) the interdiffusion of molecules between adhesive and adherent increasing the strength of the bond, 3) weak molecular attraction allowing for good wetting properties, as described in Section 2.4.2, and finally 4) adsorption, which is a combination of weak molecular attraction and chemical bonds between the adhesive and the adherent [22]. Adsorption is the reason why adhesive bonds sometimes seem to have high bond strength, but end up having a short service life. The chemical bonds that make the joint appear so strong initially are easily broken by hydration, especially if the surface was not adequately prepared [22].

Indeed, surface preparation is probably the most critical step to ensure the durability of the bond [22]. It can increase bond strength by three different methods; 1) by increasing surface tension, 2) increasing surface roughness, which in turn increases the surface area and allows the adhesive to flow around all the irregularities on the surface, or 3) changing surface chemistry in order to create chemical bonds between the metal oxide layer and the fibre-reinforced polymer molecules [23]. There exist a wide range of techniques to prepare adherents for bonding, and while some may provide adequate static strength, they may have little durability when exposed to heat and humidity. Other methods may be more prone to disbonds when exposed to harsh environmental conditions, such as heat and moisture [23]. But no matter the surface treatment, no bond is unbreakable. Research has shown over the years [4, 19, 20, 24] that adhesive bonds can fail three different ways; (1) adhesively, (2) cohesively or (3) through a mixed mode of failure

Adhesion failure is typically observed when a true disbond is present in the bond line. The adhesive remains entirely on one surface, and its surface is often very smooth. Adhesion failure is caused by the chemical bond at the interface becoming too weak, contamination during manufacturing, the use of an adhesive past its shelf life, or possibly inadequate curing temperature or temperature control during manufacturing. It results in a weak bond that may break with only a small load applied to it [25].

Cohesion failure is a sign of a strong adhesive, and usually happens due to high shear or peel stresses. Adhesive is usually present on both adherent surfaces, and may appear rough. This type of failure is more often seen when performing lap shear tests such as the ASTMD1002 or peel tests like ASTM D1781-76 [7]. If such failure is observed in service life, it may be caused by an insufficient overlap length, excessive stresses, or possibly too much porosity in the adhesive itself. A higher void content could lead to a higher exposure to moisture of the pre-cured adhesive [22].

The third mode of failure is called mixed-mode failure, and is a combination of adhesive and cohesive failure. This is perhaps the mode of failure that is the most difficult to assess, as the surface degradation leading to failure usually happens over time. Therefore, many factors can cause mixed-mode failure. It is sometimes possible for bonds to look as though they failed in mixed modes, where a partially degraded bond could be subject to high load. The weak part would fail in adhesion, and the remainder of the bond would be overloaded and give the impression to have failed cohesively, when in fact it failed adhesively [22]. Bonds that are more sensitive to moisture are likely to fail by mixed-mode failure, as bond strength will degrade over time, and will degrade more where hydration has been more severe. Eventually the bond becomes too weak and fails completely. The main concern, is that in contrast to disbonds, this cannot be detected by current NDT techniques [25].

Substrate, or adherent failure, is considered by some the fourth mode of failure and is more commonly seen when using composite materials. In this case, the adhesive layer remains perfectly intact, but the adherent will fail first, most likely due to the same shear and peel stresses that were mentioned for cohesion failure [4].

## 2.6. The Case of the F/A-18 IWSLJ

The Royal Australian Air Force (RAAF), as being one of the operating fleets of the F-A/18, took interest in the disbond behaviour of the lap joint. Early studies focused on 1D static strength, and a more recent study focused on finite element method modelling, the impact of different disbond configurations on the overall joint carrying capability [3]. More specifically, they looked at disbonds covering the full width of one and two steps at a time and disbonds covering a third of the width, in the middle, of one and two steps at a time [3]. Note that when two steps were considered at the same time, it was assumed to be Steps 1 and 2, as they are more prone to disbonds.

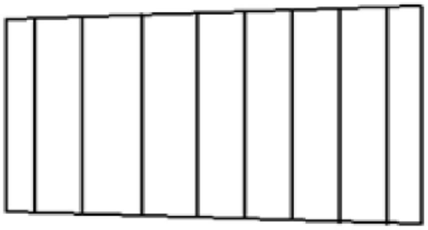

(a) Pristine

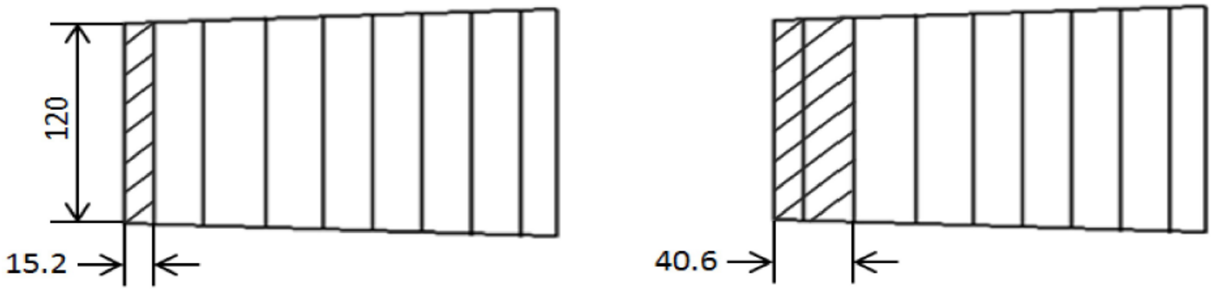

(b) One step, full width disbond (FS1)    (c) Two steps, full width disbond (FS2)

(d) One step, middle disbond (MS1)    (e) Two steps, middle disbond (MS2)

Figure 6. Disbond configuration for full width and middle disbonds, covering Steps 1 and 2 [3].

The major conclusions from their study are that an increase in disbonded area reduced the ultimate load of the bond, but that partial width disbonds over two steps had an ultimate load 45% higher than full width disbonds over two steps [3]. The partial width disbonds, more representative of what is likely to be found on a real aircraft, were found to grow even quicker than the full width disbonds, reaching as far as Step 5 before failure [3].

However, it should be noted that the RAAF analysis was done under static loading. A fatigue analysis of the lap joint was done in the United States by Senevirtne et al. [4]. They extracted all their test specimens from wing skins belonging to decommissioned F/A-18 aircraft wings (models A-D) supplied by the U.S. Navy. Since the wings had experienced fatigue cycles ranging from a half lifetime to one lifetime of fleet service, and that samples were taken at multiple locations along the joint, on the upper and lower skins, they ensured their results would provide useful information with regards to life extension prediction for the remaining aircraft.

Although the lap joint in itself is bonded by adhesive, there are still fasteners present on the wing skin. Therefore, some of the specimens extracted inevitably had fasteners holes, while others had no holes at all. Senevirtne et al. [4] chose to leave some of the fasteners in position and referred to those samples as filled holes, and removed some, creating open hole samples [4]. The spectrum used for their tests represents 300 Spectrum Fatigue Hours, and was normalized due to the variation of thicknesses across samples, but was based on flight-by-flight loading of the wing root [4]. Twenty-one specimens were tested with a tension dominant spectrum and 13 with a compression dominant one. Specimens that survived 10 lifetimes of tension cycling and 30 lifetimes of compression cycling respectively, were then tested for residual strength. Six specimens survived the tension dominant fatigue spectrum out of 21 (29%), and 10 survived the compression dominant fatigue spectrum out of 13 (77%) [4]. Not surprisingly, only three specimens in tension with filled fastener holes didn't have fatigue failure and all specimens with open fastener holes failed during testing due to fracture across the fastener hole. All of the specimens with no holes, bonded only by adhesive, survived the 10 lifetimes without any problems [4].

It is known that the number of plies has an impact on the mode of failure when an open hole is present [17]. Given the varying thickness of the carbon fibre composite in the lap joint, it is likely that failure would occur by fibre failure over Steps 1 and 2. The hole cut in the composite prevents the fibres from properly distributing the load and could result in failure of the actual fibers. If not, then delamination over Steps 8 and 9 is the most probable mode of failure.

In the case of the filled holes, the titanium was affected more than the composite. The fastener holes acted as a stress concentrator, which initiated fatigue crack growth in the titanium. But the load-bearing capacity of the joint was less affected compared to the open-hole case. The titanium was more affected than the epoxy because the epoxy matrix in the fibre-reinforced polymer usually distributes the load across the fibres better than rivets do. But the presence of the rivet still helped distribute the load, possibly explaining why the load-carrying capacity of the joint was not affected compared to the open fastener holes.

Three main failure modes were identified for the inner wing stepped lap joint [4] ; (1) cohesive failure, caused by a failure of the adhesive itself due to an inability to resist internal separation (adhesive should be present on both sides) (2) adhesive failure due to improper bonding of the adhesive with the surface, i.e. disbonds, more likely to occur under high shear stresses,  and (3) adherent failure, where the adhesive was still intact, but the adherent nonetheless failed. In composite materials this would typically mean delamination. It comes as no surprise that disbonds and delaminations were among the two most common cause of failure for the stepped lap joint. These modes of failure are not only typical to the IWSLJ, but are in fact typical to all adhesively bonded structures.

When looking at the data collected both by the RAAF [3] and by Senevirtne et al. [4], it can be concluded that the IWSLJ was well designed and can likely operate past its expected useful life. However, it was concluded by Senevirtne et al. [4] that disbonds and delaminations are among the main modes of failure of the lap joint, and the RAAF showed that disbonds can grow rapidly and significantly impact the load bearing capacity of the joint. This highlights the importance of the work being done in this thesis; detecting disbond early could possibly prevent them from spreading further and becoming a safety concern.

# 3. Mathematical Principles for Ultrasonic Inspection

Wave behaviour, be it in one or three dimensions, has been studied for a long time. It started with the introduction of differential calculus by Newton, but Brook Taylor was among the first mathematicians to advance theories on vibrating strings, proposing his work to the Royal Society in September of 1712 [26]. Herman, Bernoulli and Euler picked up interest in his work and made contributions towards the vibration theory that is known and accepted today [26].

The equation for a plane wave travelling in the x-direction is given as [27]:

$$\frac{\partial^2 y}{\partial x^2} = \frac{k^2}{\omega^2}\frac{\partial^2 y}{\partial t^2}. \tag{3.1}$$

Where x and y are coordinates of the plane, k is the wave number and ω is the angular frequency. The Helmholtz equation, which often arises when studying problems with partial differential equations, like the wave equation, represents the time-dependent form of the equation [28] and has the form:

$$\nabla^2 f = -k^2 f. \tag{3.2}$$

Where f represents a function and k is the wave number. The wave equation does not only apply to acoustics. It also applies to fluid mechanics, electromechanics, optics, and many more fields of study. In this section, the Fourier transform, which is an essential tool to switch between time and frequency domain, the delta function, which is useful in acoustics to represent an impulse function, as well as the Green function will be discussed next.

## 3.1. Fourier Transform

Named after French mathematician Joseph Fourier, the Fourier transform is a mathematical technique that transforms a function of time, f(t), to a function of frequency, F (ω). It is commonly used in signal filtering and analysis, as well as image reconstruction and compression [29]. The transform is actually a special case of the Fourier Series, where the function f(x) is expanded in a series of complex exponentials [30]:

$$f(x) = \sum_{r=-\infty}^{+\infty} c_r e^{-irx} . \tag{3.3}$$

Where $c_r$ is defined as [30]:

$$c_r = \frac{1}{2\pi}\int_{-\pi}^{+\pi} f(x) e^{-irx} dx , \qquad r = 0, \pm 1, \pm 2, \dots \tag{3.4}$$

By substituting the variable x for $\pi u/L$, where L is an arbitrary length and u is a variable, the interval of the integral is changed from ±π to ±L so that equation 3.4 becomes [30]:

$$c_r = \frac{1}{2L}\int_{-L}^{+L} f(u) exp\,(i\frac{r\pi u}{L}) dx . \tag{3.5}$$

Substituting equation 3.5 back into equation 3.3 gives [30]:

$$f(x) = \frac{1}{2L}\sum_{r=-\infty}^{+\infty}\int_{-L}^{+L} f(u)\, exp\left[-i\frac{r\pi}{L}(x-u)\right] du. \tag{3.6}$$

Let $\frac{r\pi}{L} \rightarrow k$ ; $\sum_{r=-\infty}^{+\infty} \rightarrow \int_{-\infty}^{+\infty} dk$ with $dk = \frac{\pi}{L}$ and $L \rightarrow \infty$.

Equation 3.6 becomes [30]:

$$f(x) = \frac{1}{2\pi}\int_{-\infty}^{+\infty} e^{-ikx}dk \int_{-\infty}^{+\infty} f(u)e^{iku}du\,. \tag{3.7}$$

So that [30]:

$$f(x) = \frac{1}{2\pi}\int_{-\infty}^{+\infty} F(k)e^{-ikx}dk \quad ; \tag{3.8}$$

$$F(k) = \int_{-\infty}^{+\infty} f(x)e^{ikx}dx \quad . \tag{3.9}$$

which are the equations for the inverse Fourier transform and the Fourier transform, respectively, used to transform a time function f(x) into a frequency function, F(k) [30].

## 3.2. Dirac Delta Function

The Dirac delta function (δ) is used in many branches of physics. In signal analysis, the one-dimension delta function is also known as the impulse function [31]. The function is defined as being infinitely high at x=0 and 0 everywhere else [27]. In terms of signal analysis, it is defined as [31]:

$$\delta(t) = \begin{cases} 0, & for \;\; t \neq 0 \\ \frac{1}{T}, & for\; t \leq T, \end{cases} \tag{3.10}$$

and the area under the “spike” formed by the function at t=0 must be equal to 1 such that [27]:

$$\int_{-\infty}^{+\infty} \delta(x)dx = 1\,. \tag{3.11}$$

If the pulse is rectangular, of length T and of constant amplitude 1/T, then the area under the pulse remains 1 [31]. Graphically, the one-dimensional Dirac delta function can be represented as shown in Figure 7:

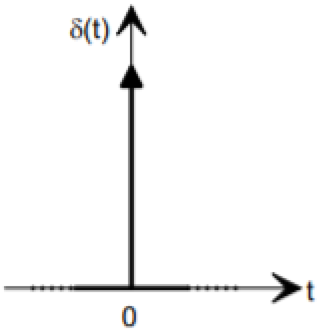

Figure 7. The impulse function at t=0 [31].

Technically speaking, it is not accurate to call the Dirac Delta function a function, because it is not finite. It would be more appropriate to call it a generalized function or a distribution [27]. But the definition has been widely accepted. If the impulse does not occur at x=0, then the signal is shifted, such that an impulse occurring at time t=a is denoted as $\delta\ (t-a)$ [31]. This allows the property of "shifting" or "sampling", where the integrand multiplied by the time shifted impulse is "shifted" out at the time of the occurrence:

$$\int_{-\infty}^{+\infty} f(t)\delta(t-a)dt = f(a)\,. \tag{3.12}$$

This property is used Section 3.4.2, in the derivation of the Rayleigh Sommerfeld Integral, the sound pressure radiating from the transducer is considered from an ideal point-like target, which would see the pressure coming as an impulse function.

The shifting property also applies to the Fourier transform of the Dirac delta function such that [31]:

$$F[\delta(t)] = \int_{-\infty}^{+\infty} \delta(t)e^{-i\omega t}dt = 1\,. \tag{3.13}$$

## 3.3. Green's functions

Green's functions are impulse responses that are used to solve differential equations, from the ordinary differential equation, to more complex, inhomogeneous equations with varying boundary conditions. They are particularly useful in applied mathematics, physics and engineering [32]. A Green's function $G = G\ (x,s)$ of a linear differential operator $\mathcal{L} = \mathcal{L}\ (x)$, acting on distributions over a subset of the Euclidean space $\mathbb{R}^n$, at point s is the solution to:

$$\mathcal{L}G(x,s) = \delta(x-s). \tag{3.14}$$

Where $\delta$ is the delta function. The Green's function that is of interest for this thesis, and becomes useful in the derivation of key equations in Section 3.4, is the Green's function for the inhomogeneous Helmholtz equation, which has the form:

$$(\nabla^2 + k^2)A(x) = -f(x). \tag{3.15}$$

With $A(x) = (G * f)(x)$. It follows that the Green's function required to solve the partial differential equation is:

$$(\nabla^2 + k^2)G(x, x_0) = \delta(x - x_0). \tag{3.16}$$

The solution to G is not trivial and can take more than one form. However, the one relevant to this project and used in Section 3.4 has the form:

$$G(x, x_0) = -\frac{e^{-ik|x-x_0|}}{4\pi|x-x_0|}. \tag{3.17}$$

## 3.4. Rayleigh Sommerfeld Theory

Consider an arbitrary volume V of a fluid medium and its closed surface S [33], where n(x$_x$) is a normal vector to the surface as pictured in Figure 8:

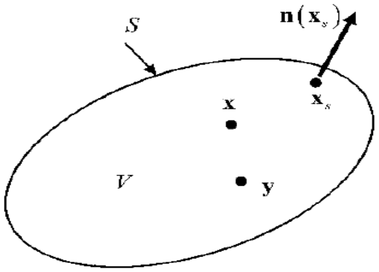

Figure 8. An arbitrary volume V and its surface S for application of the reciprocal theorem [33].

Let $p_1$ and $p_2$ be two different harmonic wave solutions of $e^{-i\omega t}$ time dependency in this medium, so that they each satisfy the Helmholtz equation [33]:

$$\nabla^2 p_1 + k^2 p_1 = -f_1; \tag{3.18}$$

$$\nabla^2 p_2 + k^2 p_2 = -f_2. \tag{3.19}$$

Consider as well the surface integral $I$ [33]:

$$I = \int_S [p_2(\nabla p_1 \cdot \boldsymbol{n}) - p_1(\nabla p_2 \cdot \boldsymbol{n})] dS. \tag{3.20}$$

Applying the divergence theorem to each of the terms and expanding the result yields an equation where some terms ($\nabla p_1 \cdot \nabla p_2$) cancel each other, so that $I$ is now [33]:

$$I = \int_V (p_2 \nabla^2 p_1 - p_1 \nabla^2 p_2) dV. \tag{3.21}$$

$p_1$ and $p_2$ can be rewritten using equations 3.18 and 3.19, so that $p_1 p_2 k^2$ terms cancel and $I$ becomes [33]:

$$I = \int_V (p_1 f_2 - p_2 f_1) dV. \tag{3.22}$$

By equating equations 3.20 and 3.22, the final form of the reciprocal theorem for a fluid is obtained [33]:

$$\int_V (p_1 f_2 - p_2 f_1) dV = \int_S [p_2(\nabla p_1 \cdot \boldsymbol{n}) - p_1(\nabla p_2 \cdot \boldsymbol{n})] dS. \tag{3.23}$$

which may also be expressed as:

$$\int_V (p_1 f_2 - p_2 f_1) dV = \int_S \left[ p_2 \frac{\partial p_1}{\partial n} - p_1 \frac{\partial p_2}{\partial n} \right] dS. \tag{3.24}$$

If the two harmonic solutions are considered again with respect to Figure 8, but this time $p_1$ is taken as the solution to an arbitrary body force f such as $\nabla^2 p + k^2 p = -f$ and $p_2$ is taken to be the fundamental solution G [33] (Section 3.3) so that:

$$\begin{gathered} p_1 = p; \quad p_2 = G; \\ \frac{\partial p_1}{\partial n} = \frac{\partial p}{\partial n}; \qquad \frac{\partial p_2}{\partial n} = \frac{\partial G}{\partial n}; \\ f_1 = f; \text{ and } \qquad f_2 = \delta(\boldsymbol{x} - \boldsymbol{y}) \, . \end{gathered} \tag{3.25}$$

Placing these expressions in the reciprocal theorem derived at equation 3.23 gives [33]:

$$\int_V [p(\boldsymbol{x}, \omega)\delta(\boldsymbol{x} - \boldsymbol{y}) - G(\boldsymbol{x}, \boldsymbol{y}, \omega) f(\boldsymbol{x}, \omega)] dV(\boldsymbol{x}) = \int_S \left[ G(\boldsymbol{x}_S, \boldsymbol{y}, \omega) \frac{\partial p(\boldsymbol{x}_S, \omega)}{\partial n(\boldsymbol{x}_S)} - p(\boldsymbol{x}_S, \omega) \frac{\delta G(\boldsymbol{x}_S, \boldsymbol{y}, \omega)}{\partial n(\boldsymbol{x}_S)} \right] dS(\boldsymbol{x}_S). \tag{3.26}$$

Using the sampling, or shifting, property of the delta function covered in Section 3.2, equation 3.26 becomes [33]:

$$\alpha p(\boldsymbol{y},\omega) = \int_V [G(\boldsymbol{x},\boldsymbol{y},\omega) f(\boldsymbol{x},\omega)] dV(\boldsymbol{x}) + \int_S \left[ G(\boldsymbol{x}_S,\boldsymbol{y},\omega) \frac{\partial p(\boldsymbol{x}_S,\omega)}{\partial n(\boldsymbol{x}_S)} - p(\boldsymbol{x}_S,\omega) \frac{\delta G(\boldsymbol{x}_S,\boldsymbol{y},\omega)}{\partial n(\boldsymbol{x}_S)} \right] dS(\boldsymbol{x}_S). \tag{3.27}$$

where [33]:

$$\alpha = \begin{cases} 1 & \boldsymbol{y}\ inside\ V \\ \frac{1}{2} & \boldsymbol{y}\ on\ S \\ 0 & \boldsymbol{y}\ outside\ V \end{cases} \tag{3.28}$$

### 3.4.1. Sommerfeld Radiation Conditions

Consider now the same region V, but contained within a finite surface S, and the surface of a large sphere $S_R$, of radius R, centred on **y** [33] as shown in Figure 9.

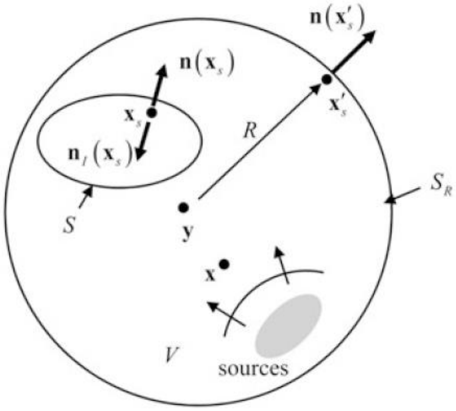

Figure 9. A large surface, $S_R$, enclosing a region containing the sources and a scattering surface S for considering radiation conditions in an infinite medium [33].

Then equation 3.27, applied to this system, becomes [33]:

$$\alpha p(\boldsymbol{y},\omega) = \int_V [G(\boldsymbol{x},\boldsymbol{y},\omega) f(\boldsymbol{x},\omega)] dV(\boldsymbol{x}) + \int_S \left[ G(\boldsymbol{x}_S,\boldsymbol{y},\omega) \frac{\partial p(\boldsymbol{x}_S,\omega)}{\partial n_1(\boldsymbol{x}_S)} - p(\boldsymbol{x}_S,\omega) \frac{\delta G(\boldsymbol{x}_S,\boldsymbol{y},\omega)}{\partial n_1(\boldsymbol{x}_S)} \right] dS(\boldsymbol{x}_S) +$$
$$\int_{S_R} \left[ G(\boldsymbol{x}'_S,\boldsymbol{y},\omega) \frac{\partial p(\boldsymbol{x}'_S,\omega)}{\partial n(\boldsymbol{x}'_S)} - p(\boldsymbol{x}'_S,\omega) \frac{\delta G(\boldsymbol{x}'_S,\boldsymbol{y},\omega)}{\partial n(\boldsymbol{x}_S)} \right] dS(\boldsymbol{x}'_S). \tag{3.29}$$

On $S_R$, because it is a contour integral, G can be defined as a Green's function to the Helmholtz equation such that [33] $G = \frac{e^{ikR}}{4\pi R}$ with $R = |x - x_0|$, as defined in Section 3.3. Equation 3.17 becomes:

$$\frac{\partial G}{\partial n(x_s')} = \frac{\partial G}{\partial R} = \frac{ike^{ikR}}{4\pi R} - \frac{e^{ikR}}{4\pi R^2} = ikG - \frac{G}{R}. \tag{3.30}$$

Therefore, the contour integral on S$_R$ can be rewritten as [33]:

$$\int_{S_R} \left[ G\left(\frac{\partial p}{\partial R} - ikp\right) + \frac{pG}{R}\right] R^2 d\Omega. \tag{3.31}$$

In terms of solid angle dΩ=sinθdθdΦ as given in spherical coordinates (R, θ, Φ) with respect to the origin **y** [33]. The integral can be expanded further as:

$$\frac{1}{4}\pi \int_{S_R} e^{ikR}\left(\frac{\partial p}{\partial R} - ikp\right) R d\Omega + \frac{1}{4}\pi \int_{S_R} e^{ikR} p d\Omega. \tag{3.32}$$

This, finally, leads to the Sommerfeld radiation conditions [33]: both integrals will disappear as R tends towards infinity if:

$$R\left(\frac{\partial p}{\partial R} - ikp\right) \to 0 \quad as\ R \to \infty;$$

$$p \to 0 \qquad\qquad as\ R \to \infty. \tag{3.33}$$

Note that these radiation conditions are valid only for harmonic waves of $e^{-i\omega t}$ time dependency [33]. These conditions ensure that waves at infinity are outgoing waves and decay sufficiently fast so that there are no sources at infinity.

### 3.4.2. Rayleigh Sommerfeld Integral

To analyze the behaviour of sound pressure when entering a fluid, it is useful to picture a half-space V ($x_3 \equiv Z\ \geq 0$ ), where the fluid is in the space shown in Figure 10. The x-y plane is the boundary and represents the face of the transducer. On this plane, the surface S represents the active surface of the transducer. The velocity is assumed to be in the z direction and 0 everywhere else except directly on S [33].

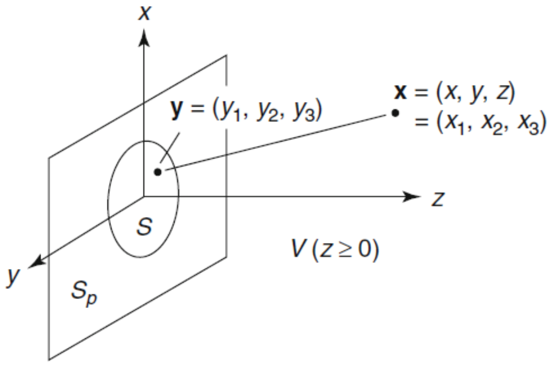

Figure 10. A fluid half space in the region z≥0 bounded by the planar surface Sp [34].

First, the integral representation theorem for the pressure in a fluid, which was derived at equation 3.26, is applied to the half-space V shown in Figure 10 with the assumption that f=0 and that the radiated pressure satisfies the Sommerfeld radiation conditions [33]. It follows that the pressure at a point **x**, in V, can be written as:

$$p(x,\omega) = \int_{S_p}\left[G(\boldsymbol{x},\boldsymbol{y},\omega)\frac{\partial p(\boldsymbol{y},\omega)}{\partial n(\boldsymbol{y})} - p(\boldsymbol{y},\omega)\frac{\partial G(\boldsymbol{x},\boldsymbol{y},\omega)}{\partial n(\boldsymbol{y})}\right]dS(\boldsymbol{y})\ . \tag{3.34}$$

But this equation is not directly useful because both the pressure p and its normal derivative on the x-y plane would have to be known. However, the Green's function used in the derivation of the radiation conditions (equation 3.17) can still apply here [33].

As defined in equations 3.17 and 3.16 respectively, $G = \frac{e^{ikr}}{4\pi r}$ is a solution for a point source that satisfies $\nabla^2 G + k^2 G = -\delta(\boldsymbol{x}-\boldsymbol{y})$. If a new Green's function, G*, due to a point source outside of V as shown in Figure 11, is considered where [33]:

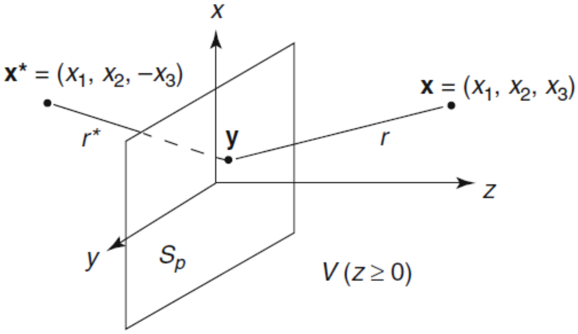

Figure 11. The source point x in V and its image point x*, which is outside V, and the corresponding distances rand r* from a point y on the x—y plane [33].

$$G^* = \frac{e^{ikr}}{4\pi r} + \frac{e^{ikr^*}}{4\pi r^*}. \tag{3.35}$$

G* has the following properties [33]:

$$\text{On } S_p\text{:} \quad G^* = 2G, \qquad \frac{\partial G}{\partial n} = 0.$$

$$\nabla^2 G^* + k^2 G^* \qquad = -\delta(\boldsymbol{x} - \boldsymbol{y}) - \delta(\boldsymbol{x}^* - \boldsymbol{y});$$

$$= -\delta(\boldsymbol{x} - \boldsymbol{y}) \; for \; \boldsymbol{x} \; in \; V. \tag{3.36}$$

By placing G* in the reciprocal theorem obtained at equation 3.24, and by following the same steps used to obtain equation 3.27, the pressure is found to be [33]:

$$p(\boldsymbol{x}, \omega) = \frac{1}{2\pi} \int_{S_p} \frac{\partial p(\boldsymbol{y}, \omega)}{\partial n(\boldsymbol{y})} \frac{e^{ikr}}{r} dS(\boldsymbol{y}) \, . \tag{3.37}$$

But:

$$\frac{\partial p}{\partial n} = \frac{v_n}{i\omega\rho} = -\frac{v_z}{i\omega\rho}. \tag{3.38}$$

Note that -z here represents the negative direction on $S_p$, v the velocity on the active surface of the transducer, and ρ is the fluid’s density. Substituting this into the previous equation leads, finally, to the Rayleigh Sommerfeld Integral [33]:

$$p(\boldsymbol{x}, \omega) = \frac{-i\omega\rho}{2\pi} \int_{S_p} v_z(\boldsymbol{y}, \omega) \frac{e^{ikr}}{r} dS(\boldsymbol{y}) \, . \tag{3.39}$$

In the special case where the velocity $v_z = v_0(\omega)$ is constant on S and zero elsewhere, the pressure is [33]:

$$p(\boldsymbol{x}, \omega) = \frac{-i\omega\rho v_0(\omega)}{2\pi} \int_{S_p} \frac{e^{ikr}}{r} dS \, . \tag{3.40}$$

This would correspond to the transducer moving uniformly as a piston, surrounded by an infinite, motionless, plane, called a planar baffle [33].

# 4. Working Principles of Conventional Ultrasonic Testing

The term “Ultrasonic technology” is somewhat ambiguous, as there are many techniques that use the same starting principle: a sound wave with a high frequency, above the audible upper limit of human hearing, travelling through solid or liquid matter. Most ultrasonic inspections are performed using frequencies between 1 MHz and 25 MHz, while the range of human hearing is approximately 20 Hz to 20 kHz [34]. The most common examples of ultrasonic technologies are sonar and real time locating systems, medical applications like sonography or therapeutic ultrasound, and, of course, the multiple non-destructive applications. Here, two versions of conventional ultrasonic testing method pertaining to the IWSLJ inspection will be looked at: Pulse echo and through transmission.

## 4.1. Wave Propagation

Ultrasonic waves differ from light or X-rays, in the sense that they are mechanical waves and not electromagnetic waves [34]. It is the oscillations or vibrations of the particles in a material, or substance, that creates the wave. Ultrasonic waves can propagate in solid, liquid, or gas. They will reflect from surfaces, refract at a boundary between two media that have different characteristic acoustic velocities, diffract at edges and around obstacles and scatter when bouncing on a rough surface [34]. When the particles inside the material are disturbed by an outside force, like an ultrasonic wave, internal stresses act to bring the particles back to their original positions. But because of the bonds present between adjacent atoms, the displacement of one particle, even to go back to equilibrium, will disturb its neighbours, and so on, propagating as a stress-strain wave [34].

There are four principal modes in which sound can propagate through matter. All four are used for different NDT applications, but the two most common are longitudinal and shear waves. There are also surface (Rayleigh) waves, and applicable only in thin materials, plate (Lamb) waves [34]. As Figure 7 shows, a longitudinal wave is defined as such because the oscillations propagate in the longitudinal direction, or the direction of wave propagation. Since compressional and dilatational forces are active, it is sometimes called a pressure wave [34]. In the case of a shear wave, the pressure is normal to the unit surface. Shear force is defined as force per unit surface, but directed parallel to that surface. Thus, the only difference between pressure and shear is one of direction [34].

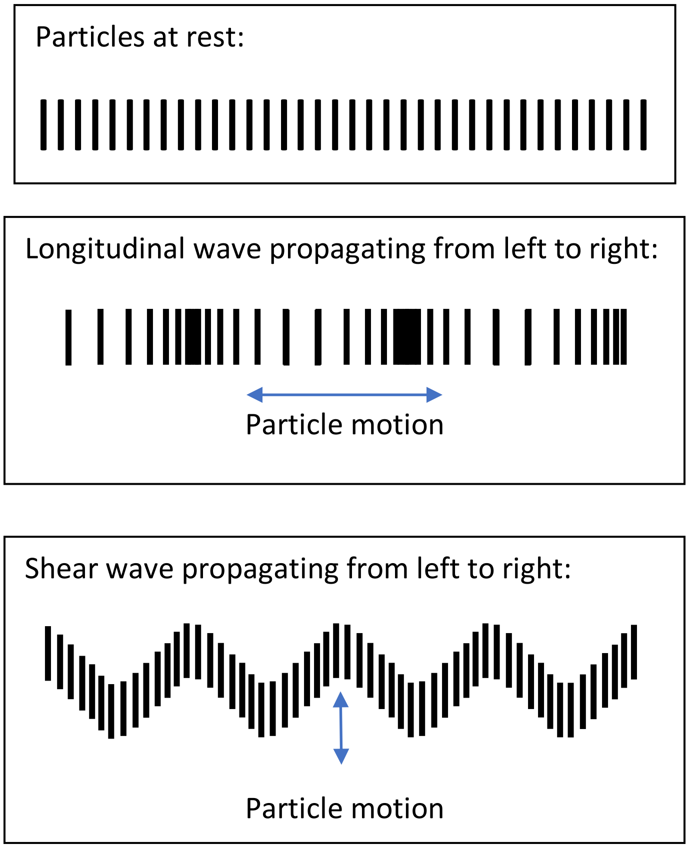

Figure 12. Particle motion caused by longitudinal and shear waves.

## 4.2. Wave Generation

The pulse of ultrasonic energy that is sent into the material is generated through the use of a piezoelectric crystal. Piezoelectric materials have the special ability to generate electricity when a mechanical force is applied to them, or to generate a mechanical energy when an electrical energy is applied to them [35]. Thus, by applying an electrical potential to the crystal and making it vibrate at a specific frequency, a wave of mechanical distortion is transmitted into the material. When a reflection comes back and hits the crystal, the mechanical disturbance is transformed into an electrical energy signal and relayed to the transducer. The transducer therefore has two functions; generating the electrical signal that is sent to the probe in the form of a mechanical distortion, and transforming the mechanical distortion it receives from the probe back into an electrical signal. The energy wave that is created by the transducer is often described in terms of pressure [36], and can be modelled mathematically, as will be discussed in Section

4.5. Most modern piezoelectric transducers use ceramic such as Barium Titanium (BaTi), Lead Zirconate Titanate (PZT) and Lead Magnesium Niobate (PMN) [35].

Most piezoelectric transducers use a single transducer that emits ultrasound and senses the resultant echoes, known as pulse-echo mode. However, it is also possible to use two different transducers in one probe (often referred to as the transmitter receiver): one with a crystal emitting a wave, the other exclusively receiving the reflected and refracted waves. This type of transmitter is often used in pitch-catch mode [37]. The initial structure of the piezoelectric transducer will depend on the kind of waves that are desired, be it shear, longitudinal or Rayleigh waves [37]. In the case of this thesis, the transducer of interest being used with the EPOCH 600© is a piston-type transducer with a single crystal designed for pulse-echo inspection with the use of longitudinal waves.

A basic pulser receiver circuit is shown in Figure 13, where the piezoelectric ceramic is represented as an electrical capacitance $C_0$. The oscillation is caused by the high-voltage electrical spike $U_s$ hitting $C_0$ [35].

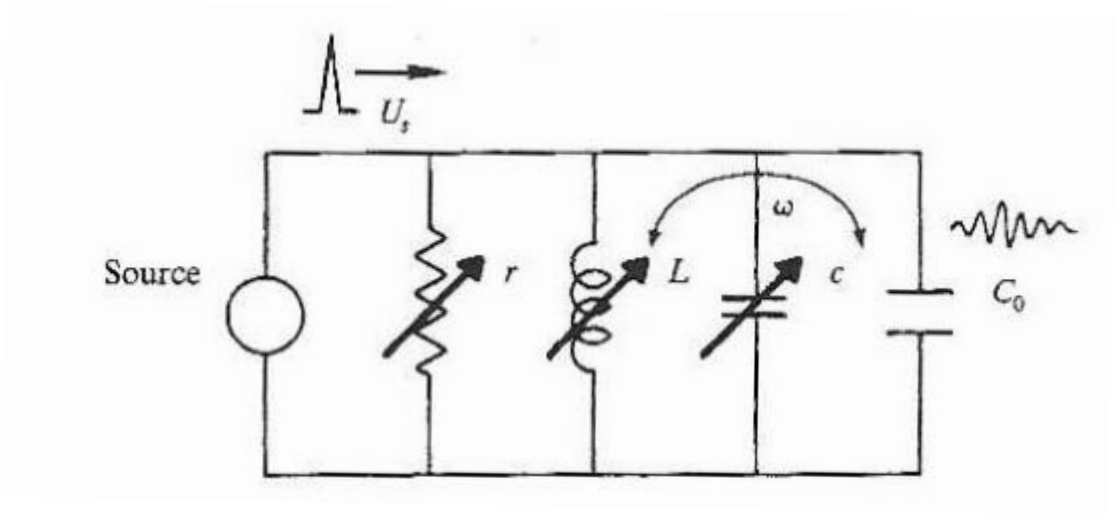

Figure 13. A basic pulser-receiver circuit [35].

The ideal resonant frequency, $f_{re}$, of the transducer is determined by [35]:

$$f_{re} = \frac{1}{2\pi\sqrt{LC_0}}, \tag{4.1}$$

where L is the inductance of the coil. It was already explained that piezoelectric materials have the ability to generate electricity when a mechanical force is applied to them, or to generate a mechanical energy when an electrical energy is applied to them. This means that the transducer also has a mechanical resonant frequency, $f_{rm}$, determined by [35]:

$$f_{rm} = \frac{1}{2\pi}\sqrt{\frac{s}{M}}, \tag{4.2}$$

where s is the mechanical stiffness of the transducer material and M represents its mass. The transducer's optimal performance happens when $f_{rm}$ is equal to $f_{re}$ [35]. ω is the resonant frequency and is defined as [38]:

$$\omega = \frac{1}{\sqrt{LC_0}}. \tag{4.3}$$

From equations 4.2 and 4.3, it can be observed that the only non-constant term is the inductance L. Therefore, the electrical damping, and consequently the pulse length, can be altered through the resistance R [35]. Knowing that the damping factor, ζ, is defined as [38]:

$$\zeta = \frac{R}{2}\sqrt{\frac{C_o}{L}}. \tag{4.4}$$

The EPOCH 600© allows the user to choose the intensity of the voltage, $U_s$, ranging from 0 to 400 V, by increments of 100 V and proposes four different resistances to affect damping: 50 Ω, 100 Ω, 200 Ω and 400 Ω [39]. Generally, the lowest resistance increases damping and near-surface resolution, while the highest resistance improves penetration power [39]. In the case of this thesis, because both high penetrating power and near surface resolution are important, the resistance is set to 200 Ω.

## 4.3. Attenuation and Reflection

By analogy, an ultrasound probe works the same way a sonar does: it sends an acoustic signal propagating through matter (water for example) and listens for a possible echo. If the wave does not return to the sonar sensor, there is no echo, and nothing to be observed. Ultrasonic testing works in a similar fashion: it sends a signal in a material and listens for the echo. Except that the wave will have to go through multiple media, will most likely reflect a few times between layers, before being sent back towards the transducer after being reflected by the back wall and will attenuate with distance travelled.

Attenuation has been found to be directly related to the distance travelled by the wave, but also to its frequency [40]. The sound pressure in a media will decay as [36]:

$$P = P_0 e^{-\alpha z}. \tag{4.5}$$

Where $P_0$ and P are the sound pressure at the beginning and at the end of a section of length z, with an attenuation coefficient α [36].

The attenuation coefficient α is sometimes referred to in terms of intensity rather than sound pressure. In that case, equation 4.5 can be written as [36]:

$$I = I_0 e^{-\alpha_I z}. \tag{4.6}$$

And because the intensity is proportional to the square of the sound pressure [36], equations 4.5 and 4.6 can be related as to obtain:

$$e_I^{-\alpha_I z} = e^{-2\alpha z} \qquad \rightarrow \qquad \alpha_I = 2\alpha$$

Taking the natural log of equation 4.5 yields:

$$\alpha z = ln \frac{P_0}{P}. \tag{4.7}$$

This corresponds to a dimensionless number representing the attenuation over the distance d, expressed in nepers (Np). The attenuation coefficient has therefore, units of Np/cm [36] (or other appropriate units of distance). However, following the common practice of electrical measurement, the decibel per metre is preferred as the attenuation coefficient unit, and is obtained by using the log to base 10 in equation 4.7 (instead of the natural log) and then multiplied by 20 as:

$$\alpha z = 20 log \frac{P_0}{P} dB. \tag{4.8}$$

Working with the decibel unit allows for various ratios of pressure to be described with simple numbers. Table 2 shows how the ratio of $\frac{P_0}{P}$ can be expressed in dB [41]:

Table 2. Pressure ratios and dB values.

| $\frac{P_0}{P}$ | Equation | dB |
|---|---|---|
| 1/4 | dB=20log (0.25) | -12 |
| 1/2 | dB=20log (0.5) | -6 |
| 1 | dB=20log (1) | 0 |
| 2 | dB=20log (2) | 6 |
| 10 | dB=20log (10) | 20 |
| 100 | dB=20log (100) | 40 |
| 10,000 | dB=20log (10,000) | 80 |

From Table 2, it can be understood why the value of ± 6 dB is often referred to in ultrasonic testing. Adjusting the gain by 6 dB allows to double or cut in half the signal amplitude. In the case of this paper, gains ranging from 40 to 70 dB were used, depending on the probe frequency. It means that the sound pressure coming back to the transducer is at least 100 times weaker than the initial pressure, $P_{0.}$

The attenuation of titanium and water are shown in Figure 14 in terms of normalized pressure, so that the values can be better compared, as the sound pressure is dependent on the speed of sound in the material of interest and a few other factors that are material dependent (see Appendix A1). Therefore the Y axis shows only the exponential of equation 4.5 with the attenuation coefficient α and the distance z. The attenuation coefficient of titanium was calculated based on pressure values obtained with the modelling equations introduced in Section 3.4, and the water coefficient was found in the literature [42].

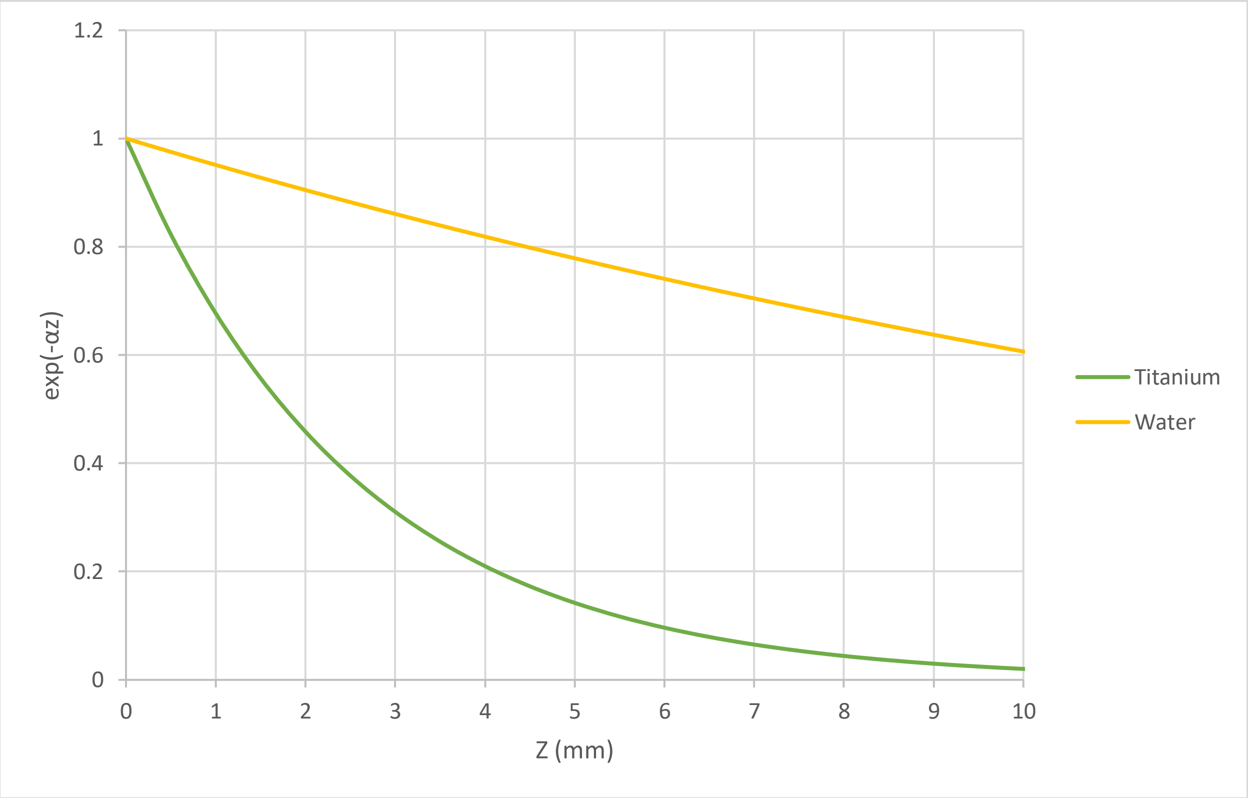

Figure 14. Acoustic attenuation of titanium and water at a frequency of 5 MHz.

The main factors that can explain why a sound wave attenuates are beam spreading, sound absorption and sound scattering. Beam spreading is discussed further in Section 4.4. Absorption is the conversion of sound energy into other forms of energy, mainly heat, for which several processes can be responsible [36]. Absorption has the effect of slowing down the oscillations of the particles, which is why high frequencies, associated with more rapid oscillations, will lose more energy. The absorption rate is proportional to the frequency, just like scattering, but disperses at a slower rate. Absorption weakens the transmitted energy and the echoes from both reflectors and the back wall [36]. To compensate, the transmitter voltage and the amplification can be increased, or the fact that there is less absorption at lower frequency can be exploited. What remains more of a problem, is scattering. Not only does it reduce the height of the echo from both the reflector and the back wall, but it can also produce multiple echoes with different transit times, sometimes referred to as grass, in which the true echoes may get lost [36]. One solution could be to use lower frequencies, but this would also limit the detection of small flaws due to the increase in wavelength and therefore, loss of resolution.

Scattering can be described as the reflection of sound in directions other than its original direction of propagation. Many factors can cause scatter, such as surface roughness or grain sizes in anisotropic materials [36]. As frequency increases, sound tends to scatter from large coarse grain structure, such as cast irons, and from small imperfections within a material [43], which are common in composite materials. High frequencies tend to experience more sound scattering because of their shorter wavelength. In the case of CFRP, the main sources of noise scattering, and therefore attenuation, are porosity and rich-resin areas [2].

The reason why the attenuation of CFRP is not shown in Figure 14 is that the attenuation coefficient α represents the total attenuation coefficient, normally made of three constituents [44]: geometrical spreading of the transducer field $\alpha_G$, absorption $\alpha_A$, and scattering at the grain boundaries $\alpha_S$ so that $\alpha = \alpha_G + \alpha_A + \alpha_S$ [44]. The overall attenuation coefficient for most common materials, like metals and water, is a good approximation of the exact attenuation coefficient, as the contribution of $\alpha_G, \alpha_A$ or $\alpha_S$ are often negligible. Some metals with large grain size, like cast irons and copper, are an exception to this rule. In the case of composite materials, the combined effects of material anisotropy and viscoelasticity make it imperative, when studying composites, to look at the different components of the alpha coefficient, which for composites becomes the sum of matrix viscosity, scattering attenuation due to defects, and energy loss at the fibre/matrix interface [45].

It was explained in 2.4.2 how the fibre component of a composite is always much stiffer than its matrix. The fibres and the matrix will also carry the ultrasonic wave at different speeds, inducing strong stress and interlaminar shear stresses on free edges [45]. R. Li et al. [45] studied the attenuating nature of composites and found that the overall attenuation coefficient α can be expressed as a function of frequency and Young's modulus ratio of fibre and matrix region:

$$\alpha^{sum}(\mu, f) = (1 - \emptyset)\alpha^{vis}(\mu, f) + \alpha^{int}(\mu, f) + \alpha^{def}(\mu, f). \tag{4.9}$$

Where $\emptyset$ is the defect volume fraction, $\alpha^{vis}$ is the viscoelastic attenuation coefficient, $\alpha^{int}$, represents the energy loss at the fibre/matrix interface and $\alpha^{def}$ is the coefficient for wave scattering and scattering due to the wave encountering defects [45]. R. Li et al. [45] modelled the impact of each of these components on a two-layered fibre/matrix composite. The matrix used in this paper has very similar material properties to the epoxy used on the IWSLJ, but the fibres differ in density and sound velocity. Their results are presented in Figure 15.

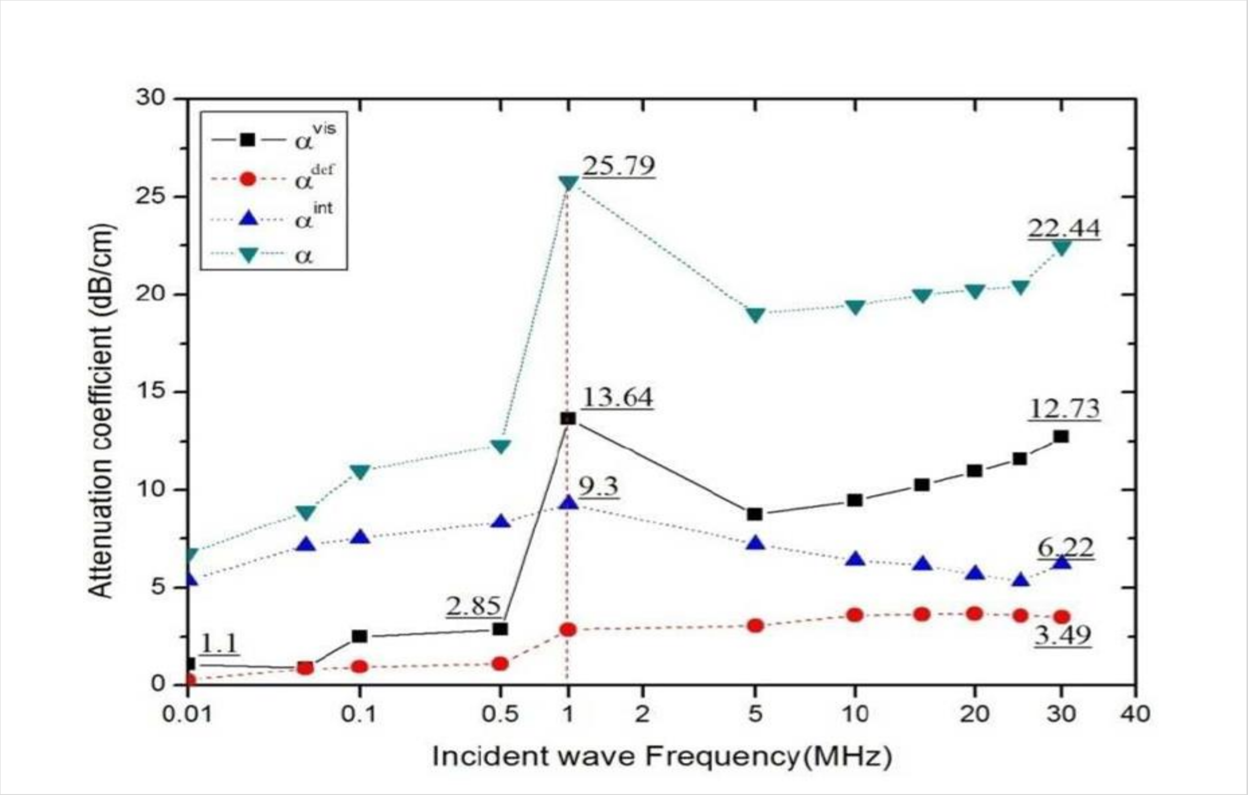

Figure 15. Attenuation coefficients for composite material, at different frequencies [45].

From Figure 15, the attenuation coefficients at 2.25, 5 and 10 MHz, respectively, are about 20, 19 and 19.5 dB/cm. Figure 16 shows the attenuation of titanium and water, but in relation to the attenuation of CFRP with an attenuation coefficient obtained in Figure 15. Figure 15 uses the same axis as Figure 14.

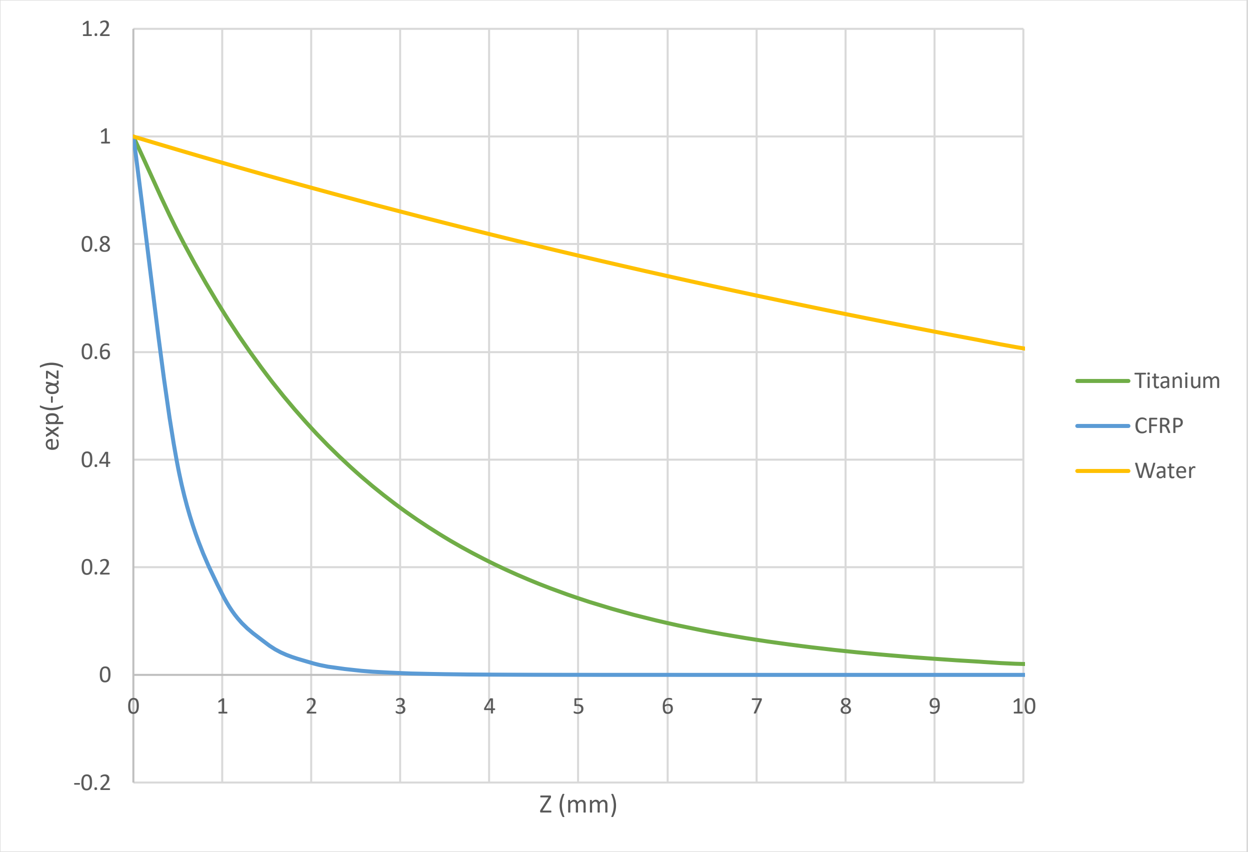

Figure 16. Acoustic attenuation of different materials, f=5 MHz.

Refraction occurs at the boundary between two media and is caused by the difference in acoustic velocities and densities of those two media. If the sound is travelling faster in the second layer, the wave will bend and slightly change direction [43]. This physical phenomenon is similar to refraction out of water. When looking at an object in water, it always seems that the submerged part is not aligned with the part that is still out of the water. This occurs because light travels at a different speed under water and its course is slightly offset when it exits water into air. If the initial wave is coming at an incident angle $\theta_1$ and at a speed $\upsilon_1$ , Snell's law is required to predict the transmitted angle $\theta_2$ as well as the speed of the wave in the new medium, $\upsilon_2$ [43]:

$$\frac{sin\theta_1}{sin\theta_2} = \frac{\upsilon_2}{\upsilon_1}. \tag{4.10}$$

In the case where the transmitted angle, $\theta_2$, is equal to 90°, the incident angle $\theta_1$ is known as the critical angle. Any angle larger than the critical angle will result in total reflection of the beam in the first medium.

This becomes especially important when conducting inspections with angled beam. In the case of the IWSLJ, only a straight-beam inspection is performed, but if the initial wave were to penetrate the CFRP at an angle, not only would it be converted into a shear wave, as will be discussed in Section 4.7, but it would also affect the way the wave is hitting the titanium, as shown in Figure 17. Sound travels faster in titanium than CFRP (see Section 4.7.2), so an angled beam inspection in the case of the IWSLJ would yield complicated signals to decipher, thus making the straight beam inspection an obvious choice.

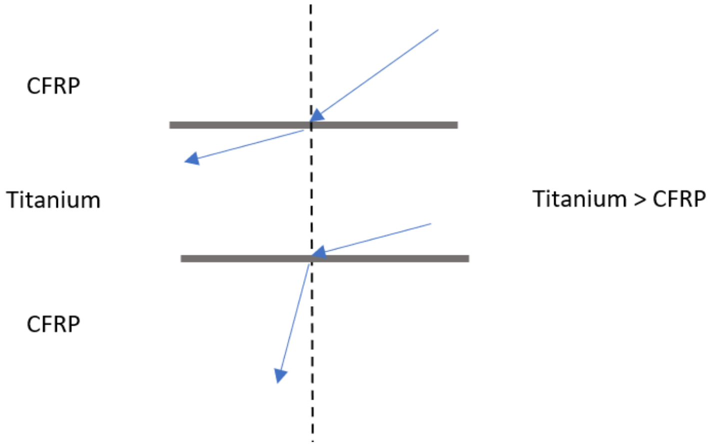

Figure 17. Example of Snell's law [40].

It should be noted that the titanium and CFRP surfaces are not perfectly parallel. A slope of approximately 1 degree can be measured on the titanium splice plate, but the effects for that angle on sound transmission are considered minimal, as the transmitted beam is at a 2.3-degree angle. Therefore, for this thesis, the surfaces are considered to be parallel.

It is of critical importance to note that when a wave arrives at an interface between two media, it will obviously not be entirely transmitted. Some, if not most of it, will be reflected back. The concept of impedance is probably the most important concept in ultrasonic testing, because it explains how much sound goes through the second layer, and how much is reflected back. The impedance, Z ($kg/m^2s$), is defined as $Z = \rho c$, where ρ, expressed in $kg/m^3$, is the density of the material, and c, in m/s, is the speed of sound in that same material. In order to know how much sound is reflected and how much is transmitted, in the case of normal incidence, the following equation applies [43]:

$$\% \, Reflection = \left[\frac{Z_2 - Z_1}{Z_2 + Z_1}\right]^2 . \tag{4.11}$$

Assuming there is no energy loss at the boundary, then the percentage of the wave being transmitted is 1 minus equation 4.11 It is interesting to look at a few numerical examples, especially involving air. Table 3 presents a few materials and their respective acoustic impedances.

Table 3. Impedance of different materials

| Material | ρ (kg/m$^3$) | C (m/s) | Z (kg/m$^2$s) |
|---|---|---|---|
| Aluminum [43] | 2712 | 6320 | 17.1 x10$^6$ |
| Steel [43] | 7850 | 5940 | 46.6 x10$^6$ |
| Copper [43] | 8940 | 4600 | 41.1 x10$^6$ |
| Titanium [43] | 4500 | 6070 | 28 x10$^6$ |
| Water [43] | 1000 | 1500 | 1.5 x10$^6$ |
| Air [43] | 1.225 | 344 | 421.4 |
| Glycerine [46] | 1261 | 1904 | 2.4 x10$^6$ |
| Polystyrene [49] [47] | 1004 | 2350 | 2.36×10$^6$ |
| CFRP [48] | 1600 | 2622 | 4.19 x10$^6$ |

In the case of the inspection of the IWSLJ, the sound wave goes first through polypropylene (which is the delay line, see section 6) and into the couplant, before travelling through all the different layers of the IWSLJ. Table 4 was populated using equation 4.11, and includes in the fourth column the percentage of the original signal being transmitted at each interface. The high impedance mismatch between air and CFRP is responsible for the back wall echo, since 99.96% of the sound is reflected back inside the IWSLJ. The same phenomenon explains how disbonds or cracks are detected: the wave encounters air and is reflected sooner than expected towards the transmitter.

Table 4. Sound transmission in the IWSLJ

| Interface | % Reflected | % Transmitted | % Of the original impulse being transmitted back to the transducer |
|---|---|---|---|
| Polystyrene → Glycerine | 0.01 | 99.99 | 99.99 |
| Glycerine → CFRP | 7.17 | 92.83 | 92.82 |
| CFRP → Titanium | 54.71 | 45.29 | 42.04 |
| Titanium → CFRP | 54.71 | 45.29 | 19.03 |
| CFRP → Air (back wall echo) | 99.96 | 0.04 | 0.76 |
| CFRP → Titanium | 54.71 | 45.29 | 8.62 |
| Titanium → CFRP | 54.71 | 45.29 | 3.90 |
| CFRP → Glycerine | 7.17 | 92.83 | 3.62 |
| Glycerine → Polystyrene | 0.01 | 99.99 | 3.62 |

Table 4 also shows that the transmitter receives only 3.62% of the original impulse. Figure 18 shows graphically what Table 4 shows in numbers. The signal coming back from the back wall or the IML has to travel across a large number of interfaces, and is therefore, further reduced. This is why high gain values, reaching 70 dB, were used during testing. At 70 dB, the received signal is amplified by a factor of 100.

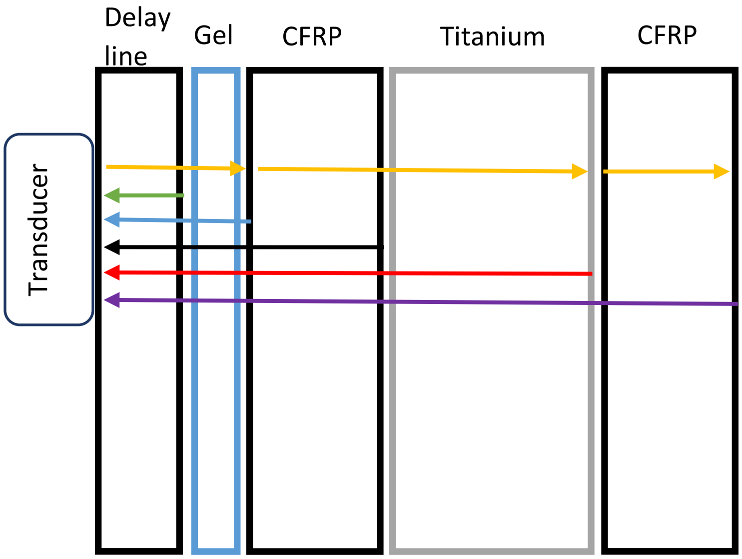

Figure 18. Representation of sound transmission in the IWSLJ based on impedance mismatch.

## 4.4. Sound Field

We often talk about “a” wave propagating through a media, but in reality, when ultrasound emanates from an ultrasonic probe it does not come from a single point but rather originates from many points along the surface of the piezoelectric element. This results in a sound beam containing many waves interacting and interfering with each other. When waves interact, they superimpose on each other and the amplitudes of the sound pressure will sum up at any point, leading to both constructive and destructive interference. This means that if the waves are in phase, the total combined pressure will be doubled, whereas if they’re completely out of phase they will cancel each other.  As sound waves emanate from the transducer, the pressure fluctuations in the near field immediately adjacent to the probe are erratic because of the fast-changing phase relationships within close proximity of the pressure wave [35]. Beyond this region, there is the far field where the pressure wave will decay smoothly as a function of distance travelled [35].

One of the best ways to picture the effects of interfering waveforms is to look at perturbations in water, as shown in Figure 19. The waves will radiate out from their initial sources with a circular wave front and will interact with each other as described above. It can be observed that closer to the origin, or the transducer, the more interaction there is between the waves, the more uneven the sound field is. This is referred to as the near-field. The sound is more uniform away from the transducer, or in the far field [49].

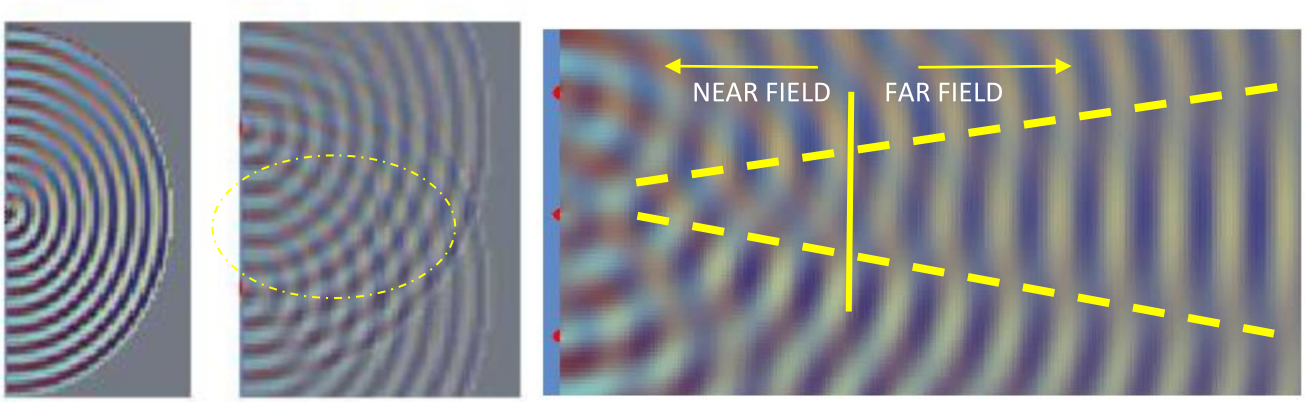

Figure 19. Wave interaction in water, showing the near and far field effect [50].

Huygens's principle is one of the best ways to describe why ultrasonic waves radiate the way they do [36]. The principle states that any arbitrary wave form can be constructed from a large number of simple spherical waves of the same frequency, called elementary waves [36]. In other words, every point on a wave front is a source of secondary waves, sometimes referred to as wavelets in older textbooks. These elementary waves spread out in the forward direction, at the same speed as the source wave, creating the new wave front. Figure 20 [36] shows how these elementary waves can interact together to create a wave front. In the case of a wire, or a rectangular piston, the waves would propagate in a cylindrical fashion. But in the case of a circular oscillator, the waves would propagate in a spherical fashion [36].

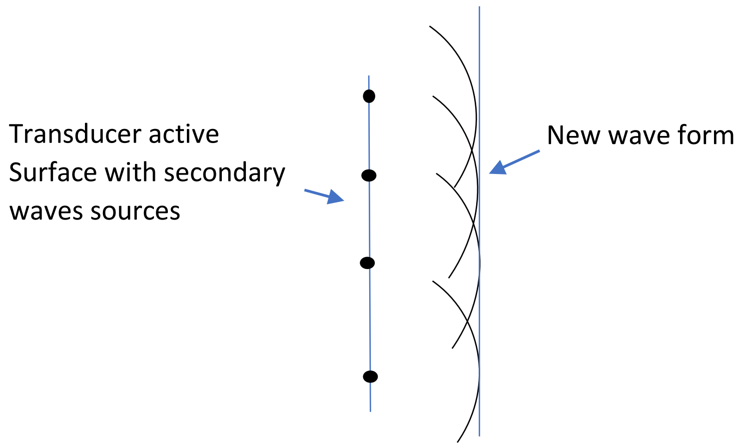

Figure 20. Construction of wave surfaces from elementary waves according to Huygens.

Huygens's principle can explain how the wave front behaves, but does not give any specific information, such as how strong the excitation of particles becomes at any given point in the sound field. For that, the mathematical model developed by Fresnel, called zone construction, is required [36].

First, it can be observed from Figure 20 that the elementary waves will not travel along the same paths, having different points of origin on the radiating surface. Therefore, differences in sound pressure at different points of the sound field will be observed. It is also known that pressure decreases with distance travelled, because the sound beam spreads out and is attenuated. Consequently, the sound pressure value of the elementary waves cannot simply be added: their path differences must be considered [36]. The principles of wave interference apply and two waves of the same amplitude with a path difference of one-half wavelength would cancel each other, whereas two waves of the same amplitude and same path length would double in amplitude [43]. This can be represented by vector addition with angular measurement, as opposed to linear measurements, where one full wavelength corresponds to an angle φ, or 2 π. The path difference between the elementary waves, l, is linked to the phase angle by the following relationship [36]:

$$\varphi = 2\pi \frac{l}{\lambda}. \tag{4.12}$$

When applying the Fresnel's zone construction method, the first step is to sort into groups of the same path length the elementary waves radiated from the surface. This is done by adding their individual vectors, thus producing, at a given point of the sound field, the resultant sound pressure [36]. For a flat radiating surface oscillating uniformly, like the transducers used by the EPOCH©, all the elementary waves can be added up to give a single sound pressure, which is proportional to the area of the zone. Zones, in the case of a flat oscillator, are concentric, circular rings [36].

If the surface of the radiator is divided into n annular zones, the j$^{th}$ zone having the area $S_j$ and the path of the wave from the measuring point being $a_j$, the sound pressure of this specific zone can be calculated as [36]:

$$P_j = C_j \frac{S_j}{a_j} \qquad (j = 1, \dots, n). \tag{4.13}$$

$C_j$ is a factor of proportionality that is constant across all zones. The path length $a_j$ can be obtained from the radius of the j$^{th}$ zone as [36]:

$$a_j = \sqrt{R_{j-1}^2 + a^2} \qquad (j = 2, \dots, n) \quad . \tag{4.14}$$

Where $a_1$=a. The angle of the phase $\varphi_j$ between the path $a_j$ and the axis is obtained from equation 4.12 [36]:

$$\varphi_j = \frac{2\pi}{\lambda} a_j \qquad (j = 2, \dots n). \tag{4.15}$$

With $\varphi_1$=0. Figure 21 shows how those equations can be applied to construct zones using Fresnel's method. The graphical construction of the sound pressure at two points on the axis of circular disc is shown, with the two observation points $a_1$ and $a_2$ corresponding to the near-field length and its half value, respectively [36]. The surface of the radiator has been divided into 12 zones with vectors 1 to 12. Their respective lengths can be calculated with the equations introduced above. The most important takeaway is that the lengths of the wave paths vary ever so slightly at a far enough distance from the radiator, whereas it is continually changing in the near field [36]. The differences between the angles φ also diminish drastically. It can be observed that for the distance $a_1$, corresponding to the exact length of the near field, the chain of vectors adds up to create an exact semicircle, resulting in the sound pressure at its maximum. At the distance $a_2$, or half way in the near field, the vector chain adds up to a full circle, meaning that the resultant sound pressure totals zero. As the distances get shorter, there are more and more extreme shifts in sound pressure between maximums and minimums, whereas the chain becomes a straight line for large distances [36]. From that, it can be deduced that at large distances from a plane radiator, the sound pressure (on its axis) is proportional to its area and inversely proportional to its distance [36]. It should be noted that pressure levels have been found by other researchers to be material dependent and have been observed to vary from the detectability threshold to 2 $\rho_0 C U_0$, where $\rho_0$ is the material density, C is the wave speed and $U_0$ is the particle oscillation speed [35].

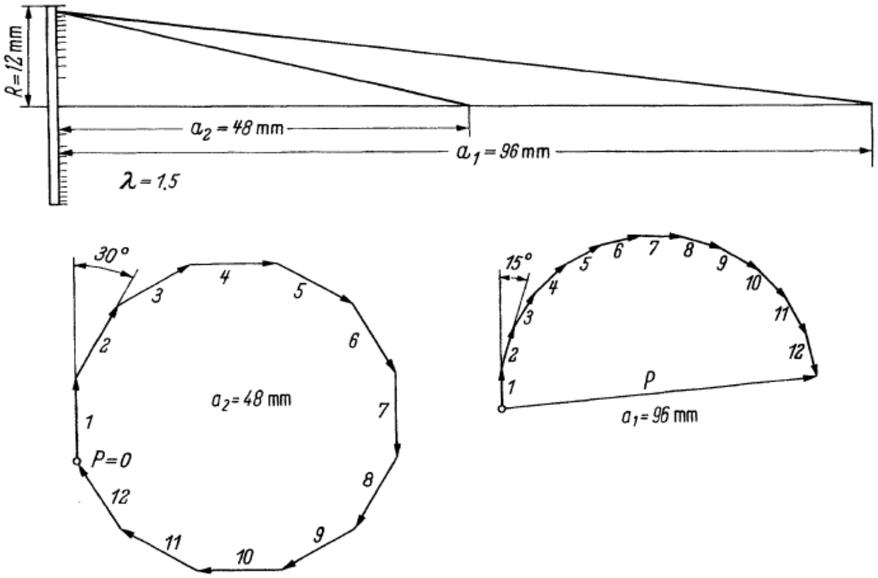

Figure 21. Example of zone Construction according to Fresnel, for two points along the axis with R=12mm and λ=1.5 mm [36].

Fresnel's zone construction method, combined with Huygens's principle, explains well what is happening in the near field, and has made clear that in the far field, the maximum sound pressure will always be along the axis of the transducer. However, when entering the far field, or the Fraunhofer zone, the sound pressure will not remain in the concentric circles defined in the Fresnel's zone. Beam spread, sometimes referred to as divergence, starts to occur and must be accounted for.

But before getting into beam spreading, it is useful to look at what the pressure pattern discussed by Fresnel looks like in three dimensions. Figure 22 shows the main lobe for a circular piston radiator. The acoustic pressure P is defined in terms of r, the distance from the centre of the element, φ /2, the angle from the centre axis of the element φ, and time t, since the pressure has the form of a travelling wave [35]. If this beam were collapsed on the (x, y) plane, all that could be seen would be the concentric circular discs described by Fresnel.

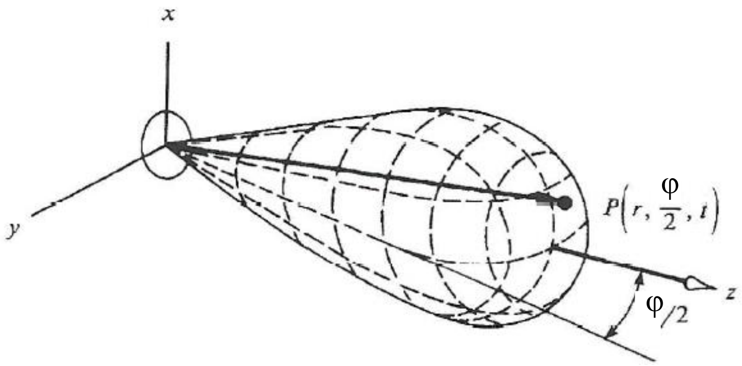

Figure 22. Main lobe of a beam generated by a circular piston [35].

The exact depth at which the near field stops and the far field begins, N, can be calculated [35] using the following equation, but is often approximated as being 1/2 λ:

$$N = \frac{d^2 - \lambda^2}{4\lambda}. \tag{4.16}$$

The pressure amplitude $P_z(r)$ is given by:

$$\frac{P_z(r)}{R} = \frac{d/\lambda}{r/d}. \tag{4.17}$$

Where d is the diameter of the probe, λ is the wavelength, r corresponds to location on z axis in polar coordinates, $P_z(r)$ is the pressure amplitude along the z-axis, R= $(\pi\rho_0 C U_0)/4$, and $C_1$ is the speed of the wave in the material.

From equation 4.17, it can be observed that larger probe diameters and higher frequencies (shorter wavelengths) result in higher pressures. However, what is not shown in the above equation is that sound pressure is also dependent on the angle away from the beam axis. As φ/2 grows larger, the phase boundary moves towards the probe until a node is reached [35]. The equation governing beam divergence is [35]:

$$\varphi = 2\,sin^{-1}\left[1.2 \times 10^{-3}\,\frac{c_1}{fd}\right], \tag{4.18}$$

where $C_1$ is the speed of the wave in the material and f is the probe frequency. Visually, divergence is what gives ultrasonic beams their distinct conical shape, as shown in Figure 23. Physically, beam divergence can be explained by the vibrating motion of the particles generating the wave. Vibrating particles do not always transfer all of their energy in the direction of wave propagation, and if the particles are not directly aligned, then some energy gets transferred at an angle [51]. In the near field, constructive and destructive wave interference make the sound field fluctuate rapidly. At the beginning of the far field, the strength of the beam is at its maximum on the centre line, and diminishes as it spreads outwards. From equation 4.18 it can be seen that beam spread will be greatly affected by the transducer's frequency and diameter. A high frequency and large diameter mean a smaller spread, and therefore, stronger reflections as the signal is more concentrated [51]. More spread is also likely to mean that the interpretation of the signal will be difficult due to the possibility of more reflections coming from the lateral surfaces [51].

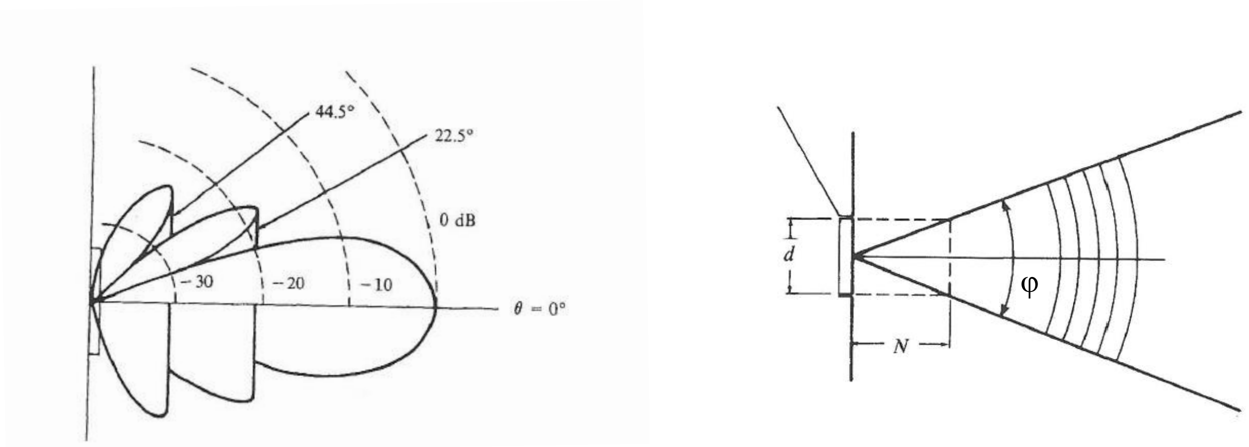

Figure 23. Beam pattern and Beam Divergence for a circular probe [35].

Probe frequency is therefore one of the most important factors affecting the minimum detectable flaw size in ultrasonic testing [35]. The wavelength has units of length, and is inversely proportional to the frequency. Probes of low frequency, 0.5 MHz to 2.25 MHz, provide greater energy and penetration in a material, while high frequency crystals, ranging from 15.0 MHz up to 25.0 MHz, provide reduced penetration but greater sensitivity to small discontinuities [52]. In the case of the IWSLJ, the biggest concern is not the size of the discontinuities, but rather the highly attenuating nature of the CFRP. It was in fact suggested in reference [19] to switch transducer frequency while inspecting the lap joint to accommodate the varying thickness of CFRP. Ten megahertz transducers were used to inspect the thin composite steps near the titanium root and 5 MHz transducers to reach the joint through the thicker carbon fibre layer near the tip of the joint. This proved successful for the OML, but showed limited capability to detect disbonds on the IML of the lap joint [19]. Reference [5] uses two different frequency probes as well: a 10 MHz transducer when searching for disbonds over Steps 1 and 2, and a 2.25 MHz transducer when looking for delaminations over steps 8 and 9. The ARMANDA system, which inspects the lap joint in its entirety, uses only a 5 MHz probe.

## 4.5. Planar Piston Transducer

The Rayleigh Sommerfeld Integral derived in Section 3.4 can be used directly to model the pressure wave field generated by a planar, circular transducer, assumed to behave like a piston. The modelling equations presented in this Section can predict sound pressure in both the near and far field, but due to approximations for the far field equation, the results are much more precise in the near field.

The Rayleigh Sommerfeld integral is derived by assuming the waves are radiating in a fluid, but it has been proven that in the paraxial approximation, used to obtain equation 3.40, compressional waves in solid behave the same as for those in an equivalent fluid medium [33].

First, in order to obtain the “on-axis” pressure, which corresponds to the sound pressure at the exact centre of the transducer, it is useful to look at Figure 24 [33]:

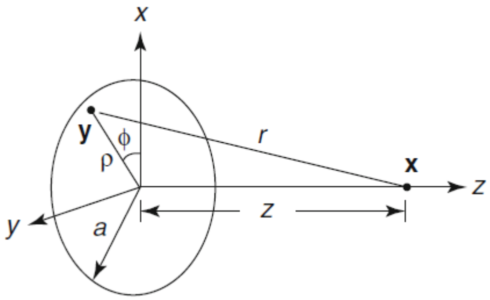

Figure 24. Geometry for calculating the on-axis response of a circular piston transducer [33].

The circle on the x-y plane represents the probe face, or the active surface of the transducer, with the axis z at its centre. The value a represents the probe diameter, and **x** can be interpreted as the depth at which the pressure is calculated inside the material. From basic geometry, $r = \sqrt{\rho^2 + z^2}$ and the area differential $dS = 2\pi r dr$. It follows that equation 3.40 becomes [33]:

$$p(z,\omega) = -i\omega\rho v_0(\omega)\int_{r=z}^{r=\sqrt{z^2+a^2}} e^{ikr}\,dr\ ;$$

$$p(z,\omega) = \rho c v_0(\omega)\left[e^{ikz} - e^{ik\sqrt{z^2+a^2}}\right], \tag{4.19}$$

where c in this case represents the phase velocity, which is ω/k.

From here, by applying the Euler Formula,$(e^{i\theta} = cos\theta - isin\theta)$, and some trigonometric identities, the pressure can be rewritten as [33]:

$$p(z,\omega) = -2i\rho c v_0(\omega)\, sin\left(\frac{k\left(\sqrt{z^2+a^2}-z\right)}{2}\right)\left[e^{\frac{ik\left(\sqrt{z^2+a^2}+z\right)}{2}}\right]. \tag{4.20}$$

Due to the nature of the sine function, there will be locations of zero pressure along the axis when its argument is zero, such as [33]:

$$\frac{k\left(\sqrt{z^2+a^2}-z\right)}{2} = n\pi \qquad n = 1,2,3,\dots \tag{4.21}$$

Isolating z, in order to determine the different null positions on the axis, $z_n$, gives [33]:

$$z_n = \frac{(ka)^2-2n\pi}{4n\pi k} = n\pi \qquad n = 1,2,3,\dots \tag{4.22}$$

$z_n$ must be positive, as it travels into the medium, so no nulls are possible for $ka > 2\pi$. It also follows that the first null appears at n=1, for $2\pi < ka < 3\pi$. The value of ka is typically large, so many nulls appear in the pressure wave field. For example, with a transducer of 6.35 mm diameter ($a$=3.175) radiating in CFRP at a frequency of 10 MHz ($k \approx 24$), ka=76.2mm. When ka is large, the value of $(2n\pi)^2$ is significantly smaller than $(ka)^2$ and can be ignored, so that [33]:

$$z_n = \frac{(ka)^2}{4\pi nk} = \frac{a^2}{2n\lambda} \qquad n = 1,2,3,\dots \tag{4.23}$$

It is important to note that $a^2/\lambda$ is one form of the near-field distance equation. More precise forms exist, such as the one introduced in Section 0. In this case, however, it is useful to rewrite equation 4.23 as [33]:

$$z_n = \frac{N}{2n} \qquad n = 1,2,3,\dots, \tag{4.24}$$

where N is the near-field distance. It shows that the null farthest away from the transducer (n=1) happens at about half a near-field distance, as shown in Figure 25. After that, even if the point of maximum pressure and the far field are not reached yet, the pressure fluctuations start to even out.

Similarly, for the points of maximum pressure, it can be shown by taking the magnitude of equation 4.20, squaring it, then setting the derivative with regards to z equal to 0 so that the cosine argument must zero such as [33]:

$$\frac{k\left(\sqrt{z^2+a^2}-z\right)}{2} = \frac{(2n+1)\pi}{2} \qquad n = 0,1,2,\ldots$$

$$z = z_m = \frac{(ka)^2-[(2n+1)\pi]^2}{2(2n+1)\pi k} \qquad n = 0,1,2,\ldots \tag{4.25}$$

which can be expressed in terms of near-field distance as $z_m = \frac{N}{2n+1}$, showing that the last on axis maximum occurs at one near-field distance [33].

After the point of maximum pressure, the pressure wave enters the far-field region and starts to behave in a smooth way. To look at the behaviour of sound pressure in that region, first the following approximations are required [33]:

$$\left(\sqrt{z^2+a^2}-z\right) \approx \left(\sqrt{z^2\left(1+\frac{a^2}{z^2}\right)}-z\right). \tag{4.26}$$

If follows that $z \approx \frac{a^2}{2z}$. Equation 4.20 then becomes [33]:

$$p(z,\omega) = -2i\rho c v_0(\omega)\, sin\left(\frac{ka^2}{4z}\right) e^{ikz}. \tag{4.27}$$

Equations 4.20, 4.22, 4.25 and 4.27 were used to model sound pressure fluctuations in CFRP and titanium, using various frequencies and a probe diameter of 6.35 mm. Figure 25 shows equations 4.20 and 4.27 in CFRP, with a 5 MHZ transducer. The detailed calculations can be found in Appendix A2.

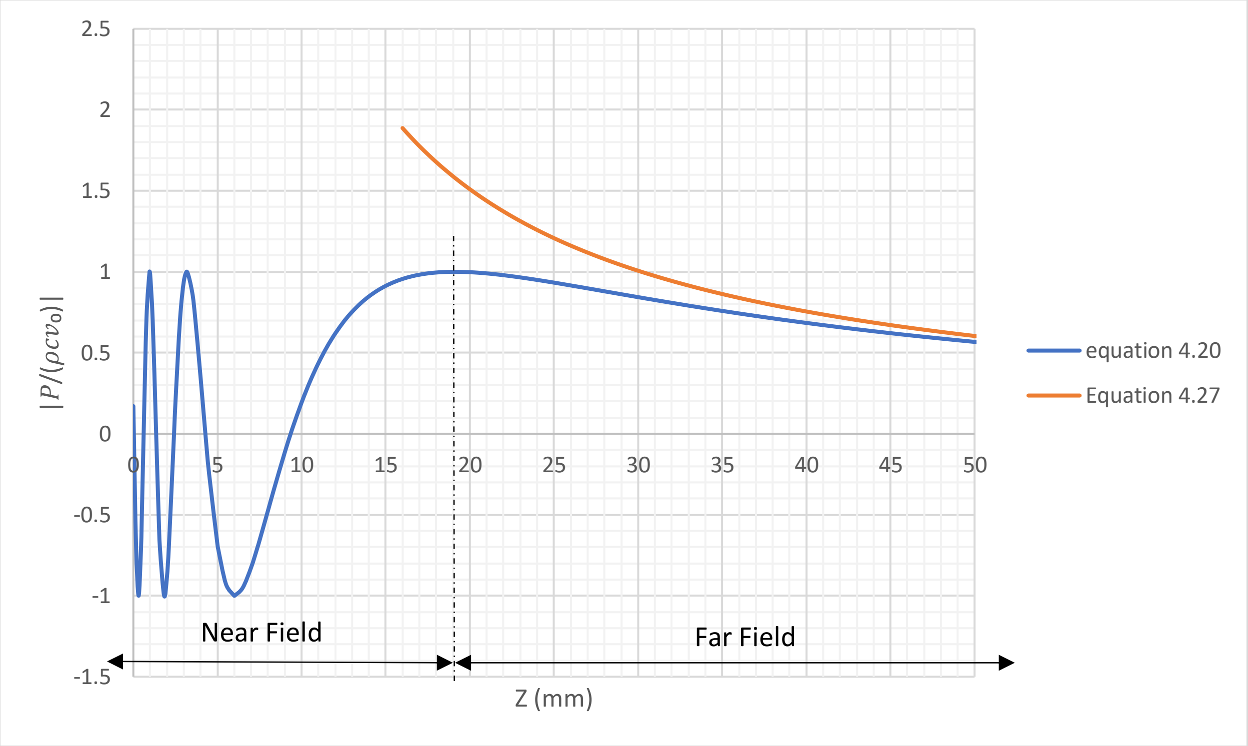

Figure 25. Magnitude of the normalized on-axis Pressure for a Plane Piston Transducer in CFRP, f=5 MHz.

## 4.6. Pulse Echo and Through Transmission

In the case of normal beam pulse echo, a transducer sends out a pulse of energy, usually in the form of a damped oscillation [36] and also senses reflected sound at the boundary of the specimen, the echo. If a crack or a flaw is present in between the probe and the back wall, a signal will come back sooner than expected, indicating its presence. Figure 26 illustrates the pulse echo method and how different flaws and the back wall echo would show up on a Cathode Ray (CR) screen. Only from looking at the screen, it is possible to determine the transit time, t, (also referred to as Time Of Flight (TOF)) to the reflector or the back wall, as well as the distance of the reflector or the back wall from the surface d. Assuming the speed of sound in the material c is known and the apparatus has been well calibrated [36], it can then be said that:

$$d = \frac{ct}{2}. \tag{4.28}$$

This kind of information is useful to perform thickness measurements, or fatigue life analysis, for example. However, this only works if the reflector or back wall is properly oriented. Although pulse echo is the most widely used UT technique, this is probably its biggest disadvantage.

To better understand the impact of angles when working with a normal beam, it is useful to look at Figure 26. In the case of elements a and b, flaws cause a reflection of the sound (and will be detected easily), but do not prevent the sound beam from hitting the back wall and producing an echo. A disbond at a titanium / CFRP interface or a delamination within the CFRP would present themselves in a similar fashion. Element c, however, has a bigger flaw that presents itself first, hiding the second one, as no sound is getting to it. This could be a delamination hiding a disbond, or a disbond hiding a crack in the titanium. In the case of element d, all the sound is deflected due to the angle of the flaw, thus preventing the back wall echo from showing. However, looking at the screen and not seeing a signal could be an indication of defect in itself, unless the part has a geometry similar to element e. In that case the beam is not incident at right angles to the back wall, also preventing the back wall echo from showing on the screen. Lastly, Element f shows high attenuation, the signal is not reaching the flaw or the back wall [36]. This could happen in a composite panel that is too thick.

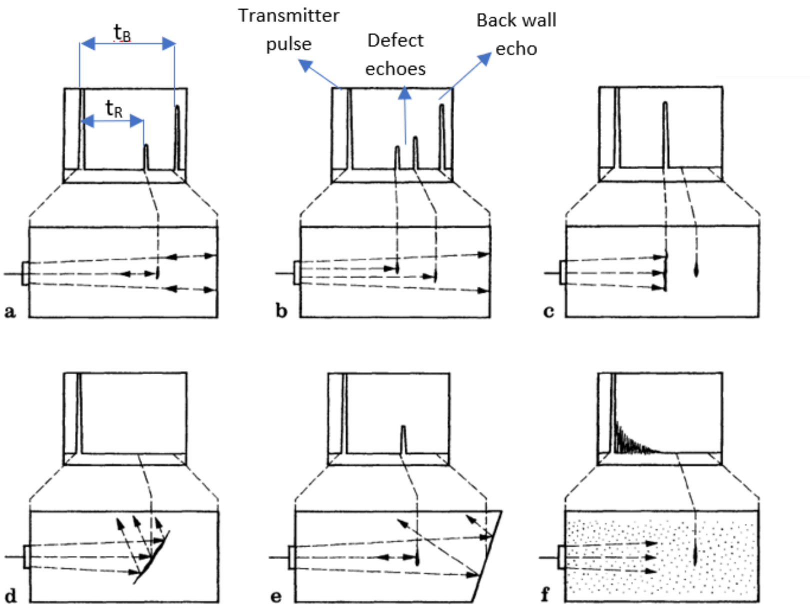

Figure 26. Schematic screen pictures obtained by the pulse echo method with normal beam inspection [36].

In the specific case of this thesis, the desired geometry in the samples that were created is very similar to element a, as shown in Figure 26. The artificially created disbonds lie parallel to the carbon fibre and titanium plates, and are therefore, perpendicular to the sound beam, making the use of pulse echo a logical choice.

Through transmission, on the other hand, may not appear as the most logical option. In most cases, to complete such an inspection, two transducers are required, one transmitter on one side of the sample, one receiver on the other side. But when inspecting the CF-188 inner wing Step lap joint, the operator does not have access to both sides. This technique will therefore only be used on lab designed samples to help characterize the artificially created disbonds as it provides one distinct advantage over pulse echo: The ultrasound waves only travel once through the sample thickness, hence the attenuation of the waves is less for through-transmission mode than pulse-echo [53]. The concept of attenuation and reflection was covered in greater detail in Section 4.3.

Through transmission provides a way to confirm if a disbond is indeed really present in the sample. If kissing bonds, and not true disbonds, are created, some sound would still be able to make its way across the sample, and therefore, give a reading. Whereas for a true disbond, no sound would go through at all; it would all be reflected by the air pocket formed inside the disbond, and therefore, nothing would be picked up by the receiving probe, as shown in Figure 27 . The use of through-transmission testing allows for a clear identification of the type of disbonds artificially created. Kissing bonds are sometimes difficult to detect with the pulse-echo method, as there is no formation of a distinct “air pocket”. Even though the material is disbonded, it is still in contact with the adherent, hence the name of “kissing bond”. With the pulse-echo method, disbonds are more likely to affect the multiple back wall echoes on an A-Scan and therefore, their discovery, when small or not fully disbonded, is subject to the operator’s experience and judgment. However, with the use of the through-transmission method, even a kissing bond will alter the intensity of the signal getting through to the receiving probe [36] making for a clear identification, as will be discussed in Section 6.5.

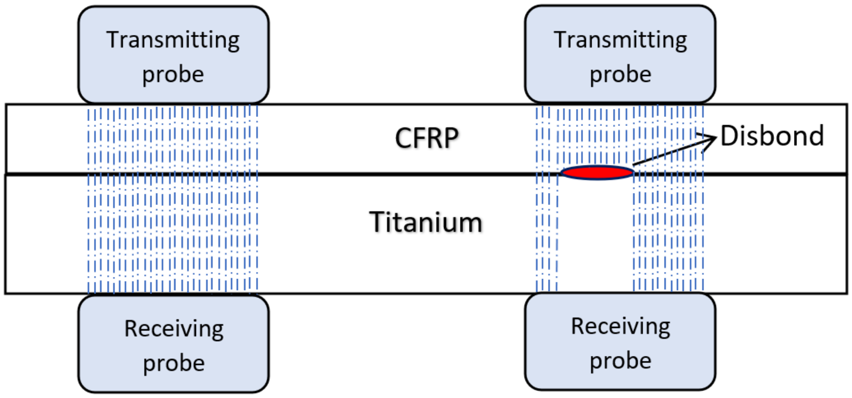

Figure 27. Through-transmission method.

## 4.7. Ultrasonic Behaviour of the IWSLJ

It was mentioned several times in Chapter 4 that the structure of the material has a direct impact on attenuation and scattering of ultrasonic waves. In this section, the acoustic properties of titanium and CFRP are individually examined, as to determine how the structure of the IWSLJ present a challenge to its inspection.

### 4.7.1. Titanium Grade 5 Ti-6Al-4V

Titanium finds considerable application in the aerospace industry and is tested ultrasonically almost as easily as light metals, such as aluminum [36]. When used in welding, there are no problems with testing rods for core or welding defects [36]. Therefore, titanium does not attenuate the signal any more than any other “common” aeronautic metal would. It is interesting to note, though, that when titanium shows signs of fatigue, the sound velocity of longitudinal waves, as well as their attenuation, are affected [54]. The higher attenuation at higher fatigue cycles may indicate an increase in the scattering of sound waves due to the increased dislocation density from fatigue [54]. It has been observed that dislocation movement migrates to the surface of the material, eventually leading to fatigue cracks. Consequently, a new field of research proposes to study changes in sound velocity as a way to monitor fatigue in titanium [54].

### 4.7.2. Carbon Fibre Reinforced Polymer (CFRP)

As already mentioned, fibre reinforced composites, such as CFRP, are notorious for having high acoustic attenuation and high ultrasonic noise [1]. Such structures are synthetically manufactured with heterogeneously arranged materials and/or threads, as is the case for the 0-90 ply layup of the carbon fibre in the IWSLJ, leading to nonlinear sound transmission [1]. The multiple reflections and interference caused by the multi-layered structure can also make signal-response difficult to decipher [2]. The impedance mismatch between the epoxy and the actual fibre also contribute to scattering and attenuation.

In Section 4.1, it was explained that longitudinal waves propagate through the thickness of a material, while transverse, or shear waves, travel in-plane. To that can be added that wave speed in the longitudinal direction is considered a material constant and can easily be calculated based on the material's density and Young's modulus. The transverse wave speed is often experimentally measured, and is always lower than longitudinal wave speed, by about a factor of 2 [55], since it is a function of the shear modulus and not Young's modulus. In the case of the IWSLJ, with a AS4 carbon fibre epoxy mix, the Young's modulus E is $11 \times 10^9$ N/m$^2$ and the density ρ is 1600 kg/m$^3$ [48] so that:

$$c = \sqrt{\frac{E}{\rho}} = 2622\,\frac{m}{s}. \tag{4.29}$$

Since the impedance, Z (kg/m$^2$s), is defined as the density of the material ρ (kg/m$^3$), times the speed of sound in that same material c (m/s), this value allows for the calculation of the impedance of the CFRP shown in Table 3.

What is interesting to note about wave propagation in CFRP, is that unless the wave penetrates the material at exactly 90°, the initial compressive beam will be converted to a shear wave and therefore, in most directions in the composite, a wave of mixed types is observed [56]. This phenomenon can be explained by Snell's law (equation 4.10): Even for a small angle of refraction, the impedance difference is so significant between the resin and the fibres [56], that what is pictured in Figure 28 is observed. This behaviour is specific to fibre reinforced materials because a disturbance generated at a fibre end will cause the wave to travel down the fibres [56]. As the structure is continuous in this direction there is little attenuation by scattering, but it must be remembered that the fibres are coupled by a strong mechanical shear to the matrix [56] and that sound travels at different speeds in the matrix and in the fibres. Therefore, the different arrival time of the wave fronts results in the interlaminar shear, and causes wave mode conversion at the interface [45].

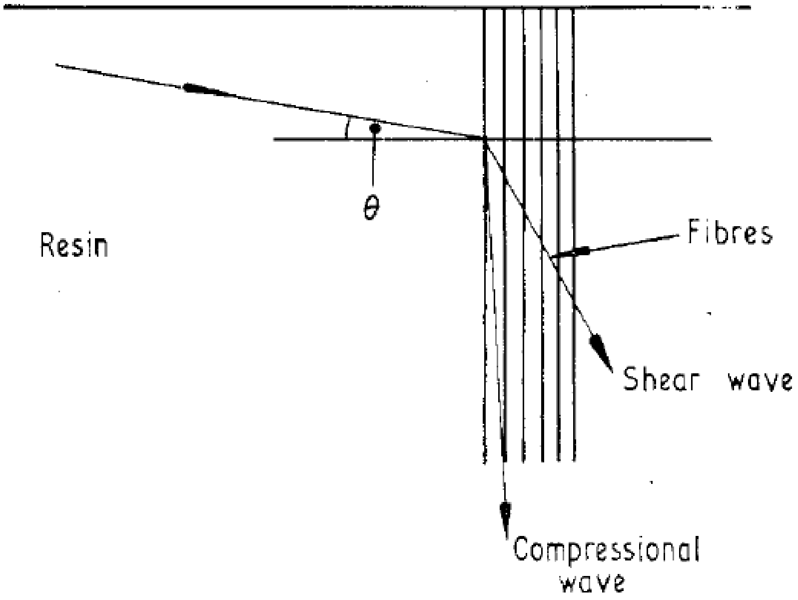

Figure 28. Compressional wave is reflected as it hits the CFRP and only a shear wave penetrates the reinforced region [56].

## 4.8. Data Presentation

When performing a conventional ultrasonic inspection, there exists three main different ways to present the data obtained: A, B and C-Scans. Section 4.6 introduced A-Scans and Figure 26 presented examples obtained from the pulse-echo method. An A-Scan is essentially a live graphical representation of the amount of ultrasonic energy received as a function of time [43]. The vertical axis shows the relative amount of energy, while time is displayed on the horizontal axis. From this form of data presentation, the reflector’s depth can be determined with equation 4.28 [57], and the size of an unknown discontinuity can be estimated by comparing the amount of energy reflected to that of a known reflector [43]. It is important to note that the vertical axis shows a relative value, and is not often referred to as a defined value with units. When comparing values on the y-axis, common practice is to consider amplitude variations, or variation in percentage, as the scales often go from 0 to 100.

The B-Scan presents a cross-sectional view based on the A-Scan. In the B-Scan, the time-of-flight of the sound energy is displayed along the vertical axis and the linear position of the transducer is displayed along the horizontal axis [43]. Since Time of Flight (TOF) is provided, it is still possible to determine the depth of a flaw, but only the linear dimension of a reflector can be estimated from this presentation. A B-Scan is usually created by setting up gates on the A-Scan. Whenever the gate is triggered by the reflected signal in the test specimen, a point is produced on the B-Scan [43]. Figure 29 shows how an A-Scan and a B-Scan would present results of the same inspection. Both scans show the Initial Pulse, IP close to time 0, and the back wall echo BW at time 9 (units are microseconds). In the case of the A-Scan, reflector A appears closer to the back wall because it is deeper in the material. Therefore more time is required for the sound to travel there and back. It can be seen on the B-Scan that reflector A appears longer than reflector B and C.

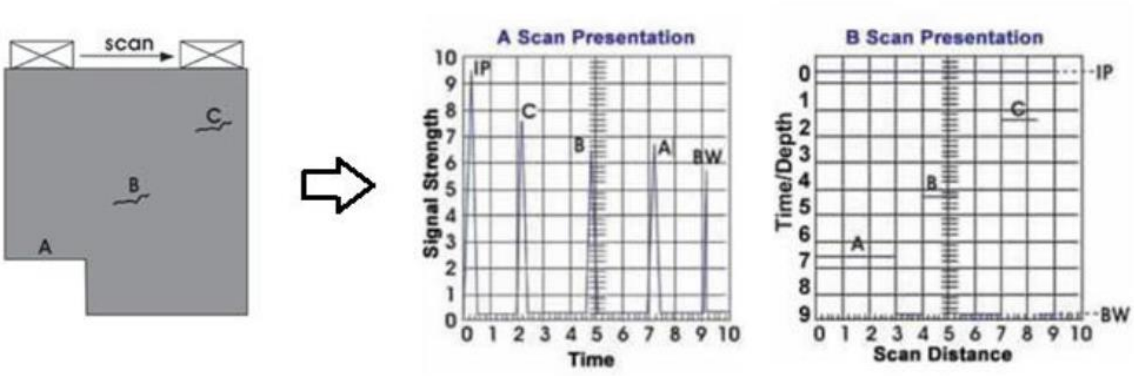

Figure 29. A and B scan Presentations [43].

C-Scan presentation provides a plane-type view of the location and size of test specimen features [43]. They are produced with an automated data acquisition system, such as ARMANDA, as computer-controlled scanning systems are required to collect and produce the image. A data collection gate is usually set up on the A-Scan and the amplitude or the TOF of the signal is recorded at set regular intervals. The relative signal amplitude or TOF is displayed as different shades of colour [43]. This results in a plane image of the test specimen, perpendicular to the transducer, showing everything that reflects or scatters sound within the specimen. This type of presentation makes data analysis easier, since one scan shows the entire specimen, compared to an A-Scan, where each square inch of the surface has to be manually covered by the operator. Figure 30 shows the difference between the three different types of scans.

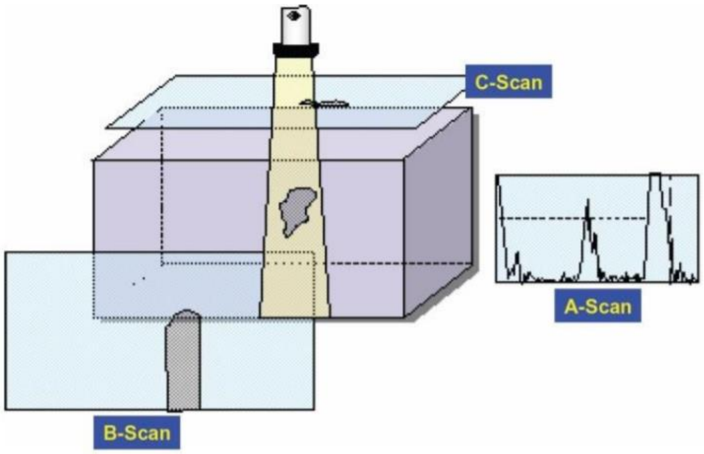

Figure 30. Different types of data presentation for Ultrasonic Testing [58].

Other types of scans exist and are associated with less conventional ultrasonic techniques. For example, Phased-Array inspections make use of sectorial scans, commonly referred to as S-Scans. This is mostly applied in medical imaging, and uses a wedge to steer longitudinal or shear waves at varying angles, creating an image in a pie shape [59]. The principles behind the image formation are very similar to that of A-Scans, but the steering capability allows for a greater possibility of detection of randomly oriented defects.

## 4.9. Ultrasonic Innovation

Pulse echo testing is a common form of ultrasonic testing in the industrial world. Its high penetrating power, the requirement to access only one surface, and its capability to estimate flaw size and depth make it a versatile technique applicable to many purposes. Of course, surface roughness, the need of trained operators and calibration procedures can put pulse echo at a disadvantage in some cases. But there exist many other ways to perform ultrasonic inspection, not only in industry, but also in other major domains like medicine. The Medical domain is driving a lot of the research and development done in UT, and as a result, Phased Array technology has become ubiquitous in hospitals as it is behind ultrasound exams. Yet it has only begun its adoption for industrial applications. Many algorithms are also developed to help enhance and denoise the results of scans conducted in highly attenuating materials, like composites. The most prominent signal processing method, Full Matrix Capture, is based on Phased Array technology.

So far, the working principles of a singular transducer have been covered. It has been explained how the vibration of the surface induces a pressure wave in a medium, and how this wave will behave at different distances from the transducer. In the case of phased array technology, all those same principles still apply, except that more than one element is fired at once. In theory, there exist an infinite number of possible geometries (and firing patterns) for a phased array probe. In practice, manufacturing costs and our ability to interpret the data collected have reduced that to three general families: linear array probes, annular array probes and matrix array probes [60]. The linear probes are the most common and are made up of elements juxtaposed and aligned along an axis [60]. The different elements of the array can be fired individually, at specified intervals, and positioned in various ways, thus creating beam steering and beam focusing capabilities.

But no matter the configuration, nearly all ultrasonic arrays have an even number of elements, such as 8, 16, 32 or 64 [61]. The reason being that it is easier to design the array controller if there are an even number of channels behaving like separate pulser-receivers. By connecting each element to separate channels in the array controller, it is possible to have some elements in receiving mode, while some are still transmitting, and vice versa [61]. This, of course, means that the array controller is a much more complicated piece of hardware that must have all the electronics for separate digital pulser-receivers for each channel, making it more expensive [61]. Furthermore, appropriate software is required to drive the array as well as calculate focal and beam steering behaviour. Generally speaking, a 32-channel array controller costs approximately ten times as much as a single conventional pulser-receiver [61].

Since linear probes are the most common, and probably the most manageable, they are the ones that will be studied in this Section. 2D-array models are eliciting interest in the research domain, and since the early 2000s, are becoming more common [62]. If a number of elements are put side by side and are firing the same pulse at the exact same time, the ultrasound beams formed by each element will interact and merge with one another. Thus, if the phased array probe uses all its elements at the same time, it will behave just like a “normal” probe and create a compression wave at 0°; that is perpendicular to the material surface [61]. The total length of a linear array is defined as:

$$L - (N - 1)\delta e_{c-c} + w_e. \tag{5.1}$$

Where N is the number of elements in the array, $\delta e_{c-c}$ is the centre-to-centre spacing between elements and $w_e$ is the width of the elements. The main advantage of a 1D linear array is the capacity to steer and focus the beam by applying a time delay to the elements. Figure 31 shows how the implementation of a time delay can create a) beam steering and b) beam focusing [60].

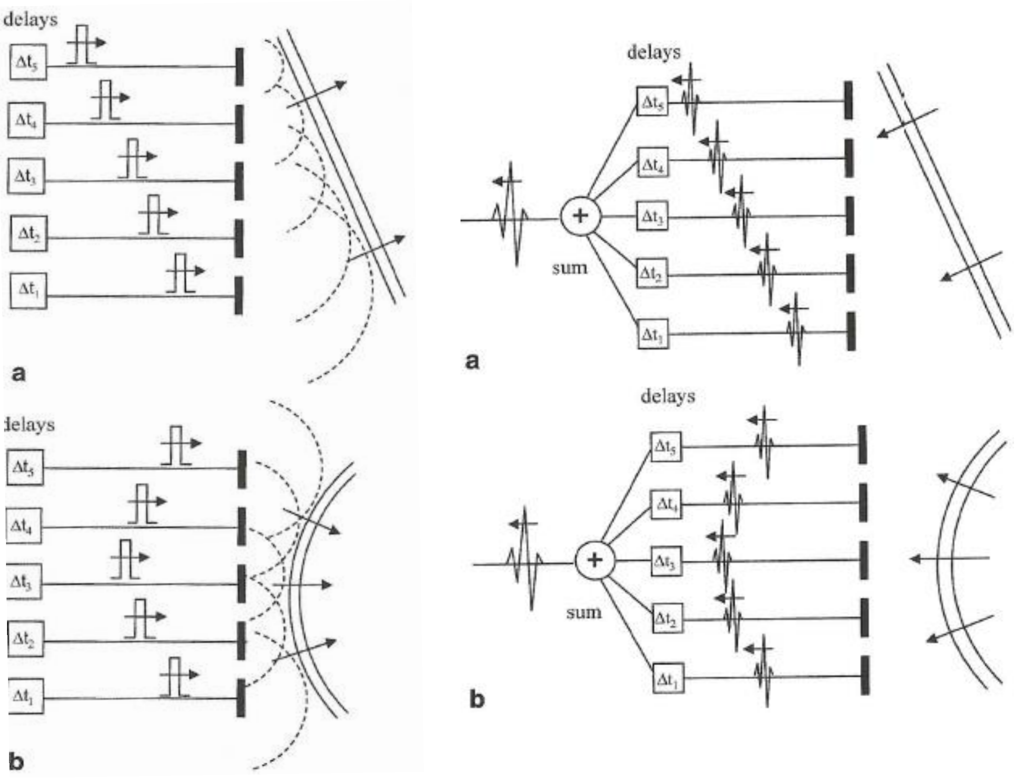

Figure 31. Impact of time delay applied to individual channels to create (a) Beam Steering and (b) Beam Focusing [63].

Mathematically, the time delay $\delta t$ applied to each element in case of (a) beam steering is much simpler than in case of (b) beam focusing. All the information required is 1) the angle desired $\theta_s$, 2) the centre-to-centre spacing between elements $\delta e_{c-c}$, 3) the frequency and 4) the wavelength of the pulse [60]:

$$\delta t = \delta e_{c-c} \frac{sin\theta_s}{c}. \tag{5.2}$$

As an example, a beam at 45° in titanium (c= 6090 m/s) is desired and a probe of 8 elements spaced by 0.5 mm is available, then the first element would fire at $\delta t_1 = 0$, the second at $\delta t_2 = 58\, ns$, and the last one would fire at $\delta t_8 = 406\, ns$. One important thing to note is that this produces a compressional wave at an angle, and not a shear wave. It is therefore different from putting a conventional probe on an angled wedge. It is, however, possible to create steered shear waves with phased array technology by also putting the phased array probe on the angled wedge, but the calculation of time delays and interpretations of results is much more complicated [61].

It is important to note that the different zones of the sound field that were studied in Section 4.4 still apply here. Huygens's principle is still valid, and the far field will still present a much more even pressure distribution. Thus, it has been stated [63, 62] that little to none image improvement would come from focusing the beam in the far field. Equation 4.16 can be adapted [62] to phased arrays so that the transition zone between near and far field is:

$$N = \frac{D^2}{4\lambda}, \tag{5.3}$$

where $D^2$ is the overall dimension of the array (instead of the probe diameter) and λ is the wavelength. Some examples using of beam steering and focusing in the near and far field were simulated by Azar et al. [62] using a 32-element array with a centre-to-centre element spacing of λ/2, a frequency of 2.25 MHz, and a wave speed of 6320 m/s. The transition depth N between the near and far field in this specific case was at 18 cm.

First, Figure 32 shows the beam steering behaviour in the near and far field. The specific depths are set at 10 and 50 cm. The beam is steering at 30° [62]. The two images (a) at the top show the main beam at the set angle, while also showing beam spreading. The bottom images (b) show a 2D representation of the main lobe and associated side lobes (see Section 4.4 and Figure 23). A sharp lobe and small side lobes indicate good image resolution and a higher intensity. In the near field, it can be observed that the steering quality is poor, due to the wide and irregular shape of the main lobe. It would be impossible to properly map the received signal from this region, because resolution is dictated by the sharpness of the main lobe [62]. On the other hand, the resolution in the far field is much better, and a clear mapping of the zone can be established [62].

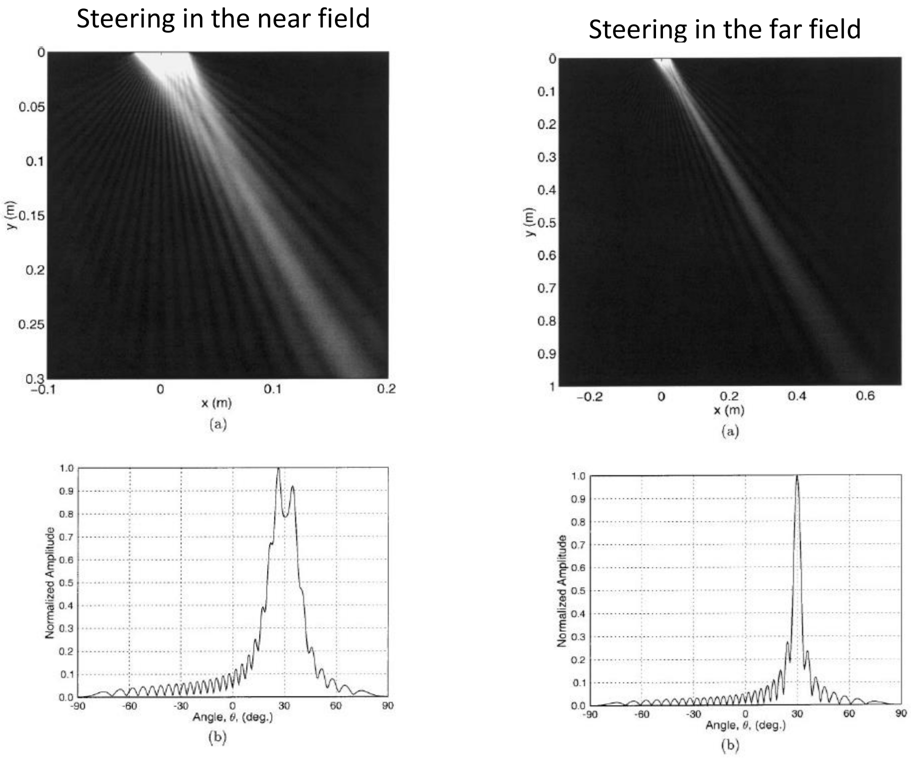

Figure 32. Beam steering behaviour in the near and far field [62].

Figure 33 shows beam focusing behaviour in the near and far field. The depths are the same, 10 and 50 cm, and while the beam is being focused, it is also steered at a 30° angle [62].

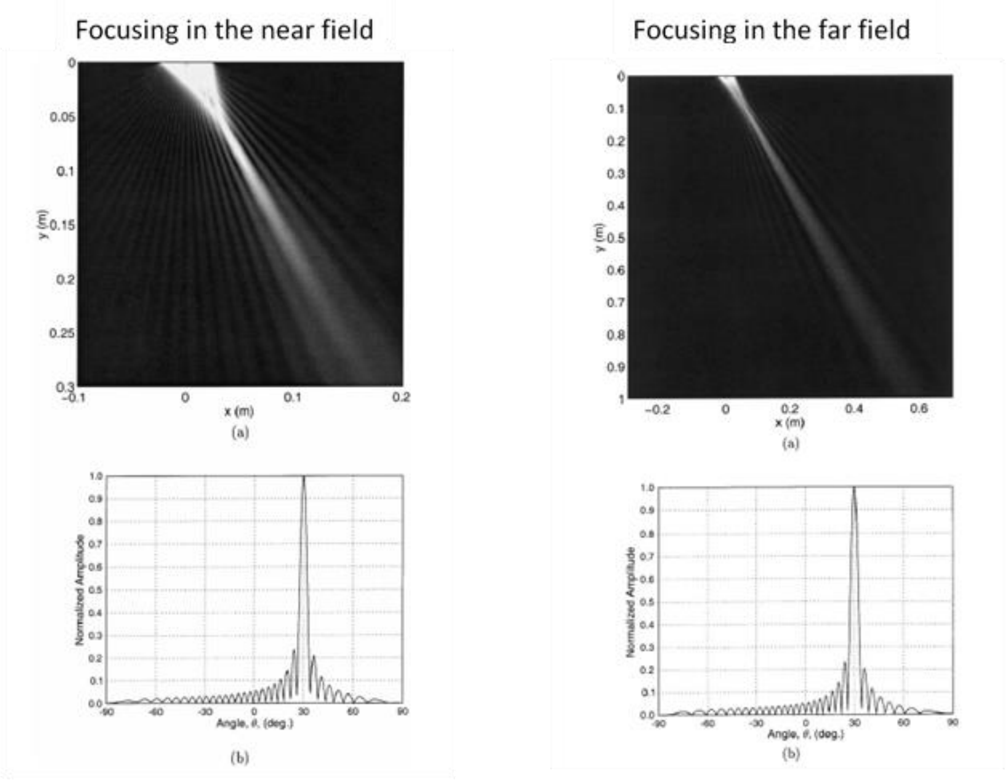

Figure 33. Beam focusing behaviour in the near and far field [38].

When comparing both near field measurements of Figure 32 and Figure 33, it can be observed that focusing the beam greatly improves the results that were seen in Figure 32 [62]. Focusing enables the acquisition of data in the near field, which is otherwise impossible by steering only, while also improving resolution [62]. In the far field, however, the benefits of focusing are not really visible over beam steering [62].

With all the advantages that phased array technology has to offer, it might be surprising that it is not one of the go-to techniques to inspect the IWSLJ. But it is important to take into consideration that phased arrays are not only more expensive, but also more complex. They are quite a bit more difficult to operate than a conventional ultrasonic testing equipment, thus requiring more training, and first-time set-up and calibration are much more intensive compared to a simple pulse-echo scan [64]. A very good understanding of beam behaviour is required to interpret the data and to determine when to apply beam steering, focusing or both. Focusing the beam at too shallow a depth can mean that deeper discontinuities may be missed [64], and inappropriate steering may lead to missed flaws as not all discontinuities are necessarily oriented in a favourable direction [64], as was explained in Section 4.6. Although PAUT presents the same disadvantage as pulse echo testing (need for calibration and highly trained operators, susceptible to surface roughness and inhomogeneous materials), beam steering and the possibility to adjust the focal length are strong advantages of phased array.

In-homogenous materials such as multiplies composite structures like the CFRP present on the IWSLJ are inherently anisotropic resulting in varying UT wave propagation speed per angle [65]. This does not guarantee that phased array will produce better results than conventional UT. The vertical part of the steps presents the area that would most benefit from a phased array inspection. But all the challenges that come with fibre reinforced composites still apply. This means that the initial compressive beam will be converted to a shear wave because it won’t be entering the material at 90$^{o}$ (recall Section 4.7). The beam would also need to be precisely focused on either the vertical or horizontal part of the step, otherwise a part of the signal will bounce back in different directions, and this could potentially be interpreted as a signal drop caused by a disbond.

Section 4 explained how the propagation of an ultrasonic wave is influenced by many factors, including the signal frequency, the distance travelled by the signal, the position, orientation and size of defects, as well as the material’s structure. All those factors can influence the resulting signal from an ultrasonic inspection and can introduce a fair amount of backscattering noise. Another possible source of noise is the electronic circuitry inside the instrument. All this noise is usually visible as “grass” on the CR screen, and when inspecting highly attenuating materials such as composites, it is possible for signal reflections to get lost in that grass. This has led to the appearance of many denoising algorithms over the last 40 years, all with the intent of making signal interpretation easier [66].

Ultrasonic flaw detectors have simple signal processing options pre-implemented in their hardware, such as analog filtering (more recent detectors are equipped with digital filtering), transducer damping, or improvement of spatial resolution in the presence of multiple reflections [67]. But in some cases, those basic noise filters are not enough. There exist many other filtering methods applicable to pulse-echo A-Scans signals, and many more denoising techniques exist based on the type of scan performed. Such algorithms are not implemented in the hardware used for the scan, and have to be applied on the raw data collected by the equipment.  It is not uncommon for researchers to combine different denoising methods based on the complexity of the part that requires inspection and the noise present in the signal. In 2017, Tiwari et al. [68] combined three algorithms to filter inspection results from a wind turbine blade of glass fibre reinforced polymer composite. Given the one side of access, the nature of the material, and the special configuration of the wind turbine blade (all conditions similar to the inspection of the IWSLJ), they found that their hybrid signal processing method considerably increased the accuracy of disbond detectability [68].  Choosing the right algorithm to use, or the right ones to combine, is a matter of material's intragranular structure, as well as the desired data presentation. The possibility to apply one of these algorithms to IWSLJ inspection results is something for future research.

# 5. Experimental Work

It is known that composites, like CFRP, are difficult to inspect ultrasonically primarily because of their attenuative nature. Therefore, challenges to the inspection of the lap joint are introduced, because of the varying thicknesses of the CFRP panels over the different steps. Ultrasonic parameters, such as sound pressure, attenuation, signal-to-noise ratio and frequency selection are examined in this section. This will allow for selection of optimal parameters for the inspection of the IWSLJ.

The current inspection procedure for the IWSLJ, using the EPOCH 600©, focuses solely on the detection of complete disbonds over Steps 1 and 2, and delaminations on the outboard edge of the titanium splice plate. However, it is also known that before disbonds are formed, an intermediary stage, called a kissing bond, occurs. Section 2.2 explained how kissing bonds are defined by partial failure of the adhesive holding two adherents together, whereas a complete failure of the adhesive is observed for full disbonds. In this chapter, the impact of kissing bond on bond strength is looked at, through the ASTMD1002 [7] The possibility to detect kissing bond with the same ultrasonic technique used for the inspection of the

IWSLJ is investigated, using the optimal UT parameters determined in this section. Results obtained are compared with inspection images obtained using the ARMANDA system.

## 5.1. Fabrication of Samples

In order to better achieve the goals of this thesis, a calibration block, currently used in the inspection of the IWSLJ was used to investigate the impact of the stepped geometry on UT parameters. In addition, two samples were fabricated in laboratory. In Sample No. 1, attempts where made to insert kissing bonds, while in Sample No. 2, the creation of full disbonds without using FBHs was investigated. Additionally, ten coupons were created to investigate the impact of kissing bonds on total bond strength. This section describes the specific dimensions and parameters of the calibration block and outlines how each sample was manufactured.

### 5.1.1. IWSLJ Calibration Block

Although the calibration block had flat bottom holes drilled in the back, to simulate defects, it was used as a reference point, as it was the closest thing to a real F/A-18 wing available. One of the flat bottom holes was located over Step 2, where the CFRP thickness was similar to the one of Sample No. 2, allowing for a reasonable comparison of the two samples. As was mentioned in Section 4.7, the sandwiching of titanium and CFRP, combined with the particular shape of the inner wing stepped lap joint, makes for a very challenging inspection and interpretation of the results. Figure 34 shows the IWSLJ calibration block under different angles; (1) shows the surface being inspected, with Point A being only titanium, Point B being over Step 1 and point C over Step 2. Points D and E are used to calibrate for delaminations; (2) shows the flat bottom holes on the back of the calibration block; while (3) shows a side view of the block. All points, with the exception of Point A, are present in pairs. According to [5], the ones circled in red represent the disbonded/delaminated area, whereas the black circles represent good bonding. Point A is different because it is only used during the calibration steps outlined in [5].

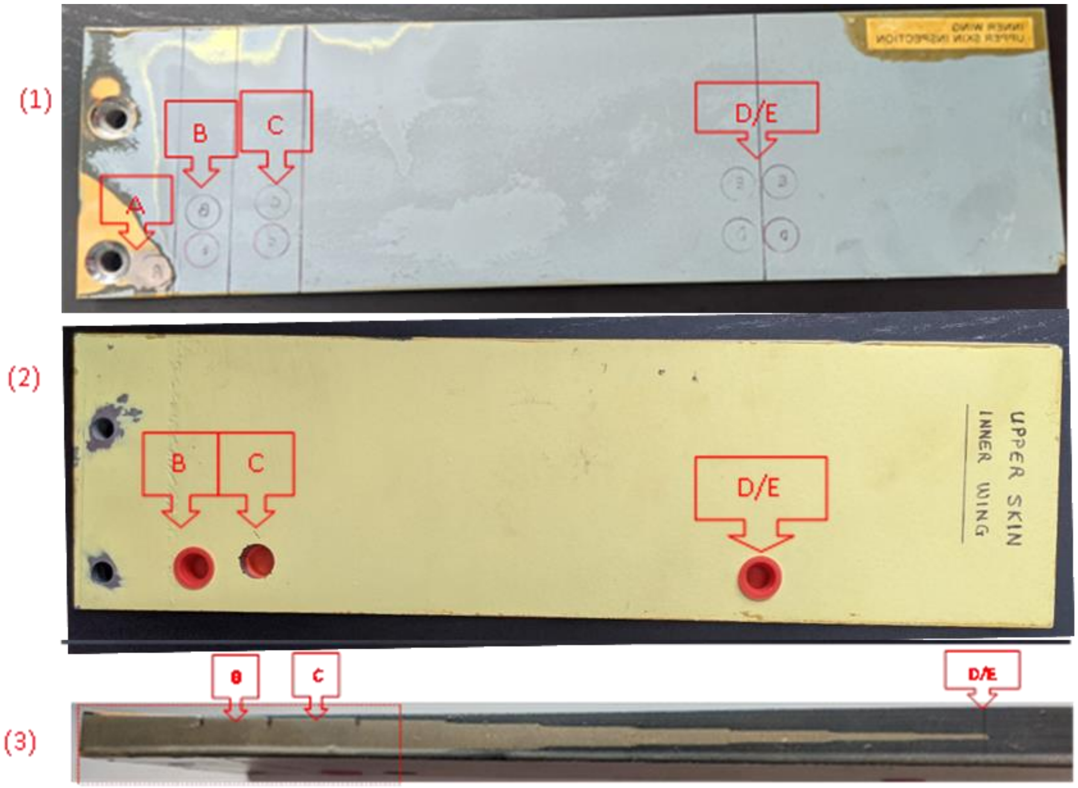

Figure 34. IWSLJ calibration block (1) top view (2) bottom view (3) side view with inspection points (A) titanium (B) Step 1 (C) Step 2 (D/E) Step 9.

The F/A-18 wing has two lap joints, one on top, and one at the bottom, appropriately named the Upper and Lower IWSLJ. Each IWSLJ has two CFRP-titanium interfaces, called the Outer Mold Line and the Inner Mold Line (OML and IML). Figure 35 shows a cross-sectional view of a wing, with the upper and lower IWSLJ. While conducting IWSLJ inspection in a normal context, the IML cannot be directly accessed for inspection. Sound has to travel through the first layer of CFRP, hitting the OML, then go through the titanium before hitting the IML. Because CFRP is highly attenuating, detecting disbonds on the IML is difficult. As Table 4 shows, only 19% of the original impulse makes it to the IML. If a disbond is present at the IML and the signal is reflected towards the transducer, only 8% of the original pulse will be detected, compared to 42% for a signal reflecting off the OML.

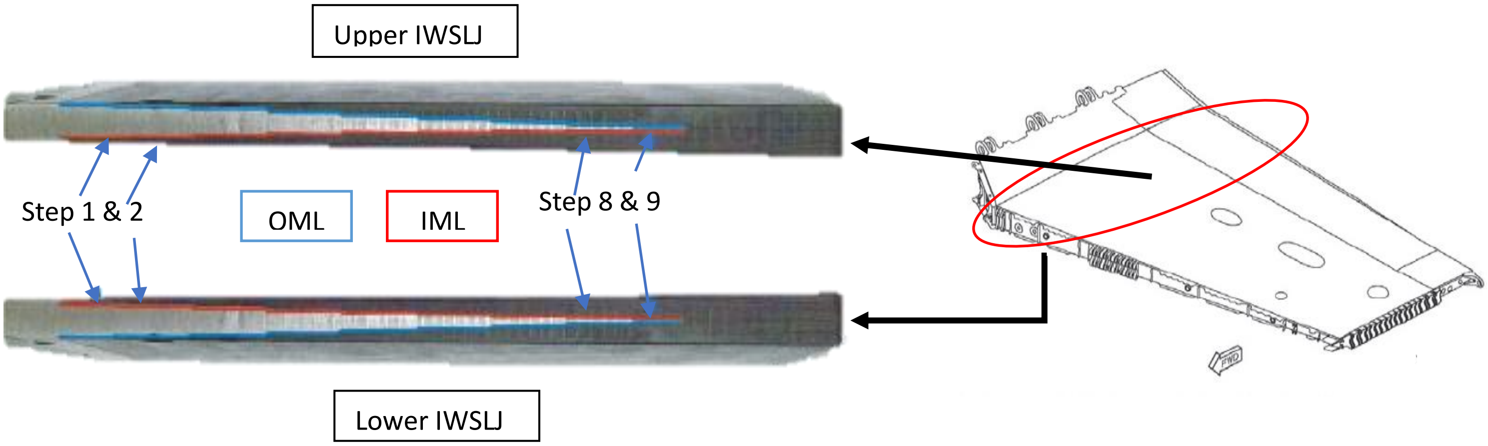

Figure 35. Location of the IML and OML with regards to probe placement during inspection [5].

The varying thicknesses will become important for interpreting results in the next few sections. Table 5 provides characteristics of the steps, with titanium and CFRP thicknesses given for each step, as well as the respective TOF required to reach the OML, IML and back wall at each step. Note that an instrument error of ± 0.5 mm is possible for the thicknesses, and that TOFs were calculated with equation 4.28.

Table 5. Step dimensions with thicknesses and TOF.

| Step No. | CFRP thickness on one side (mm) | Titanium thickness (mm) | Total thickness (mm) | TOF to OML (µs) | TOF to IML (µs) | TOF to back wall (µs) |
|---|---|---|---|---|---|---|
| 1 | 0.5 | 11 | 12 | 0.38 | 4.01 | 4.39 |
| 2 | 1 | 10.7 | 12.7 | 0.76 | 4.29 | 5.05 |
| 3 | 2 | 9 | 13 | 1.53 | 4.49 | 6.02 |
| 4 | 3 | 7.5 | 13.5 | 2.29 | 4.76 | 7.05 |
| 5 | 4 | 6 | 14 | 3.05 | 5.03 | 8.08 |
| 6 | 5 | 5 | 15 | 3.82 | 5.46 | 9.28 |
| 7 | 6 | 3.5 | 15.5 | 4.58 | 5.73 | 10.31 |
| 8 | 7 | 2 | 16 | 5.34 | 6.00 | 11.35 |
| 9 | 7.5 | 1 | 16 | 5.73 | 6.05 | 11.78 |

Knowing the exact dimensions and location of each step is important. When following the guidelines of [5], while getting ready to conduct an inspection, the procedure for the pulse-echo inspection has the inspector manually drawing on the wing the position of the steps [5]. This is critical to a good signal interpretation, because if the probe is aligned on the edge of the step, while the inspector thinks it is completely over a particular step, it might lead to a “false positive” reading: the end of the probe over the deeper step is going to transmit a different signal than the end over the original step. Therefore, the signal of the initial step will come back early, in a fashion similar to the response signal from a disbond. As an example, the probe was intentionally set up over Steps 3 and 4 in Figure 36. The “in between” response is looking very similar to the kissing bonds presented in Section 6.5, meaning that the number of peaks is not going to change, but rather the amplitudes are going to decrease significantly. If the operator/inspector is not careful, this could lead to a false positive.

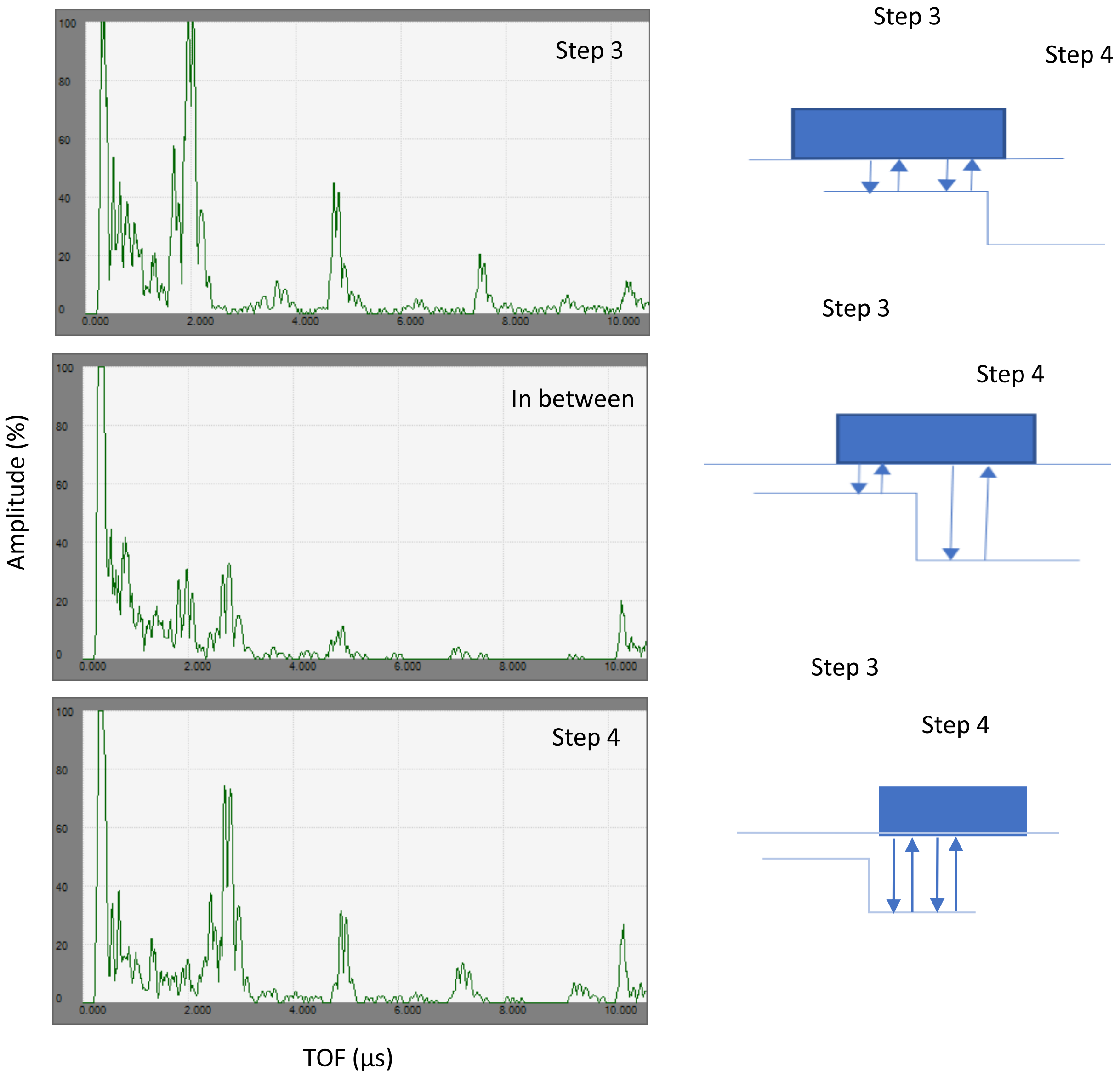

Figure 36. Importance of probe alignment over the steps, showing A-Scans of Step 3, in between Step 3 and 4, and Step 4 with representation of probe alignment.

### 5.1.2. Sample No. 1

An attempt to introduce kissing bonds into Sample No. 1 was made by adding various inserts between the titanium and adhesive, as well as by varying surface preparation prior to bonding. Sample No. 1 was made square with dimensions of 177.8 mm x 177.8 mm (7” x7”), and was comprised of a grade 5 Ti-6Al-4V sheet 6.35 mm (1/4”) thick, and a CFRP panel of 14 plies with a 0-90 ply layup, which gives it a thickness of 2.1 mm.

To begin sample No. 1’s preparation, a grid was drawn on the titanium plate: one line in the middle, then two inches on each side. This grid system was later used when creating the deffects and also when taking measurements to map defect locations. It gave an indication of which defect was supposed to be where. Small indentations were made on the sides with a bench saw, where the lines were, and two corners were cut: one with a saw and another sanded, to allow the sample to always be placed in the same orientation.

A 12.7 mm (½”) hole was drilled in the middle of the titanium plate, to serve as a calibration point. This diameter was selected because the same diameter is used on the CF-188 calibration block, also studied in this thesis. Then, following recommendations from the literature [23] [69] [70], the titanium alloy plate was thoroughly cleaned in order to properly prepare the surface for the next step of sample preparation. Neodisher LaboClea A8™ was used as a cleaner in this case. The sample was then grit blasted with silica, with the exception of three squares protected by masking tape, as shown in Figure 37 (a). The purpose of the non-grit blasted areas was to facilitate the creation of disbonds. Similarly, while still observing the recommendations of the literature [23] [70], the CFRP panel was sanded with 600 grain sand paper, except for a 63.5 mm (2 ½”) strip, as can be seen in Figure 37 (b). Again, since an increased surface roughness creates a better bond, [23] the bond should be weaker in the area of the strip, and therefore, the disbonds easier to locate.

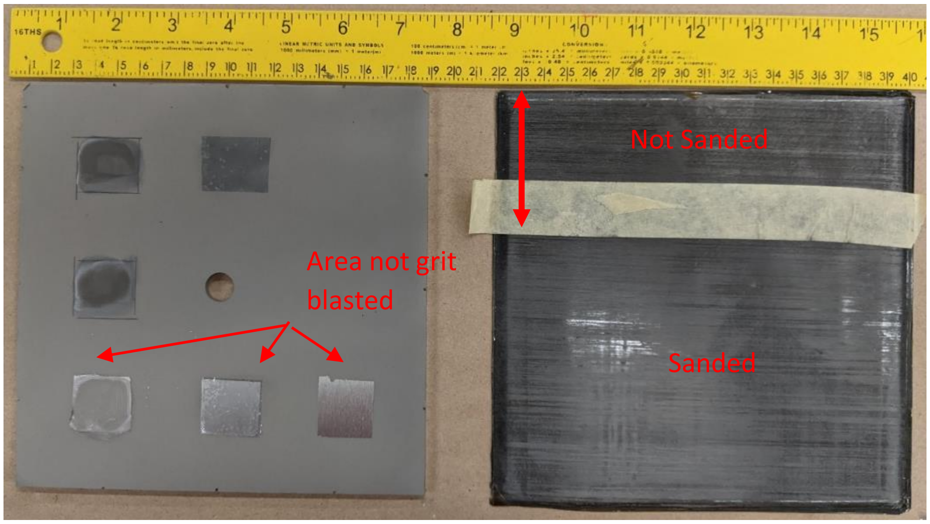

*(a)* *(b)*

Figure 37. Titanium and CFRP surface prepared for bonding (a) shows Titanium areas not grit blasted (b) shows CFRP strip not sanded.

After this, referring to the previously developed grit system, and using the indentations made on each side of the titanium sheet, the “defect layout” was developed. Figure 38 shows a map of the artificial defects created, and indicates for each one from top to bottom, its designated number for future reference, the insert used to create a disbond (mold release, thermal tape, nothing), the surface preparation of the CFRP and the surface preparation of the titanium. On the far right column, which corresponds to defects 1.3, 1.5 and 1.8, no disbonds were inserted, only the surface preparation was changed. Pieces of thermal tape were added to defects 1.2 and 1.7. Mold release wax, Gringnard™ Mold Magic™, was applied to defects 1.1, 1.4 and 1.6. Mold release has a melting point of 260 degrees Celcius so it can resist the epoxy cure of 120 degrees Celcius. FBH 1 correspond to the 12.7 mm (½”) hole mentioned above.

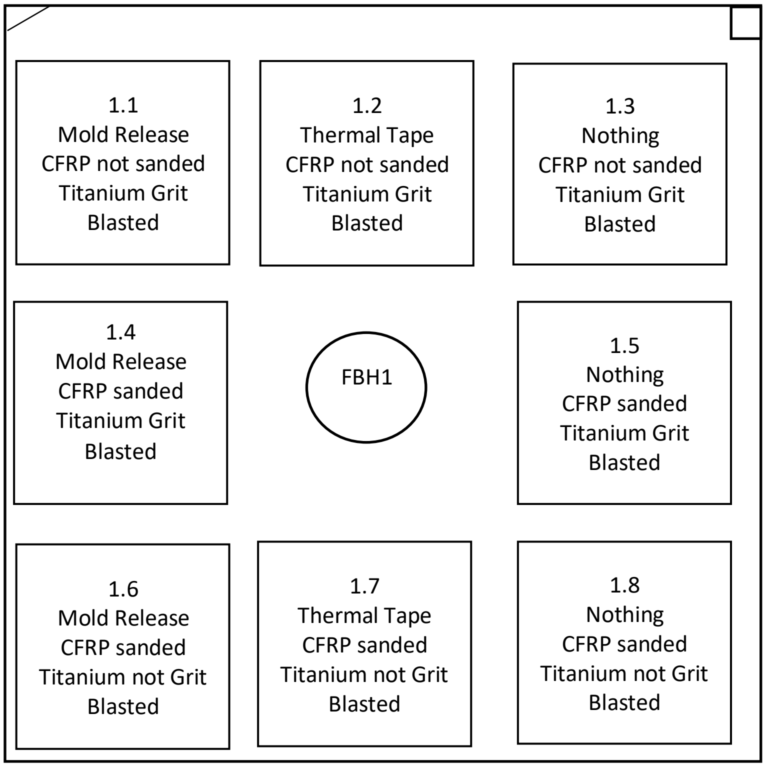

Figure 38. Disbond layout of sample No. 1 showing from top to bottom: material used to create disbond, surface preparation of CFRP, surface preparation of titanium.

Once the disbonds were created, the CFRP and titanium were ready for bonding. A 177.8 mm x 177.8 mm wide (7" x7") square of 3M™ Scotch-Weld™ Structural Adhesive Film AF 163-2 was first put on the titanium sheet shown in Figure 37(a), then the CFRP panel shown in Figure 37(b) was put on top. The composite structure was then put under a vacuum, at 880 Millibar (26 inches of Mercury), and cured at 120 degrees Celsius for 2.5 hours.

### 5.1.3. Sample No. 2

Sample No. 2 was made square, with dimensions of 152.4 mm x 152.4 mm (6" x6") The titanium sheet was 2.54 mm (0.1") thick and the CFRP panel was 1.7 mm thick. The CFRP thicknesses of both samples is similar to that of Step 3 on the IWSLJ.

Sample No. 2 was prepared in a similar fashion to Sample No. 1. The same adhesive was used, and cured the same way. A grid system was also developed, but this time the entirety of the titanium sheet was grit blasted, and the entire CFRP panel was sanded. The goal was to improve on the defects introduced in sample No. 1, investigating if kissing bonds reflecting a higher percentage of sound could be achieved by layering 2 and 4 sheets of thermal tape and applying 3 layers of mold release, or if these additions would result in the creation of complete disbonds. One layer of Teflon tape was also added to Sample No. 2, to see if this insert would create a kissing bond. Additionally, holes of varying dimensions were cut into the adhesive used to bond the titanium to the CFRP. It was anticipated that the adhesive will run and fill the holes back up during curing, but to an unknown extent; hence the varying diameters. It was hoped that by completely removing the adhesive layer, the realism of the artificial disbond and the likelihood of the formation of the air pocket would be increased. This could potentially be used to replace the use of FBHs during training, as the defects would be invisible to the naked eye. Figure 39 shows the disbond layout of sample No. 2, as well as what the sample looked like before the CFRP panel was added. The holes cut out in the adhesive (defects 2.2, 2.5 and 2.8) are visible, as well as the other inserts underneath. Similarly to Sample No. 1, a FBH was also introduced in Sample No. 2, labeled FBH2. However, note that the hole was drilled in the titanium after the panel was assembled, hence why it is not visible on Figure 39(b).

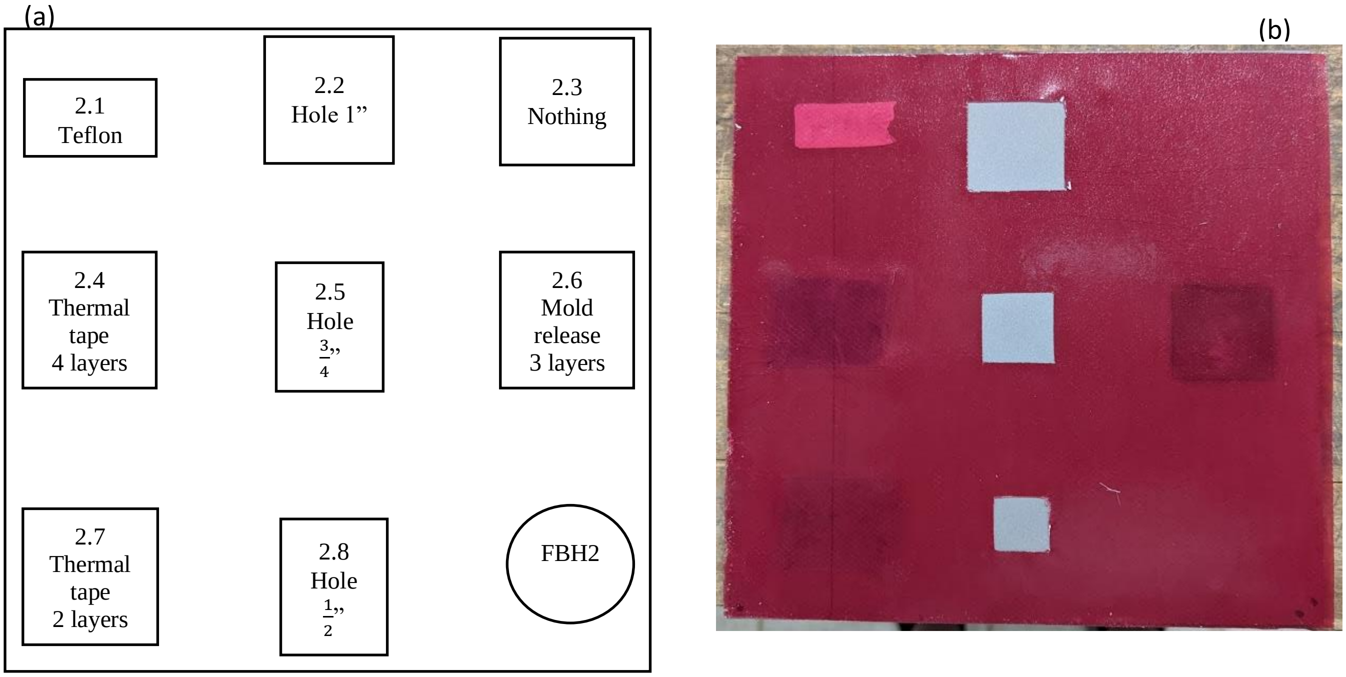

Figure 39. Disbond Layout of Sample No. 2 showing material used to create disbond (a) graphically (b) before the addition of the CFRP panel.

## 5.2. ASTMD1002 coupons

Figure 40 shows the required dimensions for a test specimen. For the case of this thesis, the thickness of the titanium sheet used was 3.18 mm (1/8”) and the overlap measured 12 mm (≈ 1/2”).

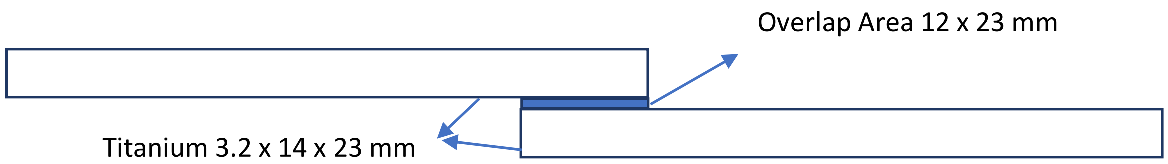

Figure 40. Dimension of a single lap joint coupon.

Ten coupons were created in accordance with the dimensions specified in [7]. The same adhesive used for Sample No. 1 and No. 2 was used for those coupons. Six were created with no disbonds, and used as a reference for the average strength of the bond, and four samples were created with disbonds covering 100% of the overlap area: two disbonds were inserted using one layer of thermal tape, and two with mold release, in the same fashion as described in Section 5.1.2. The titanium covering the adhesive was grit blasted on both sheets. Samples were then cut in 25.4 mm (1”) wide strips with a band saw. Figure 41 shows the adhesive line used to bond the two titanium sheets together and the complete panel, prior being cut in strips.

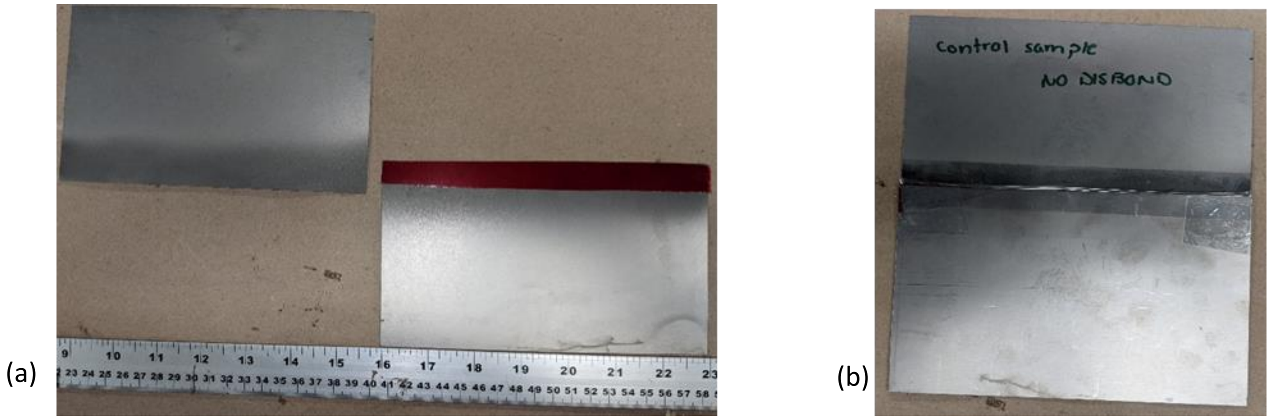

Figure 41. Assembly of test coupon (a) showing the adhesive line and (b) panel fully assembled.

# 6. Ultrasonic Parameters

In this chapter, multiple factors impacting ultrasonic measurements are looked at. First, the near field effect and the impact of a delay line on sound pressure are looked at. Then sound attenuation, followed by signal-to-noise ratio are investigated. The last parameter being looked at is frequency selection. Once the impact of these parameters has been assessed, detection of kissing bonds with ultrasonic testing is attempted. Lastly, results obtained from Sample No. 1 are compared to inspection data obtained from real F/A-18.

## 6.1. Near-field effect and delay line

In Section 4.4, the differences between near and far fields were explained and it was made clear that due to wave interference and constant changing amplitude, the near field should be avoided when doing ultrasonic testing, especially when working with really thin materials or when trying to identify defects that are close to the surface. This section explores in greater details the impact of pressure fluctuations on UT measurements and investigate if a delay line can be used as a mitigating factor.

In order to determine the near-field length, the probe frequency and diameter must be known. In the case of this thesis, a transducer of 6.35 mm (0.25”) diameter was used and three different frequencies, 2.25, 5 and 10 MHz, were employed. This information was used with equation 4.16 to populate Table 6, which shows the near field length at those different frequencies.

Table 6. Near field length in CFRP and Titanium at varying frequencies

| | 2.25 MHz | 5 MHz | 10 MHz |
|---|---|---|---|
| CFRP | 9.2 mm | 19.3 mm | 38.7 mm |
| Titanium | 3 mm | 8 mm | 16.5 mm |

Knowing where the near field ends is important, because as it was already mentioned, inspections in this region can be challenging. It was shown in Table 5 that the IWSLJ varies in thickness, from 12 mm over Step 1 to 18 mm past Step 9. The CFRP panels covering the titanium splice plates also vary in thickness, from 0.5 mm over Step 1 to 7.5 mm over Step 9. Recall from Section 4.5 that the last pressure null occurs at about half a near-field distance from the transducer. While the far field is preferred to conduct ultrasonic testing, it is assumed that the area past that last null, at about half a near-field distance, would not interfere as much with ultrasonic measurements. Therefore, regardless of the frequency used, all ultrasonic measurements of the OML from Steps 1 to 5 l will be in the first half of the near-field. A possible mitigating factor is the introduction of a delay line. Made of a sound conductive plastic, its primary function is to introduce a time delay between the generation of the sound wave and the arrival of the reflected wave. Not only does this virtually shift the near field up, as shown in Figure 42, it also allows the transducer enough time to properly "send" the sound wave before it has to receive the echoes. This results in a much higher near-surface resolution [71].

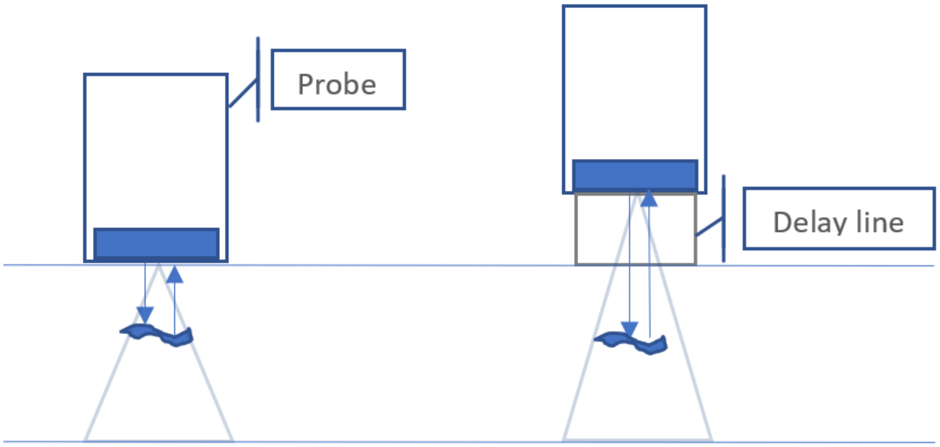

Figure 42. Function of a delay line when searching for surface flaws.

Figure 43 shows how pressure fluctuations will vary, when transitioning from one material to another, when inspecting the IWSLJ with and without a delay line. If no delay lines are used, the OML would be located at the very beginning of the near field, where pressure is rapidly changing. No matter what frequency is used for the inspection, it is logical to add the use of a delay line to increase detectability rate on the OML.

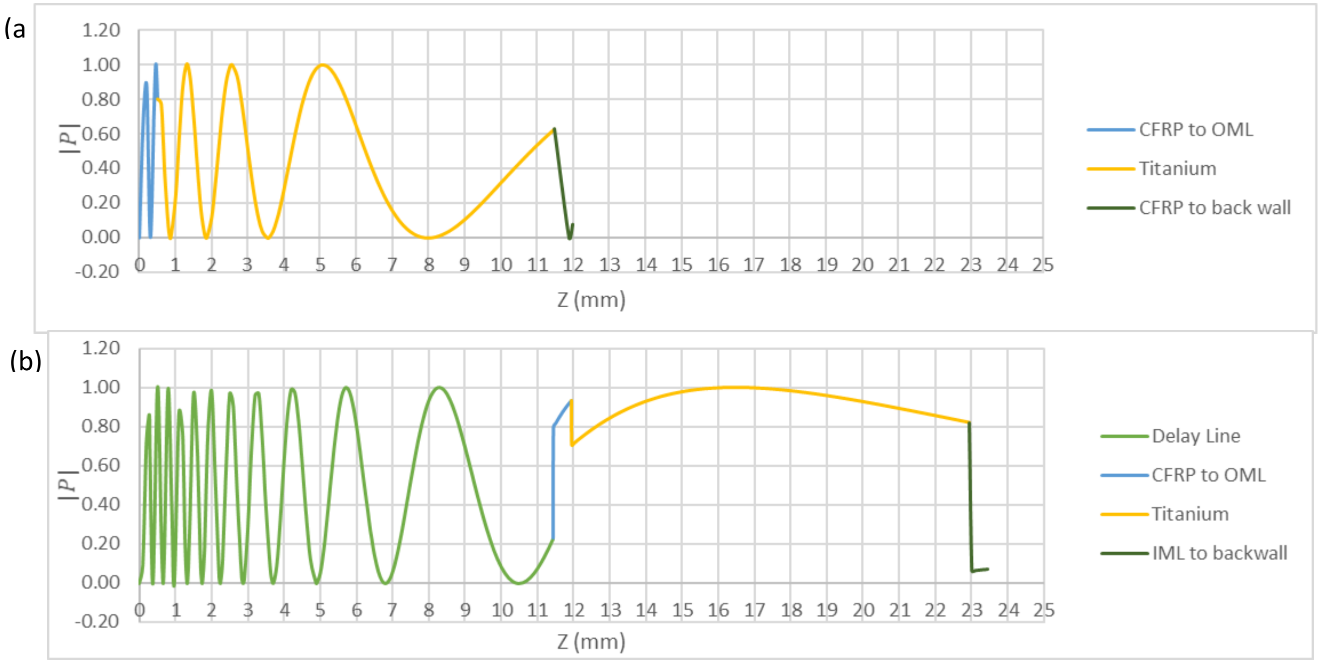

Figure 43. Magnitude of the normalized on-axis pressure for a plane piston transducer STEP 1 (a) without and (b) with a delay line.

The impact of a delay line can also be seen when looking at A-Scans, and minimizing pressure fluctuations could also help to detect IML disbonds. Figure 44 shows the A-Scan of Point B on the IWSLJ calibration block (see Figure 34) with and without the delay line, at 10 MHz. It can be seen that when the delay line was used, background noise is reduced. It also means that the back wall reflection is more distinct with the delay line, whereas without it, the back wall reflection can be confused with background noise. The current inspection procedure [5] is performed live; the operator observes the CR screen while conducting the inspection, and looks for a significant signal loss similar to what is obtained with a FBH. Reducing pressure fluctuations and background noise could help identify kissing bonds on the IML by making the echoes more evident. Note that the scans shown in Figure 44 were taken at 10 MHz, even though this frequency produces the longest near field. The reasoning being this choice is explained in Section 6.3.

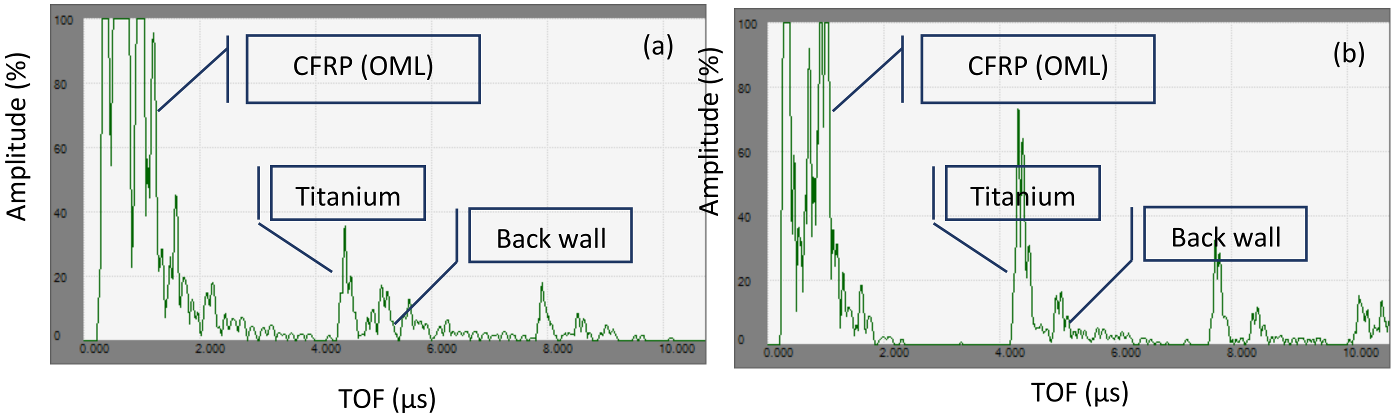

Figure 44. Background noise levels (a) without the delay line (b) with the delay line of Step 1 at 10 MHz.

Longer delay lines than the one used for this thesis are available. However, the 11.43 mm one is common in UT inspection kits. The ARMANDA system uses a custom delay line 2.54 cm (1 inch) thick, thus ensuring no rapid pressure fluctuations occur during the automated inspection. It is also possible to change the diameter of the transducer. However, using a larger transducer would also move the end of the near field further away from the transducer, thus offsetting the benefits of a possibly longer delay line (see equation 4.16). If a transducer of 6.34 mm in diameter is used, then a delay line (made of polystyrene) of 21 mm of longer would be optimal, since the first half of the near field would be entirely in the delay line.

When using delay lines, reflections will occur when the sound beam enters or leaves the delay line. This leads to unfavourable signal overlaps with possible visible echoes, sometimes referred to as front wall echoes, making interpretation of the scans more challenging [72]. According to the manufacturer's website [73], the delay line used for this paper is made of polystyrene. Knowing that the delay line used for this thesis is 11.43 mm long, equation 4.28 was used to determine that sound takes 9.7 µs to travel through it, which is in agreement with the manufacturer's specification of 10 µs [73].

When following the calibration procedure in [5], the probe is first aligned over point A (see Figure 34), which is only titanium all the way across. The impedance of titanium is much higher than CFRP, and in this case 70% of the sound is reflected at the delay line-titanium interface. Figure 45 shows an A-Scan taken at point A, which is the only one not covered by paint or CFRP. Peaks are showing at approximately each multiple of 4 µs, while slowly decreasing in intensity, representing the multiple echoes of the titanium. The delay line introduces a delay of 10 µs, so the peaks at 10 and 20 µs represent front wall echoes. The peaks at 14 and 18 µs are also front wall echoes, as each peak happen to be 10 µs after a titanium echo. In Figure 45, the main pulse sent through the titanium creates a front wall echo at 10 µs and a back wall echo at 4 µs, Internal reflections inside the titanium are responsible for the echoes observed at 8, 12, 16 and 20 µs. The additional front wall echoes observed at 14 and 18 µs are also due to internal reflections; it takes 4 µs for a sound beam to travel through the titanium, and an additional 10 µs for sound to travel through the delay line. Because 70% of the sound wave is reflected at the delay line-titanium interface, it explains why the front wall echoes have such a high amplitude.

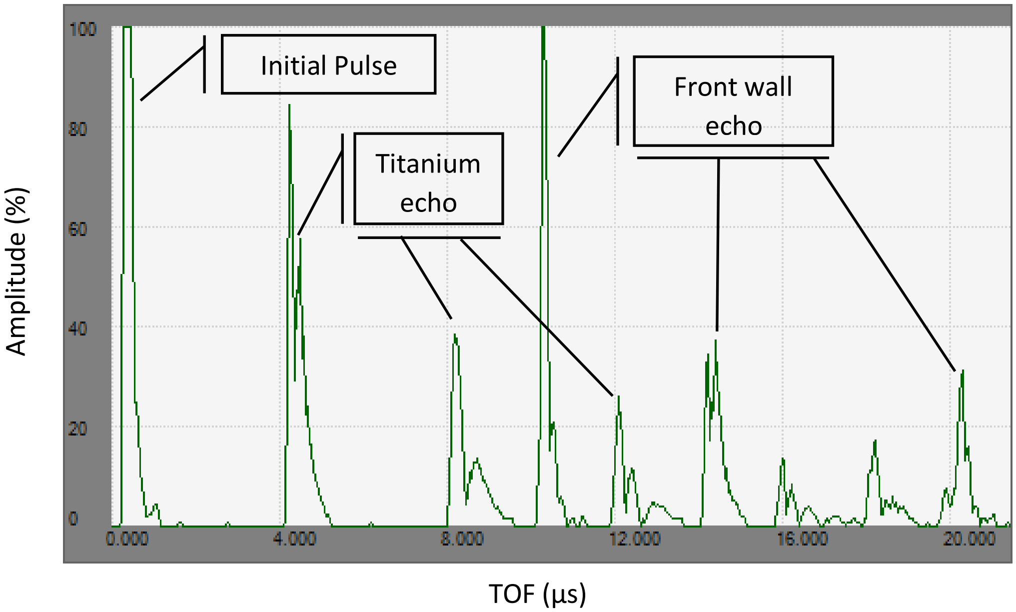

Figure 45. A-Scan of IWSLJ at Point A, showing the titanium and front wall echoes.

To correctly use the delay line, the calibration procedure outlined in the EPOCH© manual for the use of delay line was followed. It states that [39]:

1. The initial excitation pulse should be moved to the left until it is not visible on the CR screen, hence why it is not showing on the A-Scans presented in this chapter;
2. The operator should verify that the first echo now appearing on the screen is indeed the reflection of the delay line by tapping a finger on it and observing a signal damping effect; and
3. This echo should be moved left on the CR screen until it is barely visible by increasing the zero-offset value.

From the data presented in this section, it is obvious that the addition of a delay line can serve as a mitigating factor when inspecting in the near field. However, it also introduces new reflections, the front wall echoes, that can complicate the interpretation of A-Scans.

## 6.2. Sound Attenuation and Internal Reflections

It was mentioned in Section 4.3 that CFRP is highly attenuating. It was also explained how the IML of the IWSLJ cannot be directly accessed for inspection. This section explores the attenuating behaviour of CFRP and titanium, and looks as well at the internal reflections occurring inside the IWSLJ. When combining attenuation and reflection, a clear understanding of why the IML is difficult to inspect is achieved.

Being able to clearly identify each reflection and minimizing background noise is especially important when working with highly attenuating materials, such as CFRP. Figure 46 presents the A-Scan for Step 1 and 2, both taken at 10 MHz with a delay line. The only difference between Steps 1 and 2 is one of thickness: in the case of Step 2, the CFRP is 0.5 mm thicker on both sides, and concurrently titanium is 1 mm thinner. Both steps have the same numbers of reflecting interfaces. Therefore, the number of internal reflections can be assumed to be the same.

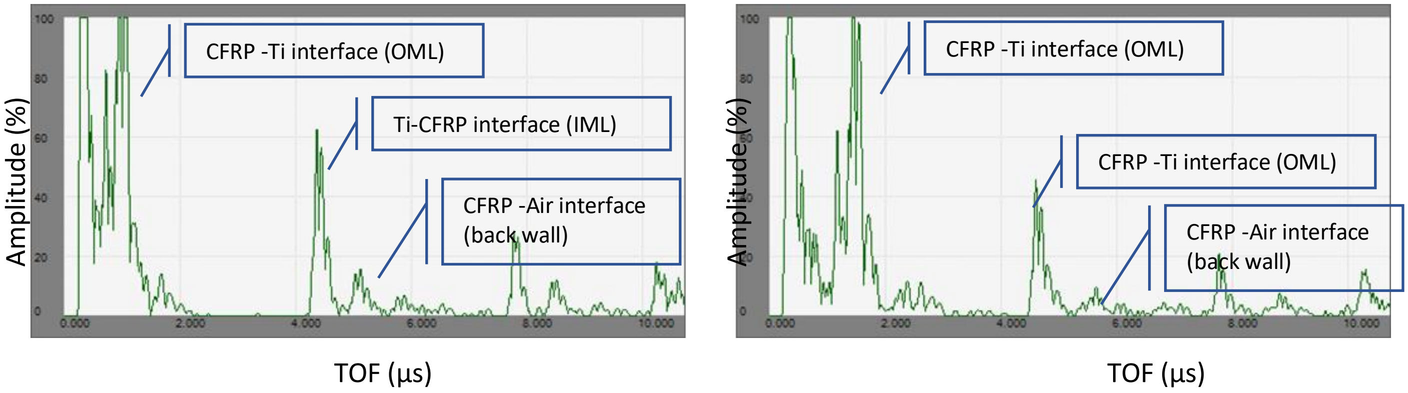

Figure 46. A-Scan of (a) Step 1 (b) Step 2, taken at 10 MHz with a delay line.

Both A-Scans show peaks at almost exactly the same time on the X-axis, as the difference in their respective thicknesses is not significative enough to be noticeable on the CR screen. According to Table 5, it takes 0.76 µs for the sound to reach the OML over Step 2, compared to 0.38 µs over Step 1. In both cases, it takes about 4 µs for sound to travel from the OML to the IML. The key difference between the two figures is the difference in intensity for each peak. In both steps, the titanium is approximately of the same thickness. But an increase in CFRP thickness by 0.5 mm is enough to lower the titanium reflection of Step 2 from 60% to 50%. Each peak for Step 2 has a lower intensity than the reflections of Step 1, thus demonstrating the attenuating nature of CFRP. It should also be noted that A-Scans at both points for Steps 1 and 2 were taken several times, to take into account the near-field effect described in the previous Section.

Section 4.3 explained the importance of the attenuation coefficient, and how it is made of multiple components: geometrical spreading of the transducer field $\alpha_G$, absorption $\alpha_A$, and scattering at the grain boundaries $\alpha_S$ so that $\alpha = \alpha_G + \alpha_A + \alpha_S$ [44]. The α coefficient for titanium was theoretically calculated based on pressures obtained with the Rayleigh Sommerfeld method, and experimental data from R. Li et al. [45] presented α coefficients of composites at different frequencies. In order to confirm the theoretical value obtained for titanium on Section 4.3 and to get a coefficient specific to CFRP, both attenuation coefficients were experimentally measured.

A CFRP panel with a thickness of 1.2 mm (48 thou) was used, as well as a titanium sheet 3.1 mm (1/8”) thick. Five A-Scans were taken per frequency (2.25, 5 and 10 MHz) on each panel. All scans were taken without a delay line, in order to measure the attenuating behaviour of only CFRP and titanium. The delay line introduces an additional layer of material, which would have inevitably contributed to the attenuation: sound would have to travel through it twice, but it would also introduce a new set of internal reflections, as explained in Section 6.1.

The exact process by which data points were acquired is described in Appendix 3. Once data points were acquired in % amplitude and distance z in cm, they were imported in MATLAB. The curve fitting tool was then used to generate the graphs seen in Figure 47. The best fit curve was automatically plotted in Excel using nonlinear least squares fitting. Robust fitting could have been used to minimize the impact of outliers, but considering that these outliers are the result of pressure fluctuations naturally occurring in the material, it was decided not to minimize their impact on the fitted curve.

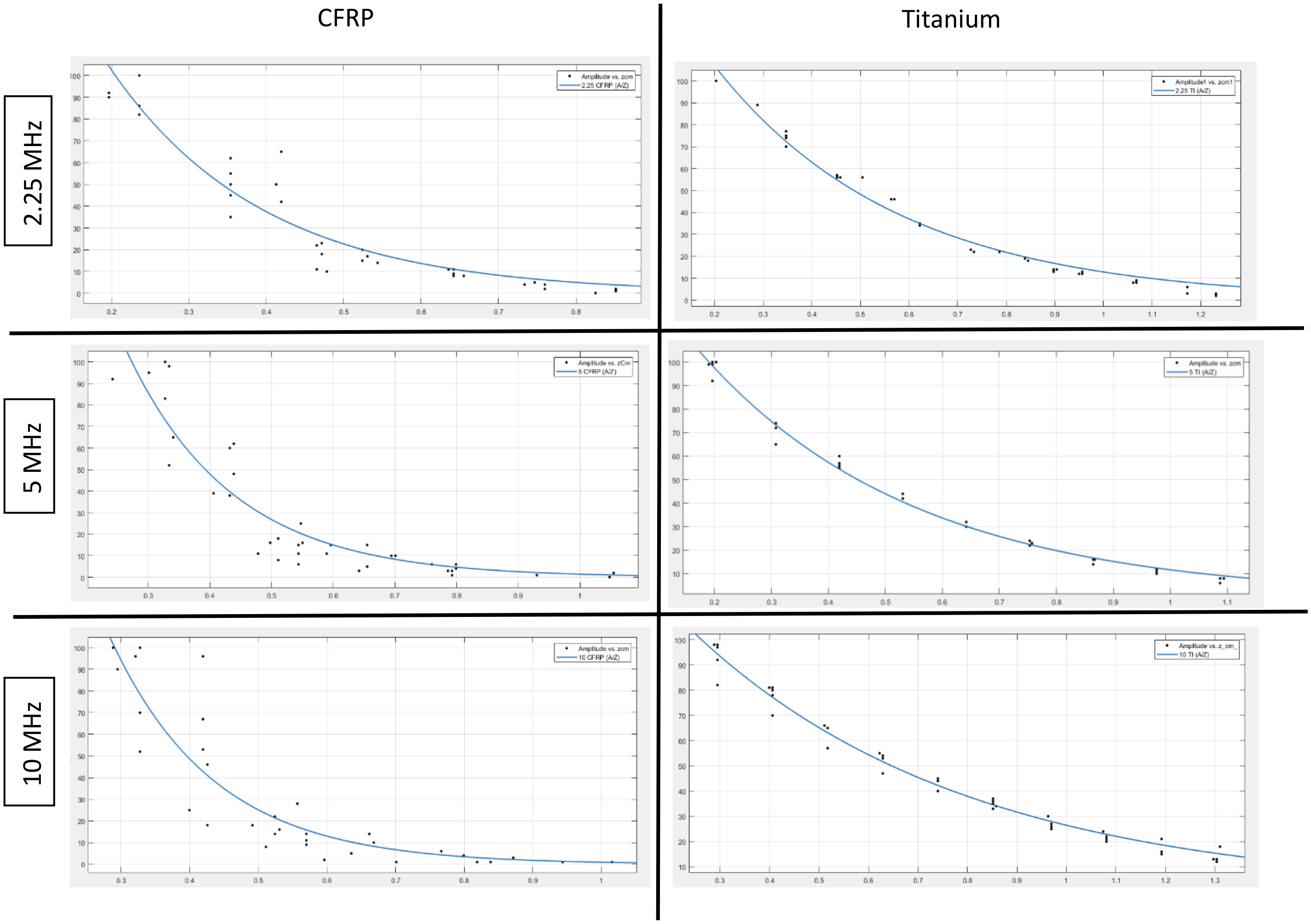

Figure 47. Fitted curves of CFRP and Titanium at varying frequencies, with the x axis being z in cm and the y axis being % amplitude.

The samples used to obtain the scans were fairly thin. The CFRP panel used had a thickness of 1.2 mm and the titanium panel was 3.1 mm thick. This was done intentionally, in order to have multiple peaks for each frequency. However, because no delay lines were used, the A-Scans were subject to pressure fluctuations. This is especially visible in Figure 47 for CFRP. Titanium was still affected, but clearly not as much. The data points for all titanium scans on Figure 47 indicate where each reflection is located, and only the effect of pressure fluctuation is visible, as data points are move up and down a little relative to their general trend. In the case of CFRP, not only are the pressure amplitudes greatly varying in each scan, but no distinct reflections are visible, except for 2.25 MHz. This can be explained by the anisotropic nature of CFRP, impacting the speed at which sound travels through the material.

Table 7 shows the $R^2$ values obtained for each curve, as well as the attenuation coefficient α in dB/cm. The signal amplitude on an A-Scan corresponds to the signal's intensity. Therefore, the coefficient experimentally measured is $\alpha_I$. From Section 4.3, it is known that $\alpha_I = 2\ \alpha$. Knowing that 1 Np is 8.69 dB [74], the experimentally measured $\alpha_I$ were converted to α. Note that no similar data was found in the literature, except for the study by R. Li et al. [45] presented in Section 4.3. Their study [45] did not discuss the uncertainty of their results and therefore, comparing the confidence bounds of Table 7 to data collected by others was not possible.

Table 7. Experimentally obtained attenuation coefficients for CFRP and Titanium at varying frequencies

| Material | Frequency | $\alpha_I$ (Np/cm) with 95% confidence bounds | $R^2$ | α in dB/cm |
|---|---|---|---|---|
| CFRP | 2.25 MHz | 5.0 (±0.7) | 0.91 | 21.9 |
|  | 5 MHz | 5.8 (±1.1) | 0.85 | 25.2 |
|  | 10 MHz | 6.6 (±1.8) | 0.81 | 28.7 |
| Titanium | 2.25 MHz | 2.7 (±0.1) | 0.99 | 11.5 |
|  | 5 MHz | 2.7 (±0.1) | 0.99 | 11.6 |
|  | 10 MHz | 1.8 (±0.1) | 0.98 | 7.8 |

From Figure 47 and Table 7, the impact of frequency on ultrasound transmission can be clearly observed. For CFRP, the attenuation coefficients increase with frequency. This can be explained by the changes in wavelength that occurs with each frequency. In the case of CFRP, a short wavelength (higher frequencies) means that more sound is scattered as it travels through the material (see Section 4.3).

On the other hand, a different phenomenon is observed for titanium. Titanium demonstrates approximately half the attenuation of CFRP, since sound in metals is less scattered than in composites. At 2.25 and 5 MHz there is no measurable difference in attenuation. At the Highest frequency (10 MHz), ultrasounds appear less attenuated, potentially because beam spreading is smaller at higher frequencies (see equation 4.18). Because CFRP and titanium behave in such a different way, and because the thicknesses of both materials keep changing in the lap joint, choosing the optimal inspection frequency can be challenging.

The theoretical attenuation coefficient obtained for titanium at 5 MHz, in Section 4.3, was based entirely on calculated pressure values and was equal to 3.9 dB/cm. The experimental value obtained is equal to 11.5 dB/cm. This is because the calculated value did not take into consideration important factors, such beam spread. The Rayleigh Sommerfeld method was used to calculate the sound pressure in the centre of the transducer only. For CFRP, the values experimentally obtained are similar to those obtained by R. Li et al. [45] shown in Figure 15. Their study took into consideration all components of the attenuation coefficient. The plotted values in Figure 15 at 5 and 10 MHz are about 20 dB, and therefore, are in good agreement with the experimental data shown in Table 7.

However, when trying to understand the attenuating behaviour of a multilayered structure such as the IWSLJ, understanding how sound behaves as it crosses different interfaces is critical.

From Section 4.3 and equation 4.11, it is understood that the impedance difference between two layers causes part of the initial wave to be transmitted into the next medium, while part of it is reflected. Table 4 shows how much sound reaches each layer of the IWSLJ **if no internal reflection is assumed**. The reality of it is that each reflected wave will travel to a new surface, while being attenuated before it hits that new surface, where once again part of it will be transmitted, and part of it will be reflected. The same thing can be said about each transmitted wave. It is therefore, complicated to calculate exactly how attenuating a multilayered structure is, but possible. Figure 48 shows a cross-sectional view of the IWSLJ, with the different surfaces S causing internal reflections (S4 is the back wall).

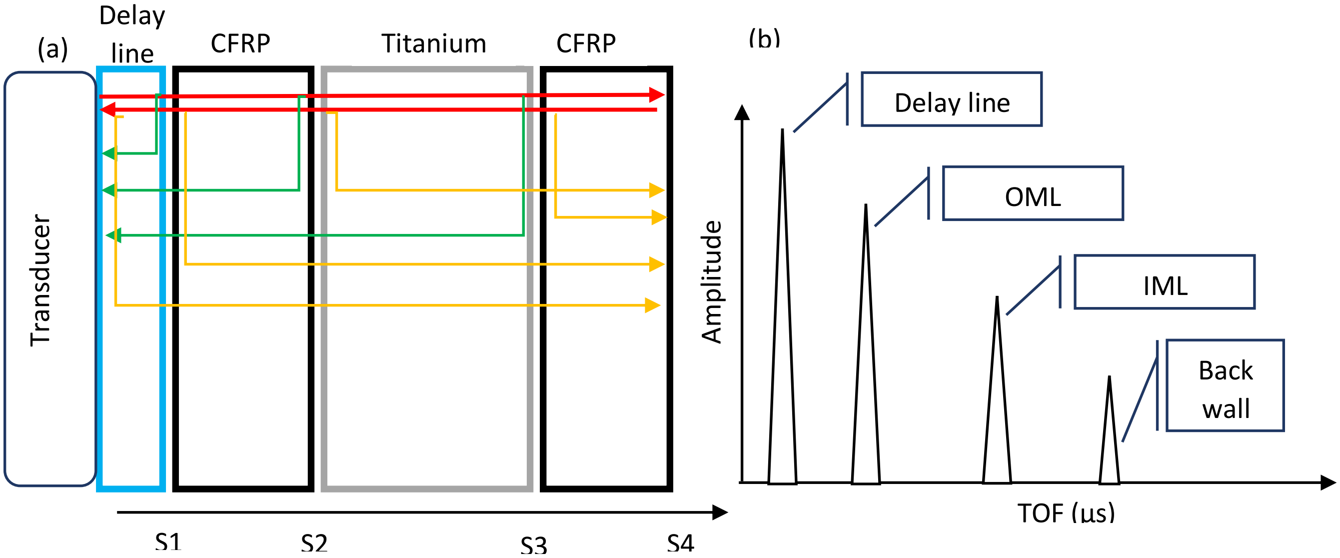

Figure 48. (a) Representation of internal reflections in the IWSLJ (b) A-Scan sketch showing how each internal reflection generates an echo.

If equation 4.11 is applied to Figure 48 the same way it was to populate Table 4, then it can be said that when the signal, first travelling through the delay line, hits the CFRP, 93% of the sound enters CFRP, and 7% is reflected. Of the 92% in CFRP, 45% will be transmitted to the titanium, while 55% bounces back inside the CFRP. Finally, of the 45% which entered the titanium, 30% reaches the last layer of gel and hits the receiver. The emission of the main pulse is shown in Figure 48 by the red arrow. Reflections occurring at interfaces, while the main pulse travels to S4, are shown by green arrows. Each green arrow will reach the transducer before the red arrow can reach S4 and travels back towards the transducer. Therefore, the first green arrow, representing signal reflected at the delay line – CFRP interface (S1) will cause the delay line echo on an A-Scan, as shown in Figure 48(b). Each subsequent green arrow will create the echo of the surface at which it got reflected. However, every reflection represented by the green arrows also has to cross different interfaces before hitting the transducer. In the same way that the main pulse (red arrow) reflects part of the sound at each interface (green arrows), the green arrows traveling towards the transducer will be in part reflected, thus generating the yellow arrows. Those beams will also be partly reflected and transmitted at each interface. This will go on inside the material until no more pulses are sent through the lap joint, and each internal reflection has completely attenuated.

When combining the internal reflections described above with the attenuating behaviour of CFRP, it becomes obvious that detecting disbonds on the IML will always be more difficult than detecting disbonds on the OML, because the signal has to travel greater distances and cross more interfaces.

## 6.3. Signal-to-Noise Ratio and Frequency Selection

Section 6.2 explained that the signal coming form the IML will always be more attenuated and of smaller amplitude than the signal coming from the OML. In this section, possible factors, such as signal-to-noise ratio and frequency, are investigated in the hopes of making IML reflections more visible.

The signal-to-noise ratio, which measures how a signal compares to background noise. The absolute peak amplitude and the absolute noise level depend on a variety of factors, such as:

- probe diameter, frequency, and efficiency;
- flaw location with respect to the incident beam, as well as the distance of the sound path; and
- flaw characteristic and sound scattering properties.

Signal-to-noise ratio can be mathematically calculated, using the equation is [75]:

$$\frac{S}{N} = \sqrt{\frac{16}{\rho c w_x w_y \Delta t} \frac{A_{flow}(f_0)}{FOM(f_0)}} \tag{5.1}$$

Where ρ and c are the material's density and speed of sound, $w_x$ and $w_y$ are the lateral beam width and the flaw depth, $\Delta t$ is the duration of the pulse, $A_{flow}(f_0)$ is the scattering amplitude at centre frequency and $FOM(f_0)$ is the noise Figure of Merit at centre frequency [75].

By examining equation 5.1, key relationships can be established. First, the signal-to-noise ratio increases as the scattering amplitude increases (larger flaws increase detectability). All the other factors introduced in equation 5.1 are inversely proportional to the signal-to-noise ratio, that is beam width, material's density and speed of sound, and the duration of the pulse. Focused beam, low-density material with small speed of sound and shorter pulses (often associated with higher frequencies) all increase detectability [75].

Table 6, introduced in Section 6.1, shows how probe frequency can affect the near field length. The current procedure [5] calls for a 10 MHz transducer, but this frequency is also the one yielding the longest near field. To compare the impact of frequency on the clarity of the signal, the IWSLJ calibration block, described in detail in Section 5.1.1, was inspected with 2.25, 5 and 10 MHz transducers. Scans of Steps 1, 3, and 9 are shown in Figure 49. Lower frequency probes are usually not recommended for near surface disbond detection, due to their longer wavelength. This explains why the 2.25 MHz probe is only improving the image quality starting at Step 9. Before that, the multiple back wall echoes are not clearly visible. Similarly, the main reason why a 10 MHz probe is used for the inspection of Steps 1 and 2 is not directly related to signal-to-noise ratio. Rather, due to the small thicknesses of the CFRP, a higher frequency offers a better resolution of surface flaws and is therefore, more appropriate to distinguish disbonds on the OML.

Still, the impact of signal-to-noise ratio is visible in Figure 49, shown in the dotted circles, as the amount of background noise seen for Step 1 on the 10 MHz scan is slightly higher than on the 5 MHz scan, whereas almost no background noise is visible at 2.25 MHz, but the reflected signals are also less visible. This can be explained by equation 5.1. Smaller frequencies mean longer wavelength and a longer pulse width ($\Delta t$). Starting at about Step 3, a 5 MHz transducer has greater advantage because the background noise reduction makes each peak more visible.

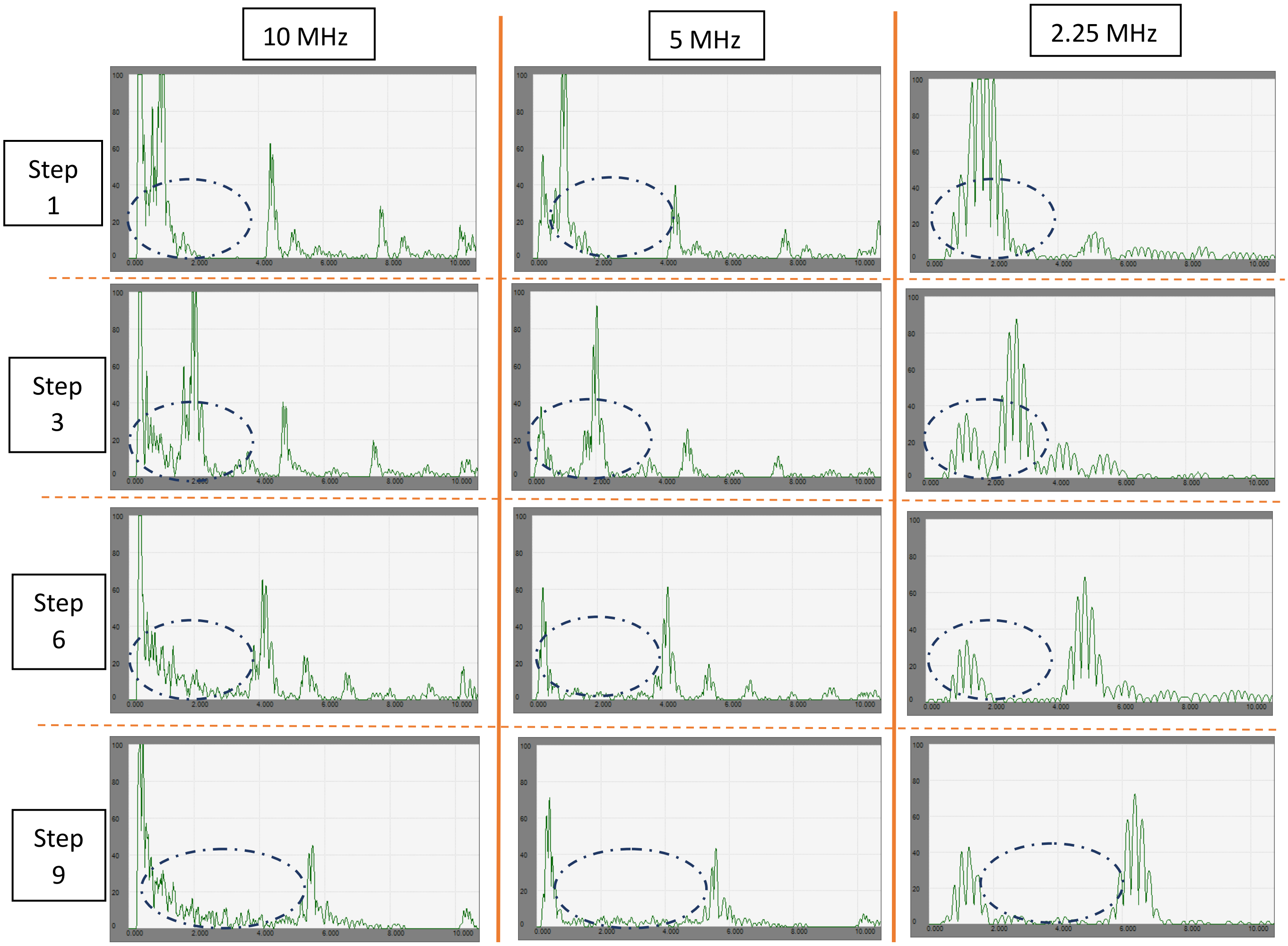

Figure 49. A-Scans of Steps 1, 3,6 and 9 with a 10 MHz, 5 MHz and 2.25 MHz transducer showing the impact of frequency on background noise with the % amplitude as the Y-axis and TOF as the X-axis.

The current procedure requires a 10 MHz probe for the inspection of Steps 1 and 2 and a 2.25 MHz transducer for the inspection of the outboard edge of the titanium plate. This section showed that those frequencies are indeed optimal for the inspection of those areas.

## 6.4. ASTM D1002— Apparent Shear Strength of Single-Lap-Joint Adhesively Bonded Metal Specimens by Tension Loading

The ASTM D1002 standard [7] is a widely accepted quality assurance test for bonding processes that tests the strength of an adhesive bond [22]. It tests the strength of a single lap joint specimen under tension. Comparing results of good bonds to those of kissing bonds will give an indication of the impact of kissing bonds on bond strength. It should be noted that this standard cannot be used to predict the service life of a bond. As discussed in Section 2.5.1, many factors can lead a bond to appear strong a first, but it can weaken quickly when exposed to different elements, such as moisture. However, for the purpose of this project, the ASTM D1002 [7] standard is useful, as the intent of this section is to quantify the impact disbonds may have on the strength of a bond.

All titanium sheets were properly grit blasted prior to adhesion. The two samples with mold release failed at that step and could not be used for the tension test. Therefore, the load at failure is identified as 0 N and not included in the following results. The remaining eight samples were pulled in tension at a rate of 1 mm/min until failure. Table 8 presents the results obtained from the tests. Once the samples failed, the overlap area was measured using a caliper, so that the force applied at failure could be converted into units of pressure.

Table 8. Results of Tension Tests

| **Sample** | **Force at failure (N) ±0.1%** | **Area ($mm^2$) ±0.5%** | **Shear Stress (MPa) ±0.6%** |
|---|---|---|---|
| **Tape 1** | 418 | 337 | 1.2 |
| **Tape 2** | 450 | 375 | 1.2 |
| **Average** | 434 | 356 | 1.2 |
| **Control 1** | 9600 | 350 | 27.4 |
| **Control 2** | 9700 | 356 | 27.3 |
| **Control 3** | 9700 | 345 | 28.1 |
| **Control 4** | 11500 | 360 | 31.9 |
| **Control 5** | 11400 | 372 | 30.7 |
| **Control 6** | 11500 | 410 | 28.1 |
| **Average** | 10567 | 366 | 28.9 |

The control samples were numbered from one to six as they were cut from the main sample, but it should be noted that they were not tested in that order. Sample 6 was the first one tested, followed by #5, #2, #3, #4 and finally #1. On average, the two samples with tape disbonds failed at 434 N, which corresponds to a shear stress of 1.22 MPa. The six control samples separated into two different groups. Coupons 4, 5 and 6 failed at around 11500 N, while coupons 1, 2 and 3 failed at about 9700 N. Because the coupons were not tested in numerical order, an equipment malfunction during testing can be ruled out as a probable cause. In theory, all the overlaps were supposed to be dimensioned 322.58 $mm^2$ (1/2” x1”), but the strips were cut manually with a band saw. This probably accounts for the irregular overlap areas. Additionally, the adhesive was cut slightly too short. When it was applied to the coupon, it was lightly pulled on from the sides, so that it would cover then entire overlap area. Maybe this was done unevenly, possibly enough to cause the two different groups observed. Between control samples 1 and 6, there is as much as 60 mm$^2$ difference in overlap area. But, between control samples 2 and 4, there is only a difference of 4 mm$^2$, and yet control sample 2 failed at 9700 N and control sample 4 at 11500. Because the samples were not tested in numerical order, the difference could not possibly be attributed to the execution of the tension test. Another possible explanation for the results obtained could reside in the adhesive mode of failure (see Section 2.5.1).

The two samples with tape disbonds suffered adhesion failures, which was expected. The typical clean break, as explained in Section 2.5.1, is visible in Figure 50, where all the adhesive stayed on one side of the sample. Both samples failed in the same way, but had a small difference in their overlap surface.

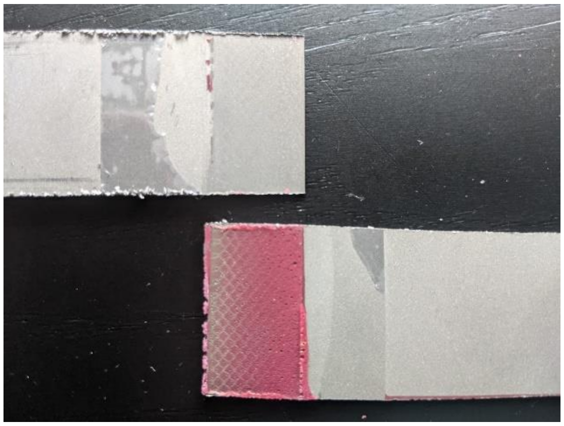

Figure 50. Tape disbond sample 2 after failure.

All six control samples failed with mixed-mode failure of cohesion and adhesion. Figure 51 shows control Sample1, where the adhesion failure appears in a triangular shape, while the rest of the adhesive failed cohesively.

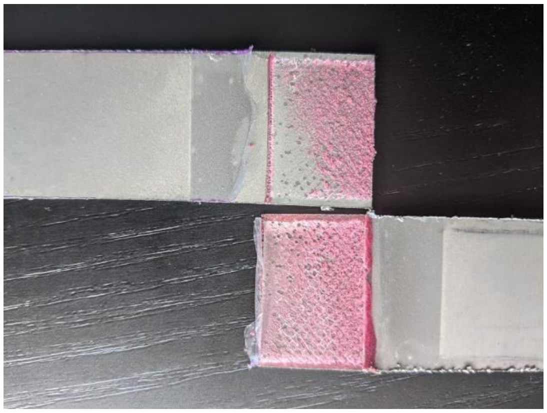

Figure 51. Mixed failure modes of control Sample 1.

It is interesting to note that all six samples presented adhesion failure in a similar triangular shape, all on the same side. Figure 52 shows all six samples, in the same order they were cut, and highlights the triangle shape, which was outlined in black.

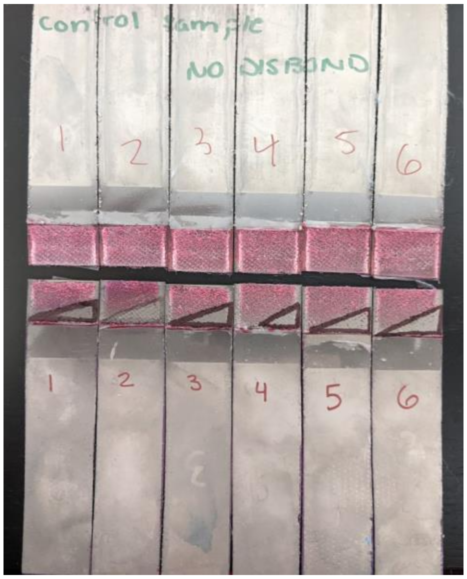

Figure 52. Mixed failure modes on all control samples.

As previously mentioned in Section 2.5.1, when performing lap shear tests such as the ASTMD1002 [7], full cohesion failure was expected over all six samples. A mixed mode of failure can usually be explained by partial degradation of the interface. In this case, the adhesive was not cured at the right temperature. It is also possible that the motion of the band saw, combined with the vibrations it induced, tore the adhesive from the adherent. This is similar to the triangles obtained when trying to pull a label from a plastic bottle, for example. When flaps detach from the adherent, by tearing or peeling, they narrow and collapse in pointy shapes [76]. This phenomenon has been observed for thin film adhesives, as well as when peeling fruits such as oranges and tomatoes [76]. Hamm et al. [76] explain how this can be linked to the conversion of bending energy into surface energy of fracture and adhesion.

Since all adhesion failure occurred on the same titanium sheet, it is possible that surface preparation was not adequate, or perhaps the surface became contaminated after grit blasting. It is also possible that the adhesive was slightly stretched when being applied, thus explaining why Samples 1, 2 and 3 broke sooner than Samples 4, 5 and 6. If the adhesive was stretched, it did not have an even thickness all across. But based on the studies of Hamm et al. [76], it is more likely that the band saw tore the adhesive on the edge, creating a stress concentrator as described in their paper. When that small section of adhesive detached, it did so before the rest of the adhesive and got pulled away faster, creating the observed triangle shape.

Table 9 compares the areas of adhesion failure with the areas of cohesive failure. The area of adhesion failure was estimated by approximating the area in the shape of a rectangle triangle, as seen in Figure 52. The same overlap areas introduced in Table 8 are also shown, but the area of the "triangles" left by adhesion failure is added to Table 9, as well as the percentage of how much of the overlap failed by adhesion.

Table 9. Adhesion failure area

| **Sample** | **Total Area ($mm^2$) ±0.5%** | **Triangle Area ($mm^2$) ±0.1%** | **% of adhesion failure ±0.6%** | **Force at failure (N) ±0.1%** |
|---|---|---|---|---|
| **Control 1** | 350 | 100 | 28.6 | 9600 |
| **Control 2** | 356 | 108 | 30.3 | 9700 |
| **Control 3** | 345 | 92 | 26.7 | 9700 |
| **Control 4** | 360 | 68 | 18.8 | 11500 |
| **Control 5** | 372 | 84 | 22.6 | 11400 |
| **Control 6** | 410 | 90 | 21.2 | 11500 |
| **Average** | 365.50 | 90.33 | 24.7 | 10567 |

It can be observed that Samples 4, 5 and 6, which required the most force at failure, also present the smallest area of adhesion failure, possibly explaining the difference observed in Table 8. The transition mechanism of an adhesive bond from strong bond, which fails by cohesion failure, to a weak bond, which exhibits adhesion failure, is not well understood [25].

Putting all these factors together explains why the average strength of the bond obtained experimentally in this paper is 11 MPa weaker than the value listed in the adhesive datasheet [77], which is 39.99 MPa. Still, it is obvious that total adhesion failure (i.e. disbonds) have a detrimental impact on the overall bond strength. Even in this specific case, where something led the control samples to be weaker than expected, the disbonded samples were only 4% as strong.

Bond strength has been tested with the ASTMD1002 standard [7] many times, using many types of material. Qiu et al. [24] experimented on CFRP panels, with disbonds varying in size and thus occupying a different percentage of the bond line. Without much surprise, they found that the strength of adhesive joints decreases with the increase of defective area. A summary of their findings, for linear disbonds transverse to the bond line, can be found in Figure 53, where the average load at failure is plotted against the defective area [24].

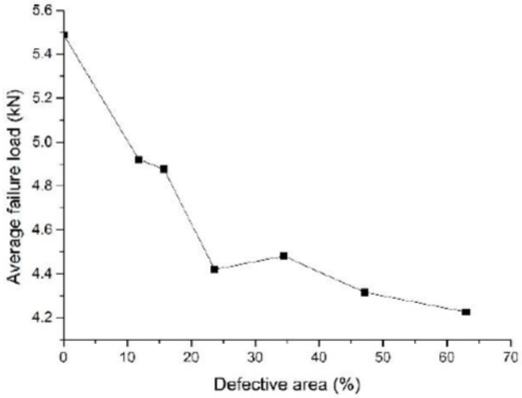

Figure 53. Average failure load vs. defective area in %, for CFRP [24].

Heidarpour et al. [20] did a similar study, but focused on the impact of 2D vs. 3D defects in the bond line. All disbonds introduced so far in this paper have been examples of 2D defects, with the exception of the holes cut in the adhesive of Sample No. 2. A 3D defect is volumetric in nature. In their study, Heidarpour et al. [20] used PVC foam to create the 3D disbonds, inserted between sheets of 2024-T3 aluminum. Their results are shown in Figure 54 below.

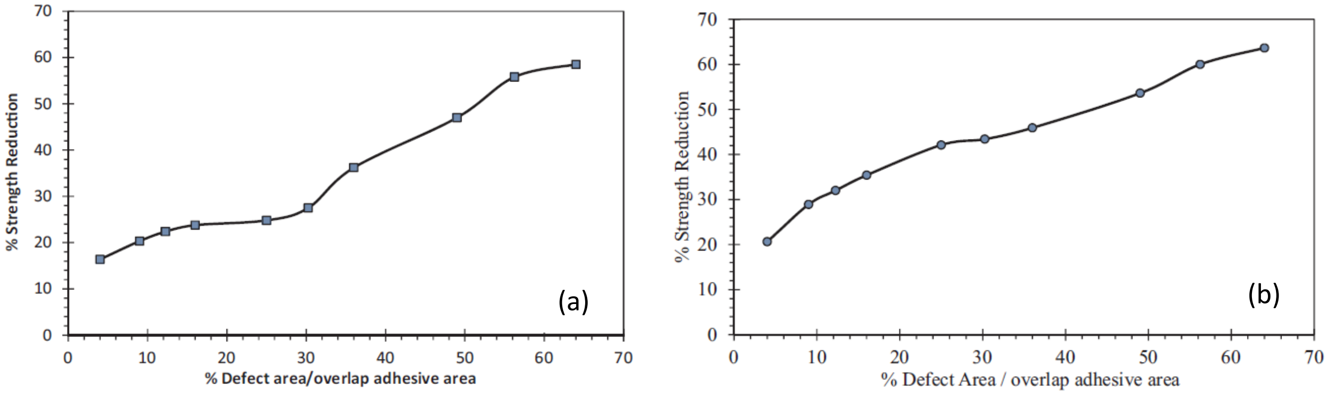

Figure 54. Effects of (a) 2D and (b) 3D defects on bond strength [20].

It is interesting to note that in the case of the 3D defects, although the impact of defect size on the rate of strength reduction is higher, the rate is almost linear. In the case of 2D defects, both Qiu et al. [24] and

Heidarpour et al. [20] came to a similar conclusion: the bigger the disbond the weaker the bond. This conclusion can also be drawn by comparing Figure 53 and Figure 54. The numbers experimentally obtained in this section may seem high, but a 96% strength reduction with 100% of the bond line covered by area kissing bond appears to be in agreement with the experimental results obtained by other researchers.

In this section, kissing bonds have been shown to drastically impact the strength of bond, even if only a small region of the bond line is affected. There may not be data available on kissing bond or disbond growth rate yet, but these results suggest that detecting defects as early as possible should be a major inspection focus.

## 6.5. Detectability of Kissing Bond

Disbonds, like many other material defects, can grow under stress. Before they form a full "air pocket" that is clearly identifiable on an A-Scan and yields results similar to FBH, they will present as a kissing bond (see Section 2.2), where partial sound transmission through the defect is still possible. Kissing bonds have been shown to have a critical impact on bond strength (see Section 6.4). Therefore, the intent behind the manufacture of Sample No. 1 was to determine if kissing bonds could be detected with conventional UT. Additionally, if kissing bonds can be created in a laboratory environment, this opens the door to the creation of more realistic and challenging training aids, currently not available in the industry.

Because the CFRP thickness of Sample No.1 is similar to that of Step 3 and because it was shown in Section 6.3 that a 5 MHz transducer starts to exhibit significantly reduced background noise at a CFRP thickness of about 2 mm, all A-Scans of Sample No.1 were performed with a 5 MHz transducer, with the 11.43 mm delay line introduced in Section 6.1. The initial intent was to use the hole in the centre of the plate to perform calibration on the CFRP and obtain sound velocity for this specific panel, since the exact carbon fibre type available in the lab was not the same AS4 carbon fibre used on the F-A/18. According to the EPOCH 600© user manual, single thickness calibration is possible, and the step-by-step instructions were followed [39]. However, as per the disclaimer in the manual, it is possible for the calibration to fail if the thickness is too thin. The CFRP panel on Sample No. 1 is 2.1 mm thick, and the attempt at a single thickness calibration failed, possibly because the sound path in the CFRP panel was too short to enable calibration. This experiment failed at calculating the speed of sound in carbon fibre — epoxy with 0/90 layout. Nonetheless, all calibration steps stated in [5] were completed, adjusting only the gain to 50 dB. Although the speed of sound in the exact carbon fibre-epoxy mix was not accurately determined, all TOF calculations performed with the speed of sound in the AS4 CFRP match the A-Scans shown in this Section. Therefore, it can be assumed that the two CFRP have very similar properties.

First, defect 1.5 in Figure 38 was analyzed. It represents a good bond and is considered the reference point of Sample No. 1, since no inserts were placed there and both surfaces were adequatly prepared for bonding.  Therefore, all further A-Scans are compared to this figure. The A-Scan of the FBH is also used as a reference, to see if the inserts created kissing bonds, or complete disbonds. If complete disbonds are created, then the A-Scans will be similar to that of the FBH. Figure 55 shows the scan of both the good bond area and the FBH. The difference between the two scans is obvious, as the titatnium reflection is not visible in Figure 55(b), and all additional reflections also dissapeared. The only other peak visible on Figure 55(b), other than the CFRP echo, is the delay line echo (front wall echo) at 10 µs.

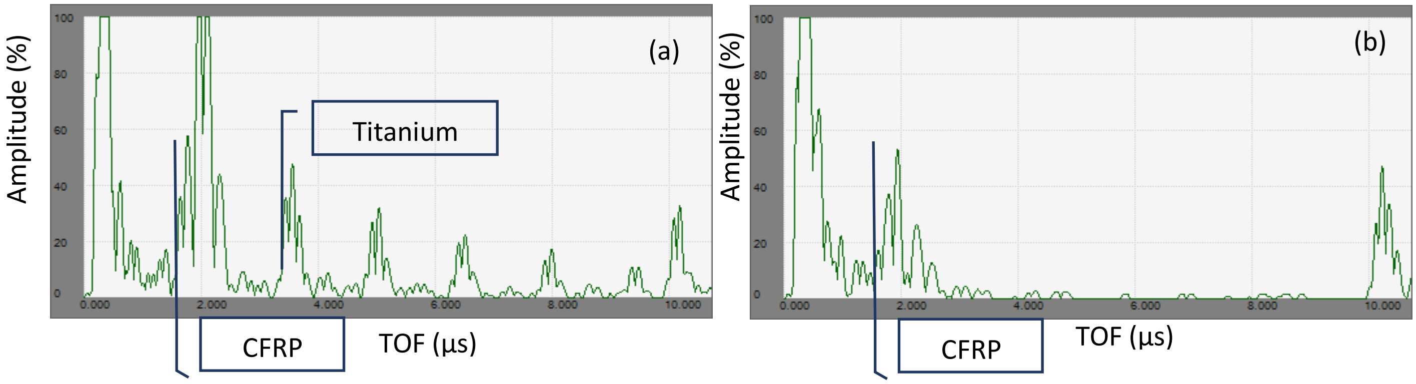

Figure 55. A-Scan of (a) defect 1.5 - good bond and (b) FBH 1.

The approximate amplitudes of the second to the fifth peak of a good bond are shown in Table 10. The reason why the first peak, being the CFRP reflection, is excluded, is because the tip of the peak is not visible. All amplitudes are considered approximate for two reasons; the first one being pressure fluctuations, and the second being the large scale of the Y-Axis on the A-Scans. Because the Y-axis is labeled every 20%, and because readings were taken manually, an uncertainty of ±5% is estimated on the amplitudes. It should be noted that the scale of the Y-axis could not be altered with the software used to extract the A-Scans.

Table 10. Measured peak amplitudes of the reference point of Sample No. 1.

| Peak # | Amplitude ref (±5 %) |
|---|---|
| 2 | 50 |
| 3 | 30 |
| 4 | 22 |
| 5 | 18 |

Next, defects 1.1 and 1.6, both created with mold release are compared. Note that in each case, one of the adherents, CFRP or titanium, was sanded/grit-blasted, while the other was not (see Figure 38). The resulting A-Scans are presented in Figure 56, with the approximate amplitude shown in Table 11.

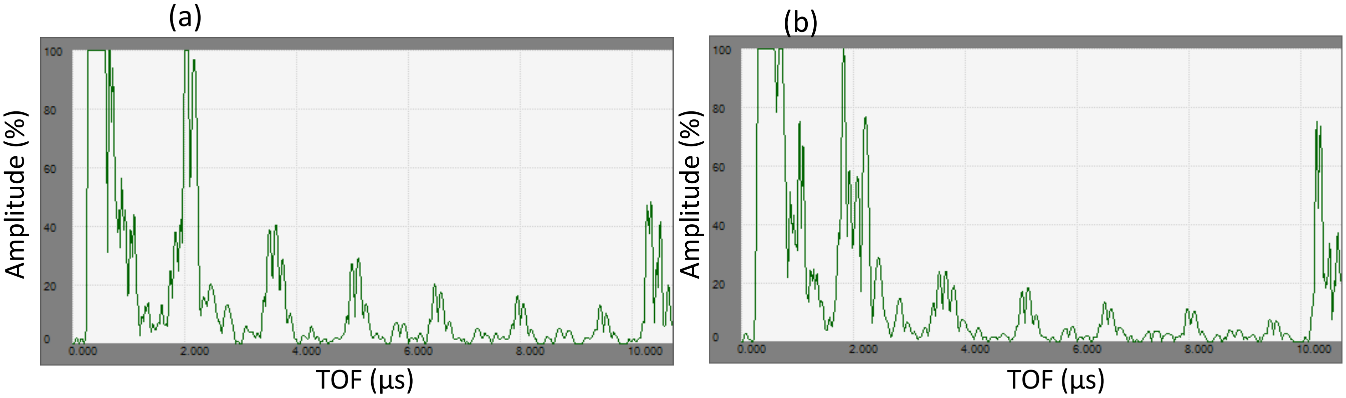

Figure 56. A-Scan of mold release (a) 1.1- CFRP not sanded, titanium grit blasted (b)1.6- CFRP sanded, titanium not grit blasted.

Table 11. Measured Amplitudes of the two mold release scans compared to reference amplitudes.

| Peak # | Amplitude (±5 %) (ref) defect 1.5 | Amplitude (±5 %) (a) Defect 1.1 | Amplitude (±5 %) (b) Defect 1.6 |
|---|---|---|---|
| 2 | 50 | 40 | 25 |
| 3 | 30 | 30 | 20 |
| 4 | 22 | 20 | 15 |
| 5 | 18 | 18 | 10 |

When comparing both scans of Figure 55(b) to Figure 56(b), it is clear that the mold release created an effective kissing bond, as multiple reflections are still visible, compared to a FBH. Yet, the amplitudes of each peak are lowered. It is interesting to note that the peak amplitudes of the mold release with CFRP sanded and titanium not grit blasted (Figure 56 (b)) is significantly lowered than the other mold release disbond (Figure 56 (a)), possibly due to increase sound scattering at the interface.

The third mold release defect, defect 1.4, was not included in Figure 56 and Table 11 to allow for an better comparison with defects 1.2 and 1.7, presented in Figure 57. Both sets of defects (1.1-1.6 and 1.2-1.7) were applied on surfaces treated the same way. Therefore, the two scans shown in Figure 56 and Figure 57 be compared.

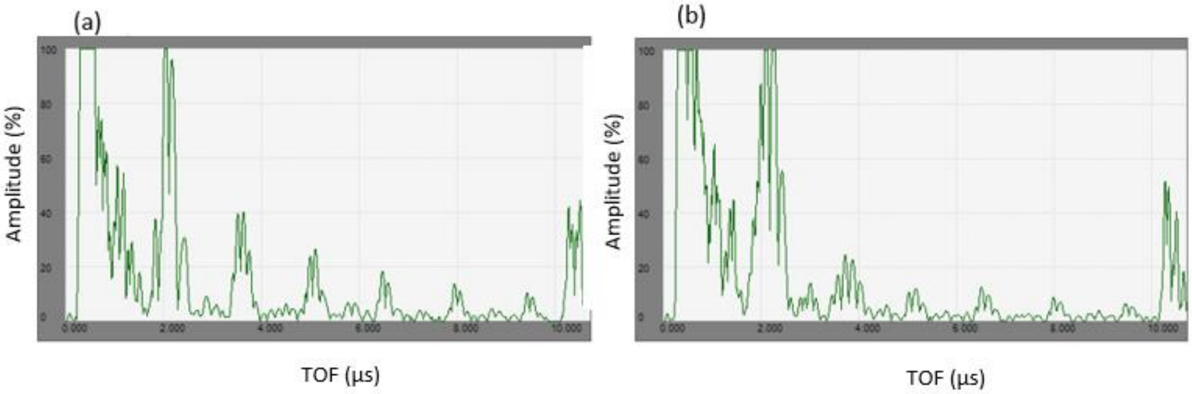

Figure 57. A-Scan of tape (a) 1.2-CFRP not sanded, titanium grit blasted (b) 1.7-CFRP sanded, titanium not grit blasted.

The peak amplitudes, shown in Table 12, varied in a similar manner to those of Figure 56. They are lower than the reference scan in both cases, but significantly lower when the titanium was not grit blasted.

Table 12.Measured Amplitudes of the two tape scans compared to reference amplitudes.

| Peak # | Amplitude (±5 %) (ref) Defect 1.5 | Amplitude (±5 %) (a) Defect 1.2 | Amplitude (±5 %) (b) Defect 1.7 |
|---|---|---|---|
| 2 | 50 | 40 | 22 |
| 3 | 30 | 25 | 10 |
| 4 | 22 | 15 | 12 |
| 5 | 18 | 10 | 8 |

from Table 11and Table 12, surface treatment appears to have an impact on sound transmission, as both areas where the titanium was not grit blasted yielded lower peak amplitudes compared to the areas where the CFRP was not sanded. In order to know what role the surface preparation prior to bonding has on sound transmission, scans of defects 1.3 and 1.8, where CFRP is sanded and the titanium not grit blasted, and vice versa, are shown in Figure 58. Note that no inserts have been placed in those regions. Only the impact of surface treatment is observed.

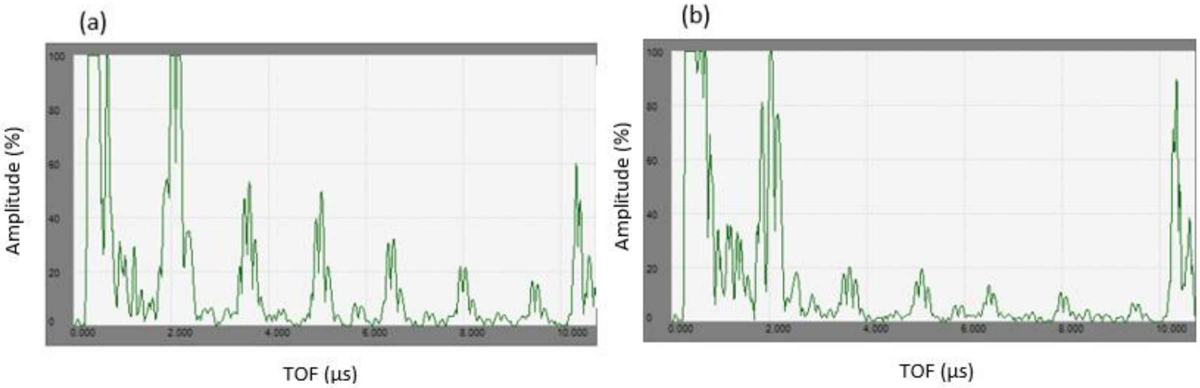

Figure 58. Impact of surface treatment on peak amplitude (a) 1.3- CFRP not sanded, titanium grit blasted (b)1.8- CFRP sanded, titanium not grit blasted.

The amplitudes are compared in Table 13 with the reference scan, where both surfaces were adequately treated. Once again, when the titanium was not grit blasted, the amplitudes are significantly lower, but when the CFRP was not sanded, the amplitudes are higher than the reference scan.

Table 13. Measured Amplitudes of Surface treatment scans compared to reference amplitudes.

| Peak # | Amplitude (±5 %) (ref) Defect 1.5 | Amplitude (±5 %) (a) Defect 1.3 | Amplitude (±5 %) (b Defect 1.8 |
|---|---|---|---|
| 2 | 50 | 55 | 20 |
| 3 | 30 | 50 | 20 |
| 4 | 22 | 30 | 15 |
| 5 | 18 | 20 | 10 |

Sanding or grit blasting is performed in order to increase surface roughness, so that the adhesive adheres better to the surface. However, the results indicate that the increased surface roughness of the CFRP scatters more sound than non-sanded CFRP. This would explain why the amplitudes of Figure 58 (a) are higher than the reference A-Scan, where both surfaces were treated. On the other hand, grit blasting the titanium appears to be critical to the creation of a good bond. Every scan taken where the titanium is not grit blasted show significantly lower amplitudes than the reference scan. The amplitudes of defect 1.8, where no insert was placed, are lowered  by approximately the same amount as the amplitudes of defect 1.6 and 1.7. This suggests that the adhesive could not properly adhere to the titanium, hence creating a small kissing bond. This is also consistent with the observations made by other researchers, [19] [23] [25], which is that when adhering composite to metal, the surface preparation of the metal is the most critical.

Knowing that not sanding the CFRP increases the peak amplitude observed, it can then be concluded that both inserts created kissing bond. Indeed, when comparing Figure 55(a) to Figure 56(a) and Figure 57(a), there is not a major difference in peak amplitudes. But knowing that the CFRP was sanded in Figure 55(a), but not in Figure 56(a) and Figure 57(a), the amplitudes of Figure 56(a) and Figure 57(a) are expected to be higher than those of Figure 55(a), yet they are lowered. This shows that both inserts created kissing bonds. Signals of defects 1.1, 1.2, 1.6 and 1.7 are lower than the reference, thus demonstrating that sound transmission was impacted.

Because both inserts have produced similar amplitudes, through transmission testing was used in order to determine which insert blocked more sound. In the case of a real disbond, no sound would make it to the receiving probe, as all sound would be reflected by the “air pocket” created by the disbond. Although not realistic for real life testing of the IWSLJ, this method of testing is a good option to determine how efficient the inserts are at blocking sound.

In Figure 59, the Y-axis represents the relative amount of energy that makes it through the sample, while the X-axis represents the time it took for each pulse to reach the receiver. Figure 59(c) represents a through transmission scan of an area without disbond, and is therefore, used as a point of reference. The first peak, appearing at 0.9 μs, has an amplitude of 100%. This indicates that signal loss due to attenuation and internal reflections is minimal in Sample No. 1, due to its small thickness. When looking at the first peaks on Figure 59(a)&(b), it can be observed that the amplitudes are respectively 80% and 93%, meaning that mold release blocked 13% more sound than the thermal tape. The results of tension tests performed on other coupons, presented in Section 6.4, corroborate these results as well; the coupons bonded with mold release failed at a much lower strength than the tape disbonds, indicating a weaker bond. Kissing bonds are characterized by partial failure of the adhesive holding two adherents together. All the peaks on Figure 59(a)&(b) also appear 0.05 μs later than in Figure 59(c), showing that the sound is slightly delayed. The general shape of the curves indicates that sound intensity decreases faster in the control sample (Figure 59(c)). This can potentially be explained in part by the internal reflections occurring between layers, as explained in Section 6.2, and by impedance mismatch. From the amplitude of the original impulse, it is known that mold release and tape will block some of the sound transmission. It is then possible that internal reflections travelling back towards the transmitter would be reflected towards the receiver at a higher percentage than in the control sample, thus increasing the amplitudes of the subsequent peaks in Figure 59(a)&(b). It is also possible that the inserts better match the impedance of the interface, thus increasing sound transmission and minimizing reflections.

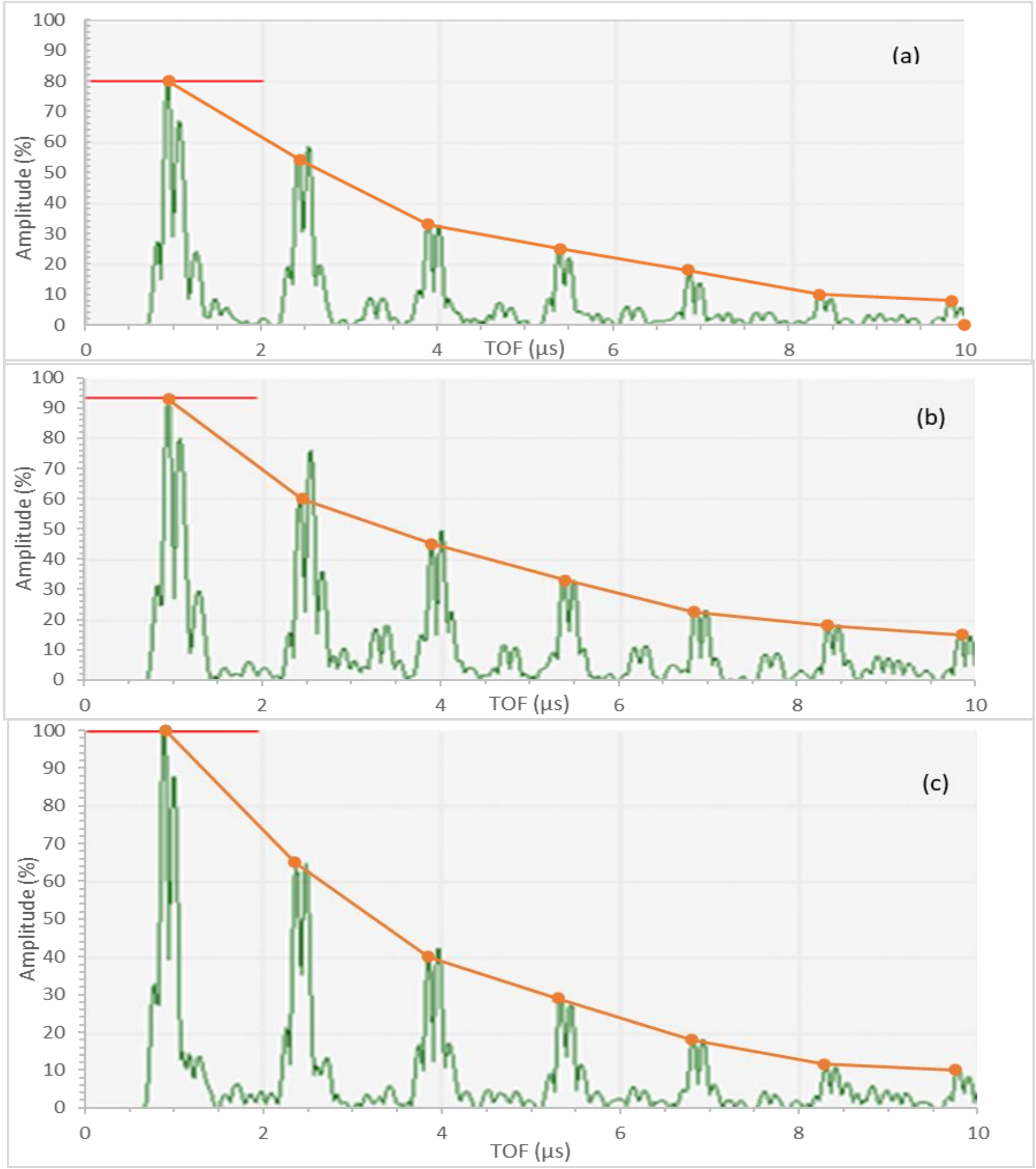

Figure 59. Through-transmission testing (a) defect 1.6 - mold release (b) defect 1.7 -thermal tape (c) defect 1.8 - no disbond.

Through-transmission results show that mold release creates a better artificial disbonds than thermal tape, blocking sound transmission by an additional 10%. However, no major difference was observed from the control sample. There is not, at the moment, any reference quantifying the amount of sound loss a kissing bond should generate. Therefore, the inserts placed in Sample No. 2 were studied to see if sound transmission can be reduced further, while still not appearing as a kissing bond. If unsuccessful at creating kissing bonds, the inserts of Sample No. 2 could then be considered to create disbond signal without the requirement of having to drill a FBH.

Mold release, although creating a greater kissing bond than tape, is harder to apply in a controlled, even fashion. Additionally, it is shown in Section 6.6 that when exposed to heat, mold release can travel inside the sample. The impact of other elements, such as moisture, is not known. Therefore, if the objective is to obtain consistent, repeatable results, thermal tape makes for a better candidate. In Multiple layers of tape were layered to see how that would impact sound transmission. Figure 60 presents the A-Scans of  defects 2.4 (4 layers of tape) and 2.7 (2 layers of tape) side by side, for comparison.

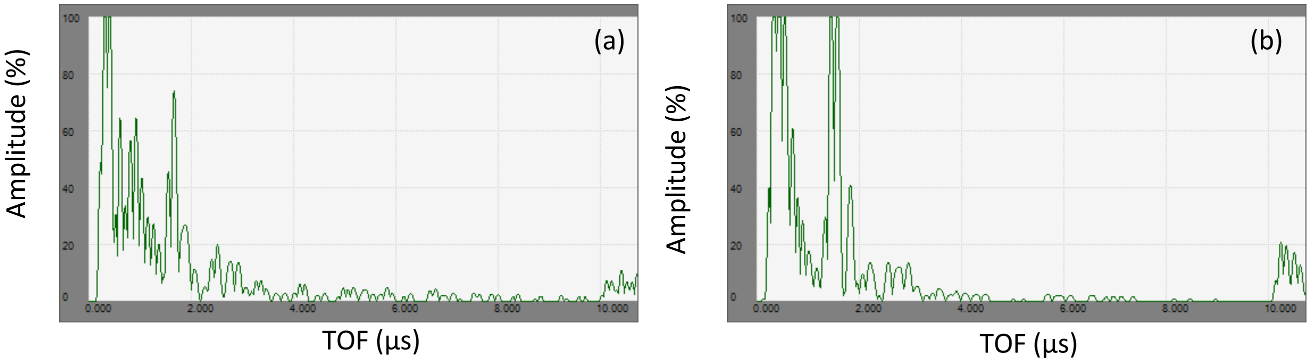

Figure 60.A-Scans of thermal tape (a)defect 2.7 - 2 layers (b) defect 2.4 - 4 layers taken at 5MHz.

Similarities can be observed between Figure 60(a) and (b) and Figure 55(b), which shows a FBH response. At 4 layers, the thermal tape blocks sound almost entirely and the resulting A-Scan has the general shape of a FBH A-Scan. The amplitude of the titanium reflection is higher on Figure 60(b) because almost all of the sound was reflected back when reaching the 4-layer tape disbond. The difference in amplitude for the CFRP peaks is attributable to the near-field effect (see Section 6.1). On Figure 60(a), small reflections are present past the titanium echo, but the A-Scan still resembles more one of a FBH than  the kissing bond showed in Figure 61

Figure 61(b).

Two other conditions were tested to create disbonds: Teflon tape and holes cut out in the adhesive (defects 2.1, 2.2, 2.5 and 2.7) Teflon is readily available in most machine shops and is often used in UT to create a reflector. Cutting actual holes in the adhesive automatically leaves an “air pocket”, required to form a disbond. The square holes were cut with a width of 1.27, 1.9 and 2.54 cm (½”, ¾” and 1”), because it was unknown how much the adhesive would flood back into the hole during curing. All three defects were easy to find during testing, so it is assumed that this factor is negligible and holes could possibly be made smaller.

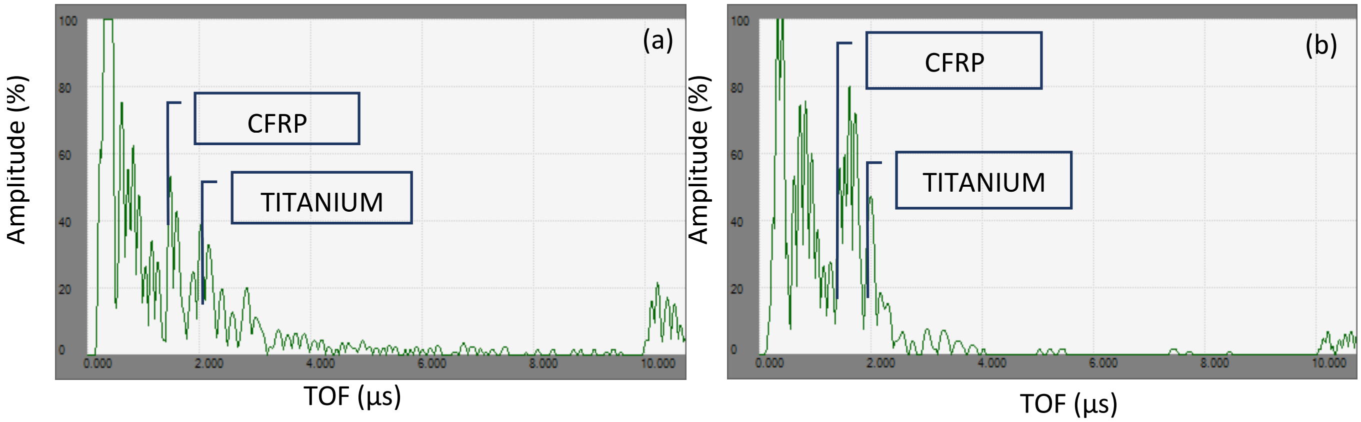

Figure 61. A-Scans of (a) defect 2.1 - Teflon tape (b) defect 2.5 - hole 3/4" width.

Figure 61 shows similarities to Figure 60, in the sense that both Figure 61(a) and Figure 61(b) have the shape of a FBH scan. Teflon tape, as previously mentioned, is often used as a reflector. Figure 58(a) showed that it indeed reflected sound, to the point of presenting results similar to an FBH.

It was expected that removing the adhesive between the CFRP and titanium , and therefore any media for sound to travel through, would create results almost identical to those of a FBH. It was explained in Section 4.3 how solid/air interface causes a sound beam to reflect back at 99.9%. If the intent is to emulate a FBH without having to drill visible holes in a test piece, this suggests an effective way to do it.

Inserts placed in Sample No. 2 did not achieve the more reflective kissing bonds that were intended. Instead, disbonds were simulated, without using FBHs. If results from sample No. 2 are compared to results from Sample No. 1, two conclusions can be drawn; (1) unless inspection data is recorded, detecting kissing bonds can be challenging, as changes in signal amplitude are not as significant as a signal from a real disbond (or a FBH); and (2) creating realistic kissing bonds for training purpose can be difficult. Determining by exactly how much signal amplitudes need to be affected to be considered a kissing bond would be useful. However, of all the different inserts explored in this section, mold release applied over non grit blasted titanium appears to be the most effective way to create a kissing bond.

## 6.6. Analysis of Inspection Data Obtained With the ARMANDA System

At this point it should be noted that finding disbonds during a periodic inspection is actually a rare event. Canada is part of a group of countries who all operate the F/A-18, and share technical information with each other, including NDT findings. Since the IWSLJ became a source of concern in 2016, disbonds were found on only two aircraft from two different countries. All CF-188 were inspected with the ARMANDA system, and no disbonds were found. This coincides with the results of Senevirtne et al. [4] presented in Section 2.6, who showed that the IWSLJ can function well past its life expectancy.

The inspections of all Canadian jets were conducted with the automated inspection system ARMANDA, which uses a 5 MHz probe and presents A-, B- and C-Scans of the inspected region. The delay line it uses is 1” long, and is also used to dispense water, the coupling agent, as it travels on the surface of the lap joint. The speed of sound in the delay line is 2.74 mm/µs. The combination of the three data representations allows the user to perform a more in-depth analysis of the results obtained with the system. As an example, Figure 62 and Figure 63 show, respectively, the A-, B- and C-Scans of a good bond and an IWSLJ with disbonds. B-Scans of both figures were taken at 10 mm on the index axis and 700 mm on the scan axis. By looking at the two A-Scans, the following can be observed: knowing the length of the delay line used and the thickness of CFRP over Step 1, the peak appearing at 18.5 µs in Figure 62(a) can be identified as a front wall echo, followed by the OML 0.4 µs later. The signal shown in Figure 63 (a) shows the front wall and OML echo, but the third peak, representing the back wall echo, is missing. Thus, the signal on Figure 63(a) resembles the signal of a FBH, indicating a true disbond on the OML.

When comparing the B-Scans, the reflections of the different steps, at different depths are observed. However, when looking at Figure 63(c) at index axis 10 mm, the signal seams to disappear at time 20 µs when compared to Figure 62(c). This significant change in the back wall reflection, which should be visible at approximately 23 µs, as seen on Figure 62(c), indicates the presence of a disbond.

B-Scans, similarly to A-Scans, also uses time in µs for its X-Axis. The reflections on a B-Scan are similar to multiple echoes on an A-Scan decreasing in intensity or amplitude over time. When looking at Figure 62(c), echoes are more spaced out, because they represent not only the OML, but the IML and back wall echoes as well. Of note, the area displayed in yellow at the edge of Step 1 in Figure 62(b) was caused by the paint slowly pulling away from the CFRP. The small circles visible on both C-Scans are caused by fasteners.

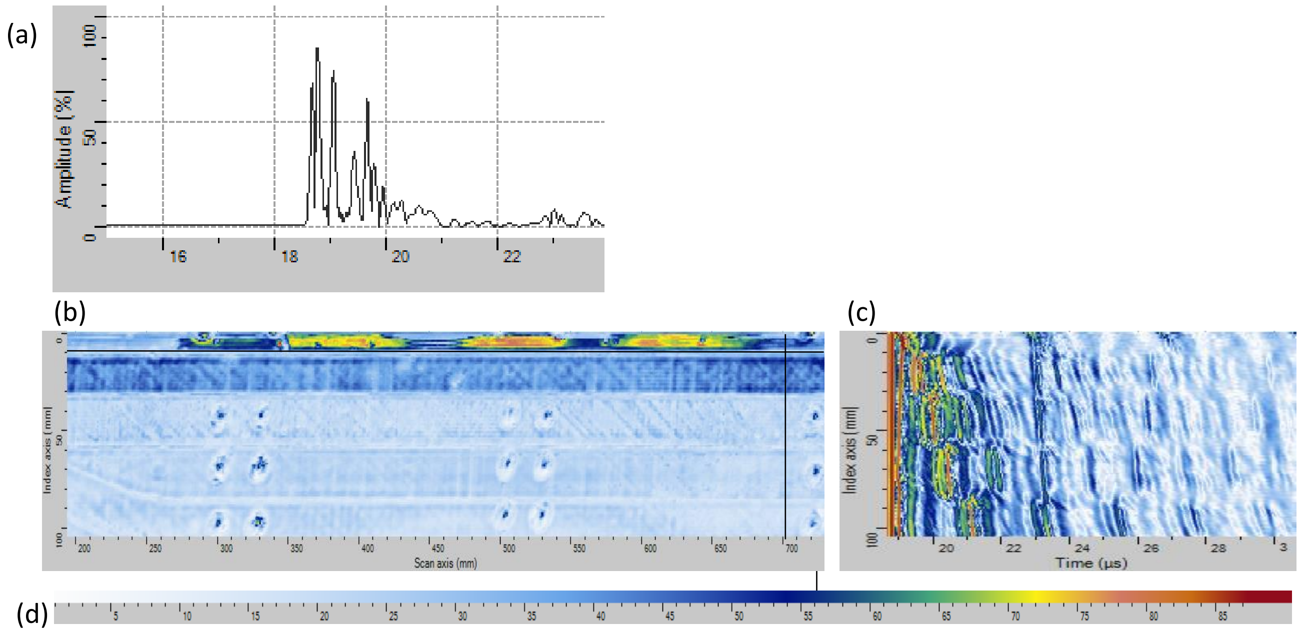

Figure 62. Example of a good bond found with the ARMANDA system on an Upper Wing (a) A-Scan (b) C-Scan (c) B-Scan view and (d) Colour amplitude scale.

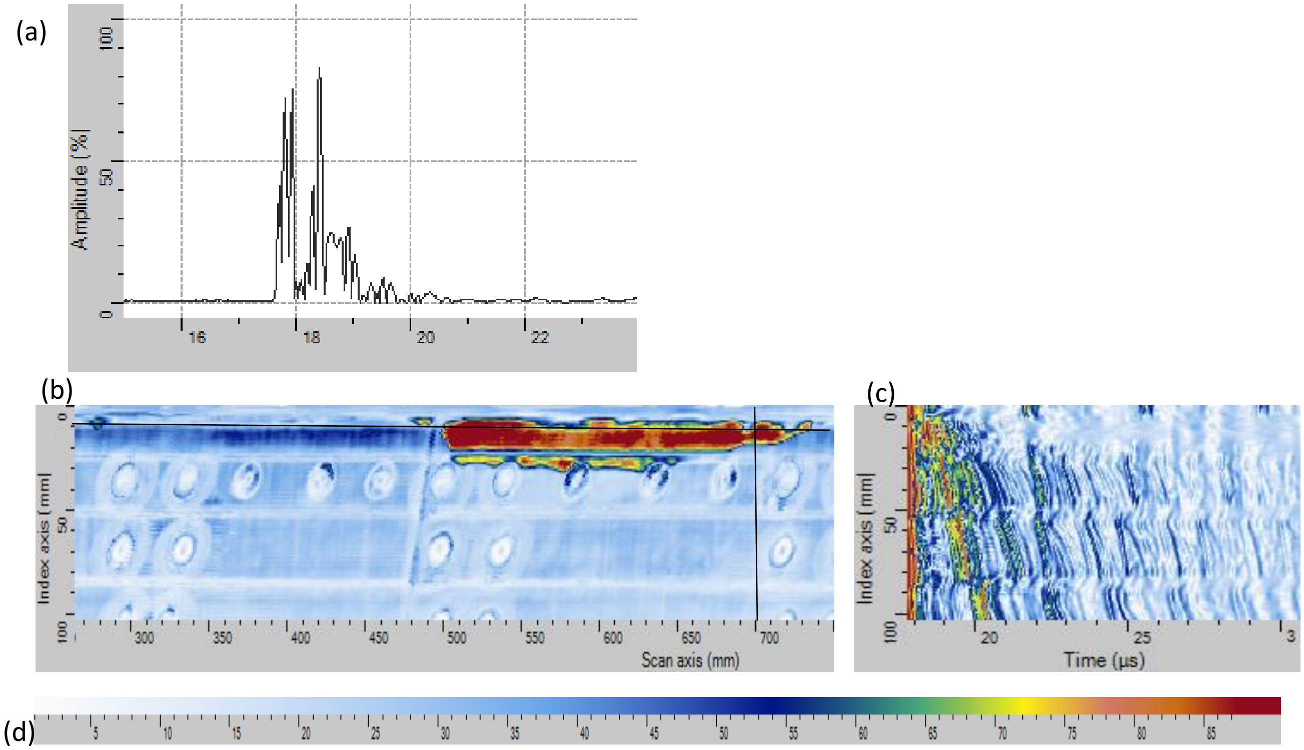

Figure 63. Example of a disbond found with the ARMANDA system on a Lower Wing (a) A-Scan (b) C-Scan (c) B-Scan (d) colour amplitude scale.

The ARMANDA system was also used by QETE to inspect Sample No. 1). Figure 64 shows the resulting C-Scan, obtained with a 5 MHz probe. The FBH in the middle (seeFigure 38) is clearly visible. Additionally, all defects on the bottom row (defects 1.6, 1.7 and 1.8) are more visible than the rest, including the bottom right corner where no inserts were added, but the titanium was not grit blasted. Those results are in agreement with the results discussed in Section 6.5. The piece of tape on the top row (defect 1.2) was applied the CFRP was not sanded, but the titanium were properly prepared. It is visible on the C-Scan, but not as much as the other piece of tape on the bottom row (defect 1.7). Defect 1.2 appears to have weaken the strenght of the bond suronding it, indicated by the green halo around the piece of tape. Yet the sample was not exposed to external stress, except some heat for thermography readings (not related to this thesis). The heat also seems to have an impact on mold release, which travelled from its original location (visible on the bottom left corner). When inspecting the sample with a manual probe at the same frequency, this disbond is the most visible on the A-Scans. Perhaps the mold release applied was thicker in this location.

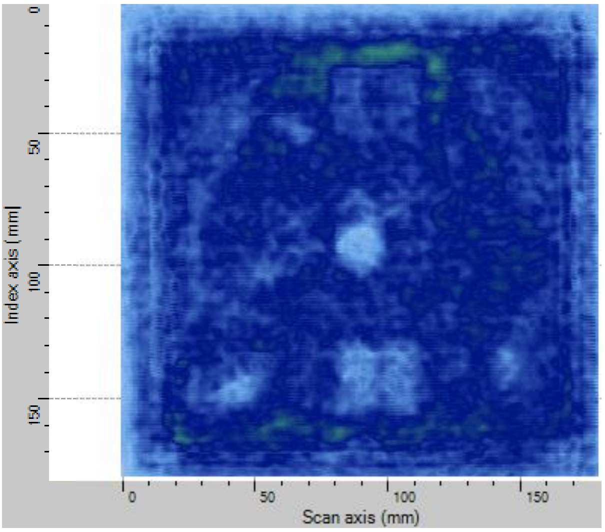

Figure 64. C-Scan of Sample No. 1 obtained with the ARMANDA system.

In order to know if the various inserts of Sample No.1 did in fact create kissing bonds, it is most useful to look at B-Scans. The A-Scans taken with the EPOCH seemed to indicate the presence of kissing bonds, and the C-Scan shown in Figure 64 suggest that indeed, sound transmission is affected at some locations. But, as it was demonstrated in Figure 63(c), B-Scans are a good way to determine if enough sound reached the backwall to create an echo. B-Scans of four different defects on Sample No. 1 are shown in Figure 65 and compared to a good bond. Their relative positions on the sample are expressed in terms of scan axis position (mm) by index axis position (mm) on Figure 65. Note that both Y-axes on Figure 65 and Figure 64 are the same, but Figure 65 has time in μs as its X-axis. Both figures also use the same colour palette as Figure 63 and Figure 64 to indicate peak amplitude. The boxes on each B-Scans highlith where reflections were most affected by the inserts.

First, when comparing element (b) FBH of Figure 65 to Figure 64(c), it can be observed that in both cases there is a discontinuity in the reflection, meaning that sound did not reach the back wall. Similarly, element (a) good bond can be compared to Figure 62(c). In both cases the back wall reflection, shown in dark blue, appear as a continous line, demonstrating that the bond is intact.

Element (d) thermal tape, which was visible on the C-Scan, does not have a visible impact on sound reflection, as the back wall reflection are almost identical to that of Element (a) good bond. This is in accordance with Figure 64, where the tape on the top row is the least visible of all defects present on the C-Scan. From Section 6.5, it is known that one layer of tape does attenuate sound a little, but not as much as mold release. This can again be observed by comparing Elements (d) tape and (c) mold release. On Element (c), the second reflection is much fainter, almost completely invisible. This is similar to what was observed in Figure 56, where the back wall reflection amplitudes were less than 10%,  and Figure 59, where mold release was shown to be more attenuating than tape. Yet, some sound is travelling through it, thus showing that a kissing bond was created. This becomes evident when comparing Element (c) mold release to Element (b) FBH, where the back wall echo is completely absent.

When looking at Element (e) grit blasting, the back wall echoes are all visible, although to a lesser amplitude than Element (a) good bond. This is in accordance with the results shown on Figure 58, where surface treatment was shown to have a small impact on sound transmission. The effects of surface treatment become more apparent when comparing both tape disbonds on Figure 64. Knowing that the tape of the bottom row was applied to titanium that did not undergo grit blasting (see Figure 38), it is interesting to note that it is more visible on the C-Scan. It is likely that the adhesive of the tape, placed on the titanium, did not adhere as well to the metal where surface roughness had not been increased. The flexible adhesive used to bond the titanium and the CFRP showed the same behaviour. Surface treatment can therefore, be considered as a good way to increase the detectability of disbonds, but perhaps it is not the most viable option to create kissing bonds on its own.

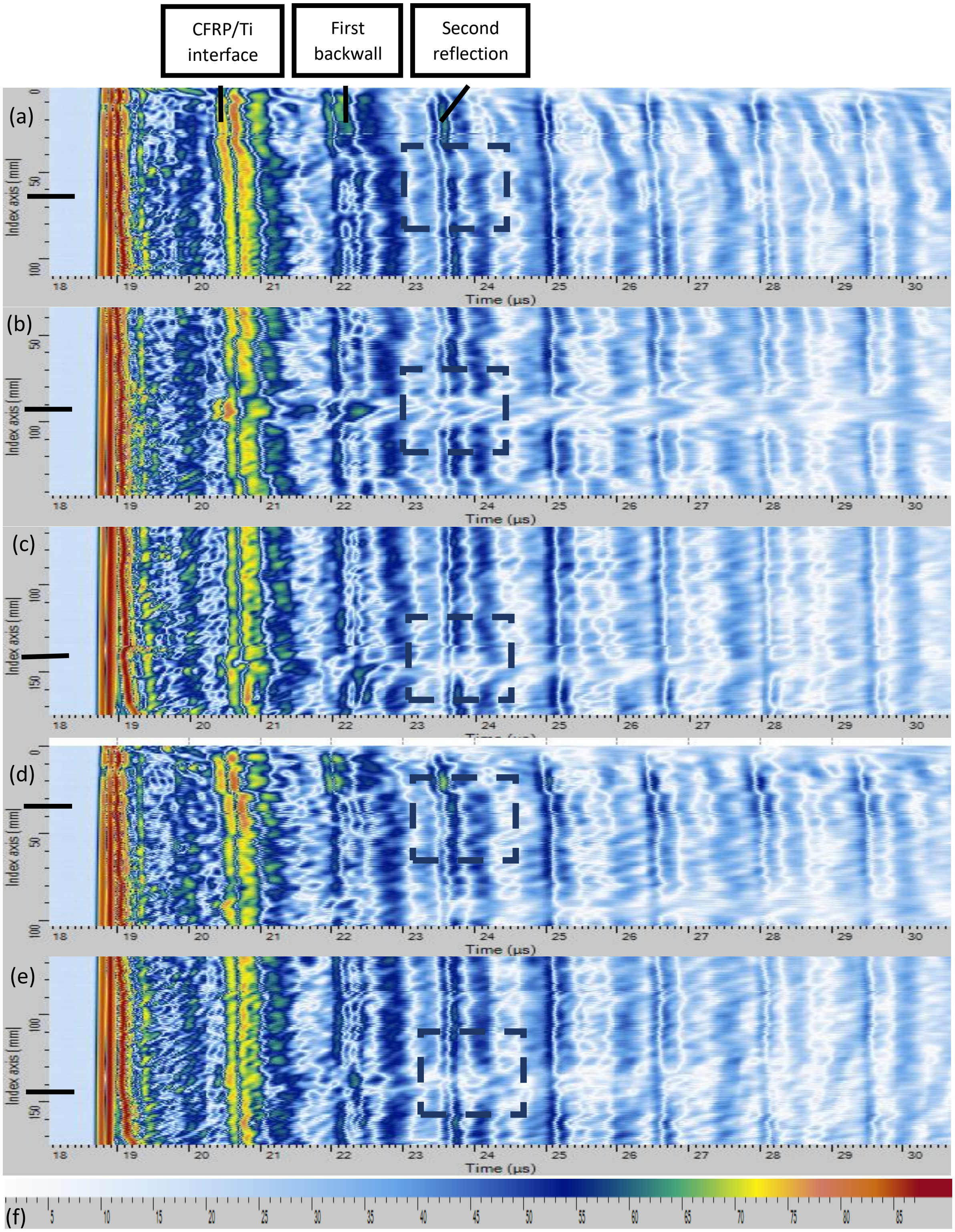

Figure 65. B-Scans of Sample No. 1 (a) good bond, position 150 mm x 65 mm, (b) BFH, position 90 mm x 95 mm (c) Mold release, position 40 mm x 145 mm (d) Thermal tape, position 95 mm x 35 mm (e) Titanium not grit blasted, position 145 mm x 140 mm and (f) colour amplitude scale.

Figure 64 and Figure 65 demonstrate one of the biggest advantage of the ARMANDA system. It generates an image (C-Scan) which, when looked at, direct the attention to possible areas of interrest. When looking at B-Scans of particular regions, highligted on the C-Scan, better knowledge of the condition of the part being inspected can be gained.

It is interesting to note that the ARMANDA system, although technologically more advanced than a manual inspection with a small transducer, faces similar challenges, mostly in the detection of signals coming from the IML. Although no disbonds were ever found on the IML, the ARMANDA system operator who developed the inspection technique [6] for the RCAF is not confident he would be able to identify a disbond on the IML at each step [78]. However, the ARMANDA system does clearly see the IML of Steps 1 to 4 [78]. There was a case (not in Canada) where a delamination was found in the outboard section of the titanium splice. The delamination eventually grew into a OML disbond that extended all the way to Step 2, as shown by the red and yellow on the C-Scan in Figure 66.

One of the potential explanations was that a disbond, present on the IML over Step 9, grew until it became visible as a delamination past the titanium plate. It is theorized that the delamination grew towards the titanium splice plate, eventually creating a major disbond along the OML [78].

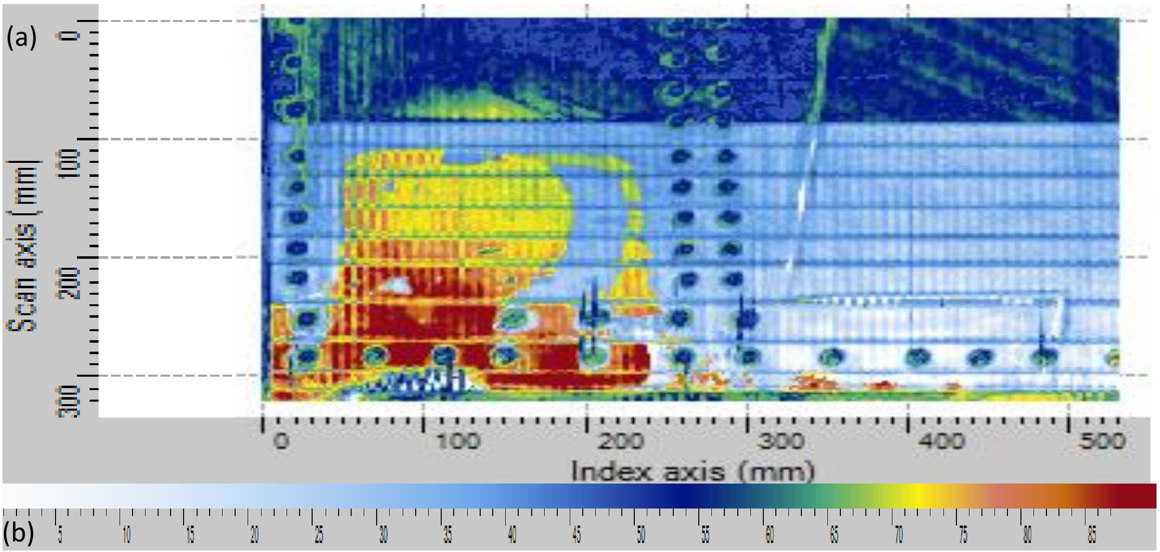

Figure 66. (a) Example of an IML disbond on a lower IWSLJ (b) colour amplitude scale.

The way the lap joint is designed and loaded, it is statistically more probable to find disbonds over Steps 1 and 2 on the OML, and disbonds/delamination on the IML over Steps 8, 9 and in outboard section of the titanium splice. This is why both UT inspections for Canadian jets, the one for the ARMANDA system and the one for manual inspections, ask the operator to inspect up to 5 cm (2”) past the last step.

Additionally, due to the uneven surface of a CF-188 wing and the automated nature of the ARMANDA, the probe has been known to lift off from the surface or tilt on its side, thus rending the inspection results invalid and forcing the operator to start over. It takes, on average, 45 min for the ARMANDA system to inspect the entirety of the IWSLJ, once it is fully set up. This is comparable to what it takes an experienced UT operator to inspect Steps 1 and 2, and the outboard section of the titanium splice with a manual probe, except that set up with the EPOCH© is much quicker. Still, because of its ability to record data and because it offers many ways to look at that data, the ARMANDA system offers many advantages to the RCAF, compared to the EPOCH 600©. The possibility to purchase more systems and to train additional personnel should be investigated.

# 7. Discussion

The IWSLJ is an essential part of the F/A-18 structure. Not only does it help attach the wing to the fuselage, but also, due to its complex design, helps distribute the shear stresses wings undergo through the aircraft’s lifetime. Although Senevirtne et al. [4] made it clear in their study of the inner wing stepped lap joint that it can survive up to ten more lifetimes of cyclic fatigue than originally designed for, some steps will be more prone to disbonds. The study conducted by the RAAF [3] showed that disbonds were more likely to appear on Steps 1 and 2, but could rapidly grow to Step 5 before complete failure of the joint. Periodic ultrasonic inspections are key to keeping the aircraft flying safely. Unfortunately, the complex structure of the lap joint, which makes it so useful, also makes it more challenging to inspect.

The use of carbon fibre on the aircraft is the first challenge that arises when inspecting the IWSLJ. By now, it has been made clear that CFRP is highly attenuating, prone to rich and low resin areas, and its complex nature can cause wave mode conversion under the right circumstances [56], although this is unlikely with a normal beam UT inspection. The acoustic attenuation caused by the composite makes the detection of disbonds on the IML difficult, as only 8% of the signal makes it to the IML and back to the transducer, as described in Section 4.3.

The placement of probes with regards to the Steps makes for another challenge, as any misalignment can cause an operator to interpret the complex signal as a kissing bond. The fact that the pulse echo technique only sends sound normal to the probe surface, and that disbonds are at a higher chance of being detected if they sit perpendicular to the sound beam, makes detection of disbonds at the corners of the steps and along the “step risers” almost impossible with this particular technique. It should be noted that although no information is yet available on the growth speed of disbonds (a study is planned for this at the National Research Council of Canada in the fall of 2021), all disbonds that have been detected so far were considerably large, and have often extended to at least one other step. Figure 63 shows a disbond more than 20 cm long. The likelihood of a disbond along the “step risers” causing failure is then relatively low.

There are a few things that can be done to improve the probability of detecting more disbonds at the titanium/CFRP interface, both on the OML and IML. First, the addition of a delay line to perform an inspection. Section 6 explained what the impact of conducting an inspection in the near field can have. Although the delay line used in this project did not move the interface out of the near field completely, it did reduce the amount of observed pressure fluctuation and improved signal interpretation. The delay line used by the ARMANDA system, which is much longer, did eliminate the near-field effect completely.

The current procedure clearly states that disbonds will show up on the Ultrasonic display the way FBHs do, meaning that inspectors are looking for fully disbonded areas, and only over Steps 1, 2, 8 and 9. But as previously mentioned, there is no information available on the speed with which disbonds can grow to a critical size. It would be worthwhile to find a way to detect kissing bonds, as it could help predict when, where and how fast full disbonds might form. In the context of an aging fleet, having the ability to detect disbonds before they form, and therefore, render a full wing unserviceable, would be a technical and tactical advantage. However, detecting kissing bonds when conducting a manual inspection is challenging. Even if a calibration block could be redesigned and specific training dispensed to operators, the small changes in A-Scan signals that need to be observed can easily be confused with pressure fluctuations due to the near-field effect, uneven pressure applied to the transducer by the operator, or the rough surface of a F/A-18 wing causing the probe to lift up from the surface unintentionally. If kissing bonds were to be detected during a manual inspection, all inspection data would need to be recorded and analyzed after the inspection was complete. Currently, any data analysis is done qualitatively and simultaneously with the scan.

The use of the ARMANDA system is presently reserved for only a few individuals from QETE. The reason being that this system is much more complicated to operate, calibrate and provides more complex data to analyze than a conventional UT instrument. Moreover, the inspections conducted with the ARMANDA system are not intended to replace the periodic inspections done with the EPOCH©. Rather, they are meant to be done once on each aircraft, to gather data on the state of the Canadian fleet. The use of the system may be required again if an aircraft undergoes severe stress such as hard-landing, over-G during flight, or other similar events. The manual inspection outlined in reference [5] is therefore, still the most used. Although conducting a more thorough inspection of the lap joint is technically possible, as was discussed above, most changes would not be practical, except for the use of a delay line. Inspecting more steps than what it being done right now would (1) require fine precision (2) be time consuming and (3) increase the chances of the probe being misaligned. Trying to detect kissing bond with the manual probe exacerbates the chances of false positive calls, due to the small difference observed on an A-Scan signal between a good bond and a kissing bond.

The ARMANDA system eliminates most of the challenges listed above. It was shown in Section 6.6 how this automated system gives a more complete picture of a particular object, providing the operator with A, B and C-Scans to analyze the data while also automatically recording all the data collected, which allows for post data analysis and can serve as a reference point in case an IWSLJ is reinspected. It would therefore, be more practical to look for kissing bonds with this system.

Table 14 summarizes the advantages (Pros) and disadvantages (Cons) of the EPOCH 600© and the ARMANDA system.

Table 14. Pros and Cons of the EPOCH 600© and the ARMANDA system

| EPOCH 600© | | ARMANDA | |
|---|---|---|---|
| Pros | Cons | Pros | Cons |
| • Light weight and portable<br>• Can change probe frequency mid inspection, but requires additional calibration<br>• Requires minimal set up<br>• Inspection takes approx. 45 min | • Live inspection result (no data recording)<br>• Kissing bonds can be easily missed<br>• Disbonds sizes cannot easily be measured<br>• Probe hand held: pressure applied influences amplitudes<br>• Current inspection limited to disbonds over Steps 1 and 2 and delaminations outboard of the titanium splice<br>• May miss small defects<br>• IML disbond detection difficult<br>• Signals can be prone to misinterpretation if steps are not properly located<br>• Inspection conducted in the near field even with a 10 µs delay line | • Records all inspection data, post analysis possible and can serve as a reference on re-inspections<br>• Offers different data presentation views (A, B and C-Scans)<br>• Inspects the entire IWSLJ<br>• Uses a longer delay line and eliminates near field effect<br>• IML disbonds can be seen at Steps 1 to 4 | • Requires advanced training<br>• More expensive<br>• Set-up takes longer<br>• Portable, but has more components (computer, tracks)<br>• Fixed frequency per inspection (still suitable for disbonds and delaminations detection), offset by the data recording capabilities<br>• Inspection takes approx. 45 min, but set-up takes longer |

To emphasize the point, the EPOCH 600© is a great choice to perform qualitative inspections, focusing on full disbonds on the OML. The ARMANDA system offers the possibility to analyze the data post inspection, thus enhancing the probability of detecting kissing bonds, and possibly on the IML. In the context of an aging fleet, the data recording feature of the ARMANDA gives it a clear advantage over the EPOCH©. However, it requires more intensive training, is more expensive and more difficult to set up. It is therefore unlikely that the ARMANDA will be distributed to the main air force bases operating the CF-188. The most realistic option is to keep using the EPOCH©, but add a delay line of sufficient length to the inspection procedure.

In light of what has been discussed, it can be said that inspections should be conducted with the ARMANDA system. If and when that is not possible, however, the following some minor modifications to the current procedure [5] are recommended. First, changes could be made to the block currently being used: FBHs are currently drilled from the back wall up to the OML. Having FBH or varying depths, up to the IML for example, would be advisable. However, in order to have FBHs reaching the IML, holes would need to be drilled through the second layer of CFRP. Composites in general do not agree well with holes. It can be done, but the use of inserts, creating kissing of full disbonds, could be added to the block instead. This would make for a great training aid. Although unlikely at this time, in the eventuality that a disbond occurs on the IML, the suggested changes would provide a point of reference to help with their identification. Additionally, use of a delay line should be added to the inspection procedure outlined in [5], as the negative impact of pressure fluctuations on measurements taken in the near field has been shown in this thesis.

# 8. Conclusion

In this thesis, challenges that arise while inspecting the IWSLJ were identified and suggestions to address them were made. The attenuation coefficient of CFRP was obtained at 2.25, 5 and 10 MHz, and shown to be consistent with literature values. It was demonstrated that the addition of a delay line improved near-surface resolution for inspection of thin CFRP layers, such as those that occur over Steps 1 and 2. It was also shown that the delay line reduces background noise level, thus making the IML and back wall reflection more visible and facilitating interpretation of inspection results. The impact of kissing bonds in reducing bond strength was demonstrated. It was also shown that detecting kissing bonds, with a manual transducer or with the ARMANDA, can be challenging. Therefore, their detection should play a more crucial role in operator training. In the case that kissing bonds become more of a concern in the industry, this thesis suggested ways in which kissing bonds could be inserted in training aids.

Until more information is available on disbond growth rates, it would be preferable to create training aids with artificial inserts creating kissing bonds. Not grit blasting the titanium, and inserting thermal tape, appears to be the most effective way to create a repeatable kissing bond.

Given the aging state of the RCAF CF-188 fleet and the fact that disbonds were found on F/A-18 in other countries, it can be anticipated that disbonds will eventually appear on Canadian jets. Until more is known about the growth and critical size of disbonds, inspections should aim at detecting disbonds, while they still present as kissing bonds.

# 9. Future Work

This thesis proposes that the fabrication of a new calibration block, with FBHs drilled up to the OML, but also up to the IML could increase the chances of detecting disbonds on the IML. If a new block is designed, the incorporation of kissing bonds should be considered. An insert creating a kissing bond showing similar signal at every inspection should be selected, and the fabrication process should be written down so that it can be reproduced. Once additional data is available on kissing bonds and disbond growth rates, the exact amount by which amplitudes need to decreased to indicate a kissing bond should be determined. Once that threshold is established, inspecting the IWSLJ with gates located at that threshold could help identify kissing bonds.

In the eventuality that the CAF does not to procure more ARMANDA systems and that the training of additional personnel is not possible, it is recommended that future work include a way to automatically record inspection data taken by the EPOCH 600©, as the inspections are presently only conducted in real time. This would allow for the possibility to apply denoising algorithms to that data. There exist many algorithms, not all operating on the same principles that could be implemented. The option to use one of those algorithms to detect kissing bonds and disbonds on the IML should be investigated further.

The possibility to conduct this inspection with a phased array system should also be investigated. The use of such a system is not expected to improve the detection of disbonds on the OML, since disbonds can be clearly detected by conventional UT. However, it should be determined if the beam steering and focusing capability of PAUT increase chances of detecting disbonds on the IML, and potentially kissing bonds.

It was explained in Section 6.2 how the internal reflections of the IWSLJ affect sound transmission. A modelling approach could potentially account for internal reflections and large attenuation losses in the CFRP. Because the number of interfaces is constant through the joint, such model could be used to predict the amplitude decay of back wall reflections at each step, and therefore could potentially identify kissing bonds, if the signal amplitude loss is greater than predicted.

# References

[1] G. Aranguren, J. Etxaniz, S. Cantero-Chinchilla, J.M. Gil-Garcia, M.K. Malik, "Ultrasonic Guided Wave Testing on Cross-Ply Composite Laminate: an Ampirical Study," Sensors, pp. 1-18, 16 September 2020.

[2] W. Feng, X. Zhou, X. Zeng, X. Yang, "Ultrasonic Inspection of Localized Defects in low-porosity CFRP," Sensors, pp. 1-16, 6 April 2019.

[3] J. Hayes-Griss, J. Wang, A. Litchfield, A.D.M. Charles , "Numerical Analyses of F/A-18 wing root Step-Lap Joints -Part 2: Assessment of Disbond Progression Behaviour," Australian Governement - Department of Defence Sicence and Technology, 2017.

[4] W. Senevirtne, J. Tomblin M. Kittur, "Durability and residual strength of adhesively-bonded composite joints: the case of F/A-18 A-D wing root stepped-lap joint," in Fatigue and Fracture of Adhesively-Bonded Composite Joints: Behaviour, simulation and Modeling, Woodland Publishing, 2015, pp. 289-320.

[5] ATESS, Canadian Forces Ultrasonic Inspection 188-338-U Rev 2, Ottawa, Ontario: National Defence, 2015.

[6] ATESS, Automated Ultrasonic Inspection 188-355-U, Ottawa: National Defence, 2019.

[7] ASTM International, Apparent Shear Strength of Single-Lap-Joint Adhesively Bonded Metal Specimens by tension Loading, West Conshohocken, PA: ASTM international, 2019.

[8] G. Blessing, An Assessment of Ultrasonic Reference Block Calibration Methodology, Washington, DC: U.S. Department of Commerce, 1983.

[9] M.I. Hussain, Z.M. Zain, T.L. Kee, "Root Causes Analysis of Disbonds and Unidentifiable Ultrasonic Indications on Composite Materials," Applied Mechanics and Materials, Vols. 465-466, no. December 2013, pp. 1304-1308, 2013.

[10] HEXCEL, HexPly® 3501-6 High strength, damage-resistant, structural epoxy matrix product data sheet, Hexcel corporation.

[11] M. Peters, J. Hemptenmacher, J. Kumpfert, C. Leyens, "Structure and Properties of Titanium Alloys," in Titanium and Titanium Alloys, Weinheim, WILEY-VCH, 2003, pp. 1-36.

[12] M. Wojtaszek, T. Śleboda, A. Czulak, G. Weber, W.A. Hufenbach, "Quasi-Static and Dynamic Tensile Properties of Ti-6Al-4V Alloy," Archives of Metallurgy and Materials, vol. 58, no. 4, pp. 1261-1265, 2013.

[13] W.D. Callister Jr., D.G. Rethwisch, Material Science and Engineering, An Introduction, eigth eidition, Hoboken, NJ: John Wiley & Sons, Inc., 2010.

[14] C. Soutis, "Carbon fiber reinforced plastics in aircraft construction," Material Science and Engineering, vol. 412, no. 1-2, pp. 171-176, December 2005.

[15] D. Chung, Carbon Fiber Composites, Newton, MA: Butterworth-Heinemann, 1994.

[16] HEXCEL, HexTow® AS4C Carbon fiber product data sheet, Hecxel corporation.

[17] M. Wisnom, "The role of Delamination in Failure of Fibre-Reinforced Composites," Philosophical Transactions of the Royal Society A, vol. 370, no. 1965, pp. 1850-1870, 2012.

[18] F. Campbell, "Introduction to composite materials," in Structural Composite Materials, Cleaveland, Ohio, ASM International, 2010, pp. 1-29.

[19] J. Kuczmaszewski, Fundamentals of Metal-Metal Adhesive Joint Design, Lubln, Poland: Politechnika Lubelska, 2006.

[20] F. Heidarpour, M. Farahani, P. Ghabezi, "Experimental Investigation of the Effects of Adhesive Defects on the Single lap Joint Strength," International Journal of Ahesion and Adhesives, vol. 80, pp. 128-132, 2018.

[21] S.G. Prolongo, G. del Rosario, A. Urena, "Comparative Study on the Adhesive Properties od Different Epoxy Resins," International Journall of Adhesion ad Adhesives, vol. 26, pp. 125-132, 2006.

[22] M.J. Davis, D.A. Bond, The Importance of Failure Mode Identification in Adesive Bonded Aircraft Structures and Repairs, Melbourne, Australia: Directorate Genaral of Technical Airworthiness Royal Australian Air Force, 2010.

[23] P. Molitor, V. Barron, T. Young, "Surface treatment of titanium for adhesive bonding to polymers composites: a review," International Journal of Adhesion & Adhesives, vol. 21, pp. 129-136, 2001.

[24] P. Qiu, J. Shi, J. Zheg, "Experimental Investigation on Adhesive Bonded Joints of Carbon Fiber Composite Laminates Containing Disbond Defect," in ASME 2017 Pressure Vessels and Piping Conference, Waikoloa, Hawaii, 2017.

[25] M.J. Davis, A. McGregor, "Assesing Adhesive Bond Failures: Mixed-Mode Bond Failures Explained," in ISASI Australian Safety Seminar, Canberra, 2010.

[26] J. T. Cannon, S. Dostrovsky, The Evolution of Dynamics: Vibration Theory from 1687 to 1742, New-York, NY: Spriger- Verlag, 1981.

[27] D. Griffiths, Introduction to Electrodynamics, Pearson, 2012.

[28] T. Arens, "Helmholtz Equation," in Waveguides and Scatering, 2001, p. section 17.

[29] R. Keim, "All About Circuits - Technical Article," EETech Media, LLC., 30 07 2020. [Online]. Available: https://www.allaboutcircuits.com/technical-articles/what-is-the-fourier-transform/. [Accessed 31 03 2021].

[30] M. Heald, J.B. Marion, Classical Electromagnetic Radiation, Sarthmore, Pennsylvania: Sauders College Publishing, 1995.

[31] D. Rowell, 2.161 Signal Processing- Continuous and Discrete Lecture 1, Cambridge, Massachusetts: Massachusetts Institute of Technology, Dept of Mechanical Engineering, 2008.

[32] C. Stover, "Green's Function," MathWorld--A Wolfram Web Resource, [Online]. Available: https://mathworld.wolfram.com/GreensFunction.html. [Accessed 09 05 2021].

[33] J. L.W. Schemerr, Fundamentals of Ultrasonic Nondestructive Evaluation, A Modeling Approach, Ames, Iowa: Springer, 2016.

[34] A. Ahmad, L.J. Bond, "Fundamentals of Ultrasonic Inspection," in ASM Handook - Volume 17, Nondestructive Evaluation of Materials, Russell, Ohio, ASM International, 2018, pp. 155-168.

[35] D.E. Bray, R.K. Stanley, Nondestructive Evaluation: a tool in design, manufacturing and service, Huston, Texas: Taylor&Francis, 1997.

[36] J. Krautkrämer, H. Krautkrämer, Ultrasonic Testing of Materials, Berlin: Springer-Verlag, 1990.

[37] S. J. Rupitsch, Piezoelectric Sensors and Actuators, Fundamentals and Applications, Berlin, Germany: Srpinger-Verlag, 2019.

[38] W. McAllister, "RLC natural Response- Variations," Khan Academy , [Online]. Available: https://www.khanacademy.org/science/electrical-engineering/ee-circuit-analysis-topic/ee-natural-and-forced-response/a/ee-rlc-natural-response-variations. [Accessed 13 05 2021].

[39] Olympus NDT, Inc, EPOCH 600 User's manual, Waltham, Maine: Olympus NDT, Inc, 2011.

[40] S. Edelman, "Ultrasond Physics," in Examination of Special Competence in Adult Echocardiography (ASCeXAM), ESP Ultrasound, 2011, pp. 1-47.

[41] "Center for Non-Destructive Evaluation - Attenuation of Waves," Iowa State University, [Online]. Available: https://www.nde-ed.org/Physics/Waves/attenuation.xhtml. [Accessed 13 05 2021].

[42] E.M. Strohm, M.C. Kolios, "Sound Velocity and Attenuation measurements of Perflurocarbon Liquids Using Photoacoustic Methods," in 2011 IEEE International Ultrasonics Symposium, Orlando, Florida, 2011.

[43] A. Hijazi, Introduction to Non-Destructive Testing Techniques - Ultrasound Testing (course notes), Amman, Jordan: German Jordanian University - Dept of Mechanical Engineering.

[44] J. Pitkänen, W. Arnold, S. Hirsekorn, "The Effect of Grain Size on the Defect Detectability in Copper Components in Ultrasonic Testing," in 6th international Conferenceon NDE in Relation to Structural Integrity for Nuclear and Pressurized Components, Budapest, Hungary, 2007.

[45] R. Li, N. Toshiaki, X. Hong, "Analysis of Individual Attenuation Components of Ultrasonic Waves in Composite Material Considering Frequency Dependence," Composties Part B: Engineering, vol. 140,

no. May 2018, pp. 232-240, 2018.

[46] "NDT ressource center," National Science Fondation, [Online]. Available: https://www.nde-ed.org/GeneralResources/MaterialProperties/UT/ut_matlprop_liquids.htm. [Accessed 18 November 2020].

[47] A. Selfridge, "Platic Material's acoustic properties," IEEE, 05 1985. [Online]. Available: https://www.ndt.net/links/proper.htm. [Accessed 13 04 2021].

[48] K. Peimandis, NASA Contractor Report 187229 - Environmental and Strain Rate Effects on Graphite/Epoxy Composites, Evanston, Illinois: NASA, 1991.

[49] A. Hijazi, Introduction to Non-Destructive Testing Techniques - Ultrasound Testing (course notes), Amman, Jordan: German Jordanian University - Dept of Mechanical Engineering.

[50] S. Edelman, "Ultrasond Physics," in Examination of Special Competence in Adult Echocardiography (ASCeXAM), ESP Ultrasound, 2011, pp. 1-47.

[51] Iowa State University, "Center fo Nondestructive Evaluation - Transducer Beam Spread," American Society for Nondestructive Testing, [Online]. Available: https://www.nde-ed.org/NDETechniques/Ultrasonics/EquipmentTrans/transducertypes.xhtml. [Accessed 6 03 2021].

[52] "NDT Kits," Honesdom International (HK), 12 May 2013. [Online]. Available: http://www.ndt-kits.com/blog/sgs-ndt-services-for-paper-mill-expansion-in-south-africa/. [Accessed 18 February 2021].

[53] Q. Shen, M. Omar, S. Dongri, "Ultrasonic NDE techniques for Impact Damage Inspection on CFRP Laminates," Journal of Materials Science Research, vol. 1, no. 1, pp. 1-15, 2012.

[54] J. Frouin, S. Sathish, T.E. Matikas, J.K. Na, "Ultrasonic Linear and Nonlinear Behavior of Fatigued Ti-6Al-4V," Journal of Materials Research, vol. 14, no. 4, pp. 1295-1298, 1999.

[55] "Velocity of Sound in Solid Metals," Engineering ToolBox, 2004. [Online]. Available: https://www.engineeringtoolbox.com/sound-speed-solids-d_713.html. [Accessed 26 02 2021].

[56] S.J. Wilkinson, W.N. reynolds, "The propagation of Ultrasonic waves in Carbon-Fibre-Reinforces Plastics," Journal of Physics D: Applied Physics, vol. 7, pp. 50-57, 1974.

[57] "NDT ressource center - Data Presentation," National Science Fondation, [Online]. Available: https://www.nde-ed.org/EducationResources/CommunityCollege/Ultrasonics/EquipmentTrans/DataPres.htm. [Accessed 31 01 2021].

[58] M.A. Abdullah, M.F.Z. Abidin, A.B. Elmi, M.F. Mahmod, "Feature Analysis Thru Image Recognition of C-Scan Image from Composite Laminated Materials," in 27th International Invention & Innovation Exhibition , Kuala Lumpur, Malaysia, 2016.

[59] "Phased Array Tutorial - Phased Array Sectorial Scans," Olympus Coporation, [Online]. Available: https://www.olympus-ims.com/en/ndt-tutorials/instrumententation/pa-scan/. [Accessed 24 03 2021].

[60] J. Poguet, A. Garcia, J. Vazquez, J. Marguet, F. Piochonnat, "Phased Array Technology Concepts, probes and appications," in 8th European Congress On Non destructive Testing, Barcelona, Spain, 2002.

[61] S. Cochran, "Fundamantals of Ultrasonic Phased Arrays," Insight- Non-Destructive Testing and Condition Monitoring, vol. 48, no. 4, pp. 212-217, 2006.

[62] L. Azar, Y. Shi, S.-C.Wooh, "Beam Focusing behaviour of linear phased arrays," NDT&E international, vol. 33, pp. 189-198, 2000.

[63] L. Schmerr, Fundamentals of Ultrasonic Phased Arrays, Ames, Iowa: Springer, 2015.

[64] R.J. Ditchburn, M.E. Ibrahim, Ultrasonic Phased Arrays for the Inspection of Thick Section Welds, Victoria, Australia: Australian Government Department of Defence - Science and Technology Organisation, 2009.

[65] V. Kappatos, G. Asfis, K. Salonitis, V. Tzitzilonis, N. P. Avdelidis, E. Cheilakou, P. Theodorakeas, "Theoretical Assessment of Different Ultrasonic Configurations for Delamination Defects Detection in Composite Components," in The 5th International Conference on Through-life Engineering Services, Cranfield, UK, 2016.

[66] F. Meng, X. Ma, C. Xu, J. Ren, Z. Zhang, T. Zhang, "Recent Advances in Ultrasonic Volume Vizualization," in Far East NDT New Technology & Application Forum (FENDT), NanChang, China, 2016.

[67] D. Pagodinas, K.Baršauskas, "Ultrasonic Signal Processing Methods for Detection of Defects in Composite," Ultragarsas, vol. 4, no. 45, pp. 47-54, 2002.

[68] K.A. Tiwari, R. Raisutis and V. Samaitis, "Hybrid Signal Processing Technique to Improve the Defect Estimation in Ultrasonic Non-Destructive Testing of Composite Structures," Sensors, vol. 17, no. 12, p. 2858, 2017.

[69] M. Stone, "The Effect of Silane Coupling Agents on the," The Journal of Adhesion, vol. 26, no. 2-3, pp. 101-111, 2006.

[70] A. Fink, S. Sophabmixay, W. Dumars, "Developement of an Improved Surface Preparation for Titanium Bonding and Titanium Graghite Laminates for Aircraft and Space Vehicule Applications," in AIRTEC, 5th International Conference, Frankfurt, Germany, 2010.

[71] I. S. University, "Center for Non Destructive Evaluation: Transducer Types," the American Society for Non Destructive Testing, [Online]. Available: https://www.nde-ed.org/NDETechniques/Ultrasonics/EquipmentTrans/transducertypes.xhtml. [Accessed 04 03

2021].

[72] Tec-Science, "Ultrasonic Testing (UT)," 13 07 2018. [Online]. Available: https://www.tec-science.com/material-science/material-testing/ultrasonic-testing-ut/. [Accessed 04 03 2021].

[73] Olympus, "Standard Delays," Olympus Corporation, [Online]. Available: https://www.olympus-ims.com/en/store/delay-line/delays/standard/. [Accessed 12 04 2021].

[74] "Electronics Note," Radio-Electronics.com, 2016. [Online]. Available: https://www.electronics-notes.com/articles/basic_concepts/decibel/neper-to-db-conversion.php. [Accessed 02 05 2021].

[75] "Center for Nondestrucive Evaluation - Signal-to-Noise Ratio," Iowa State University, [Online]. Available: https://www.nde-ed.org/Physics/Waves/signaltonoise.xhtml. [Accessed 31 08 2021].

[76] E. Hamm, P. Reis, M. LeBlanc, B. Roman and W. Cerda, "Tearing as test for mechanical characterization of thin adhesive film," Nature Materials, vol. 7, pp. 386-390, 2008.

[77] Unknown, Technical Data Sheet FM 300 Adhesive Film, Alpharetta, GA: Solvay, 2018.

[78] S. Savage, Interviewee, Email Correspondance. [Interview]. 27 05 2021.

[79] L.L. Beranek, T.J. Mellow, Acoustics: Sound Field and Transducers, Oxford, UK.: Elsevier, 2012.

# Appendices

# Appendix 1. Theoretical Attenuation coefficient

To calculate the attenuation coefficient, the initial sound pressure, as well as the sound pressure at a distance d from the transducer must be known. Since the normalized sound pressure is calculated in Appendix 2, it is assumed that the initial pressure, $P_o$ is 1. The sound pressures at different distances are determined in A2. The attenuation coefficient is only calculated in the far field.

From equation 4.16, for a 5 MHz transducer of 6.35 mm diameter, the near field ends at 19.09 mm.

Using equation 4.8, and diving by z, yields the alpha coefficient. Note that it is not constant. The pressure needs to be recalculated with the help of equation 4.5, so that it can be plotted against z. From that curve, an exponential trend line gives the overall alpha coefficient.

Table A.1. Calculation of the attenuated pressure at different z values

| Z (mm) | \|p\| | $20log\left(\frac{1}{\|p\|}\right)$ | α | $p = exp^{-ad}$ |
|---|---|---|---|---|
| 19.0 | 0.6302 | 4.0109 | 0.2111 | 0.018117 |
| 19.5 | 0.6167 | 4.1989 | 0.2153 | 0.015013 |
| 20 | 0.6037 | 4.3839 | 0.2192 | 0.012477 |
| 20.5 | 0.5912 | 4.5660 | 0.2227 | 0.0104 |
| 21 | 0.5791 | 4.7452 | 0.2260 | 0.008693 |
| 21.5 | 0.5674 | 4.9216 | 0.2289 | 0.007288 |
| 22 | 0.5562 | 5.0952 | 0.2316 | 0.006126 |
| 22.5 | 0.5454 | 5.2660 | 0.2340 | 0.005164 |
| 23 | 0.5349 | 5.4341 | 0.2363 | 0.004365 |
| 23.5 | 0.5248 | 5.5995 | 0.2383 | 0.0037 |
| 24 | 0.5151 | 5.7623 | 0.2401 | 0.003144 |
| 24.5 | 0.5057 | 5.9226 | 0.2417 | 0.002678 |
| 25 | 0.4966 | 6.0803 | 0.2432 | 0.002287 |
| 25.5 | 0.4878 | 6.2357 | 0.2445 | 0.001958 |
| 26 | 0.4793 | 6.3886 | 0.2457 | 0.001681 |

|  |  |  |  |  |
|---|---|---|---|---|
| 26.5 | 0.4710 | 6.5392 | 0.2468 | 0.001446 |
| 27 | 0.4630 | 6.6875 | 0.2477 | 0.001246 |
| 27.5 | 0.4553 | 6.8336 | 0.2485 | 0.001077 |
| 28 | 0.4478 | 6.9776 | 0.2492 | 0.000933 |
| 28.5 | 0.4406 | 7.1194 | 0.2498 | 0.000809 |
| 29 | 0.4336 | 7.2592 | 0.2503 | 0.000704 |
| 29.5 | 0.4267 | 7.3969 | 0.2507 | 0.000613 |
| 30 | 0.4201 | 7.5327 | 0.2511 | 0.000535 |
| 30.5 | 0.4137 | 7.6666 | 0.2514 | 0.000468 |
| 31 | 0.4074 | 7.7986 | 0.2516 | 0.00041 |
| 31.5 | 0.4014 | 7.9288 | 0.2517 | 0.00036 |
| 32 | 0.3955 | 8.0572 | 0.2518 | 0.000317 |
| 32.5 | 0.3898 | 8.1839 | 0.2518 | 0.000279 |
| 33 | 0.3842 | 8.3088 | 0.2518 | 0.000246 |
| 33.5 | 0.3788 | 8.4322 | 0.2517 | 0.000218 |
| 34 | 0.3735 | 8.5539 | 0.2516 | 0.000193 |
| 34.5 | 0.3684 | 8.6740 | 0.2514 | 0.000171 |
| 35 | 0.3634 | 8.7926 | 0.2512 | 0.000152 |
| 35.5 | 0.3585 | 8.9096 | 0.2510 | 0.000135 |
| 36 | 0.3538 | 9.0253 | 0.2507 | 0.00012 |
| 36.5 | 0.3492 | 9.1394 | 0.2504 | 0.000107 |
| 37 | 0.3447 | 9.2522 | 0.2501 | 9.59E-05 |
| 37.5 | 0.3403 | 9.3636 | 0.2497 | 8.58E-05 |
| 38 | 0.3360 | 9.4737 | 0.2493 | 7.69E-05 |
| 38.5 | 0.3318 | 9.5824 | 0.2489 | 6.89E-05 |
| 39 | 0.3277 | 9.6899 | 0.2485 | 6.19E-05 |
| 39.5 | 0.3237 | 9.7961 | 0.2480 | 5.57E-05 |
| 40 | 0.3199 | 9.9011 | 0.2475 | 5.01E-05 |
| 40.5 | 0.3161 | 10.0049 | 0.2470 | 4.52E-05 |
| 41 | 0.3123 | 10.1075 | 0.2465 | 4.08E-05 |
| 41.5 | 0.3087 | 10.2089 | 0.2460 | 3.68E-05 |
| 42 | 0.3052 | 10.3093 | 0.2455 | 3.33E-05 |
| 42.5 | 0.3017 | 10.4085 | 0.2449 | 3.02E-05 |

| | | | | |
|---|---|---|---|---|
| 43 | 0.2983 | 10.5067 | 0.2443 | 2.74E-05 |
| 43.5 | 0.2950 | 10.6038 | 0.2438 | 2.48E-05 |

When plotting the new pressure against Z, Figure A. 1 is obtained:

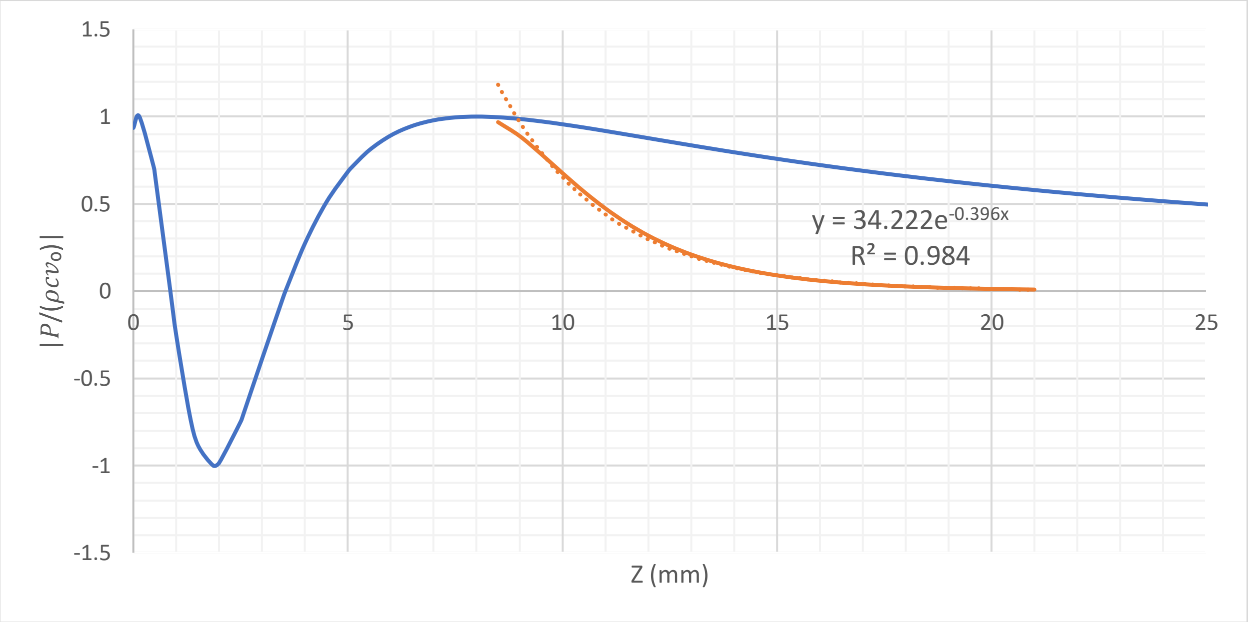

Figure A. 1. Magnitude of the normalized on-axis Pressure for a Plane Piston Transducer in Titanium, f= 5MHz

The exponential trend line shown in Figure A. 1 has the form $P=P_0e^{-\alpha z}$. Because α was calculated with equation 4.8, α is equal to 0.4 dB/mm.

# Appendix 2. On-Axis Pressure Fluctuations

This appendix presents the calculation steps required to obtain Figure 25 and Figure 43. As an example, the on-axis pressure fluctuation for CFRP at a frequency of 10 MHz are shown.

Constants:

$\omega = 2\pi f$ $f = 10MHz$ $\omega = 62.83s^{-1}$

$k = \frac{\omega}{c}$ $c = 2.622\frac{mm}{\mu s}$ $k = 23.96$ (The wave number is unitless)

With the above constants established, the location of nulls and maximum pressure points are determined using equations 4.22 and 4.25. Results are shown in Table A.2

Table A.2 Null and maximum pressure position along the Z-Axis for CFPR at 10 MHz

| n= | Equation 4.22: null positions (mm) | Equation 4.25: Maximum positions (mm) |
|---|---|---|
| 0 | | 38.38 |
| 1 | 19.09 | 12.62 |
| 2 | 9.35 | 7.36 |
| 3 | 6.01 | 5.03 |
| 4 | 4.28 | 3.68 |
| 5 | 3.19 | 2.77 |
| 6 | 2.42 | 2.11 |
| 7 | 1.83 | 1.58 |
| 8 | 1.35 | 1.15 |
| 9 | 0.96 | 0.78 |
| 10 | 0.61 | 0.45 |
| 11 | 0.31 | 0.16 |
| 12 | 0.03 | N/A |

The normalized pressure is derived from equation 4.20:

$$p(z,\omega) = -2i\rho c v_0(\omega)\sin\left(\frac{k\left(\sqrt{z^2+a^2}-z\right)}{2}\right)\left[e^{\frac{ik\left(\sqrt{z^2+a^2}+z\right)}{2}}\right] \tag{A.1}$$

And becomes:

$$\left|\frac{p(z,\omega)}{\rho c v_0(\omega)}\right| = -2i\sin\left(\frac{k\left(\sqrt{z^2+a^2}-z\right)}{2}\right)\left[e^{\frac{ik\left(\sqrt{z^2+a^2}+z\right)}{2}}\right] \tag{A.2}$$

The “COMPLEX” function in excel is used in order to get an expression of the form a+ib. Then the function “IMREAL” is used to extract the real part of the equation, which is then used to plot the on-axis normalized pressure. The z values are set up to increase by 0.5 mm, but the values obtained in Table A.2 are also incorporated. The “COMPLEX” function in Excel does not allow the user to set a number of significant digits. The significant digits of the “IMREAL” function are set to three in order to identify the true maximum, where the value is equal to 1. Due to the large number of rows contained in Table A.3, some were removed, noted by […], so that the table would fit in two pages. The nulls and maximums obtained in Table A.2 are highlighted in yellow.

Table A.3. Calculation of the normalized on-axis pressure at various Z values

| z (mm) | normalized P — “COMPLEX” function | “IMREAL” function |
|---|---|---|
| 0 | 0.336008357027486+33215315408842200i | 0.336 |
| 0.03 | -0.0150756094890981+33271767945067600i | -0.015 |
| 0.16 | -0.999002063586175+34858063412597600i | -0.999 |
| 0.31 | 0.0491294744803736+39801706636755200i | 0.049 |
| 0.45 | 0.999053683060633+48579601321879000i | 0.999 |
| 0.5 | 0.892950886394203+53082177636959900i | 0.893 |
| 0.61 | 0.0127892275352044+66603396713232900i | 0.013 |
| 0.78 | -0.999840096792898+102942379901162000i | -1.000 |
| 0.96 | 0.0340189111230096+181986178690195000i | 0.034 |
| 1 | 0.36342675860861+209616421865978000i | 0.363 |
| 1.15 | 0.99975469929773+372980571563962000i | 1.000 |
| 1.35 | 0.0298368496011116+896998624477290000i | 0.030 |
| 1.5 | -0.858138932642408+1872124379489750000i | -0.858 |

| | | |
|---|---|---|
| 1.58 | -0.999999420604519+2844445093501510000i | -1.000 |
| 1.83 | 0.0092061953368324+11726581149931100000i | 0.009 |
| 2 | 0.83837098763852+335709039793644000000i | 0.838 |
| 2.11 | 0.999677753693404+686998429083820000000i | 1.000 |
| 2.42 | -0.012935477473936+5933109003536120000000i | -0.013 |
| 2.5 | -0.375012401828543+1.06718269400044E+21i | -0.375 |
| 2.77 | -0.999860676240866+8.41805312494909 E+21i | -1.000 |
| 3 | -0.632364822775992+5.36925605687238E+22i | -0.632 |
| 3.19 | 0.003029437300208+2.63001392089907E+23i | 0.003 |
| 3.5 | 0.854238372330914+3.88710893206892E+24i | 0.854 |
| 3.68 | 0.999985312117569+1.95519129113848E+25i | 1.000 |
| 4 | 0.641434242127581+3.7516130346906E+26i | 0.641 |
| 4.28 | 0.00327768963207091+5.3729573708365E+27i | 0.003 |
| 4.5 | -0.476741013352123+4.54732213752233E+28i | -0.477 |
| 5 | -0.998067205463413+6.60965927316313E+30i | -0.998 |
| 5.03 | -0.999979290584048+8.95519618479711E+30i | -1.000 |
| 5.5 | -0.694196239459737+1.11174619126629E+33i | -0.694 |
| 6 | -0.0200216404026551+2.10499850575899E+35i | -0.020 |
| 6.01 | -0.00612880958835274+2.34020207009676E+35i | -0.006 |
| 6.5 | 0.589422753053528+4.39123356061016E+37i | 0.589 |
| 7 | 0.932276724241598+9.92404288520842E+39i | 0.932 |
| 7.36 | 0.999998899758606+5.12706395388411E+41i | 1.000 |
| 7.5 | 0.991107794788499+2.39753373140221E+42i | 0.991 |
| 8 | 0.835920648130721+6.12618397795098E+44i | 0.836 |
| 8.5 | 0.556167683315065+1.64149714016043E+47i | 0.556 |
| 9 | 0.22822228150888+4.58025761799747E+49i | 0.228 |
| 9.35 | -0.000394576311768628+2.40974749601411E+51i | 0.000 |
| 12.62 | -0.99999990398386+5.19328370255697E+67i | -1.000 |
| […] | […] | […] |
| 19.09 | -0.000334383327645218+5.0198958330092E+100i | 0.000 |
| 19.5 | 0.0648135837951281+6.39507624448895E+102i | 0.065 |
| […] | […] | […] |
| 35 | 0.988600792488728+7.46131547345101E+182i | 0.989 |

| | | |
|---|---|---|
| 35.5 | 0.991948893604963+2.91145709028395E+185i | 0.992 |
| 36 | 0.994649545763962+1.1368288278149E+188i | 0.995 |
| 36.5 | 0.996750130920852+4.44178610818036E+190i | 0.997 |
| 37 | 0.99829471851275+1.73654844362775E+193i | 0.998 |
| 37.5 | 0.999324296385077+6.79316670487158E+195i | 0.999 |
| 38 | 0.99987698677073+2.65891045183897E+198i | 1.000 |
| 38.38 | 0.999999999507312+2.48463328920594E+200i | 1.000 |
| 38.5 | 0.999988247959355+1.04129000211322E+201i | 1.000 |
| 39 | 0.999691062347686+4.08006608586716E+203i | 1.000 |
| 39.5 | 0.999016111591039+1.59949035254448E+206i | 0.999 |
| 40 | 0.997991939586516+6.27345552406512E+208i | 0.998 |

When expanding the significant digits, only at z=38.38 does p stay equal to 1.0000000

With the Z and pressure values known, graphs such as the ones pictured in Figure 25 and Figure 43 can be plotted. Figure A. 2 shows the graph obtained for CFRP at 10 MHz.

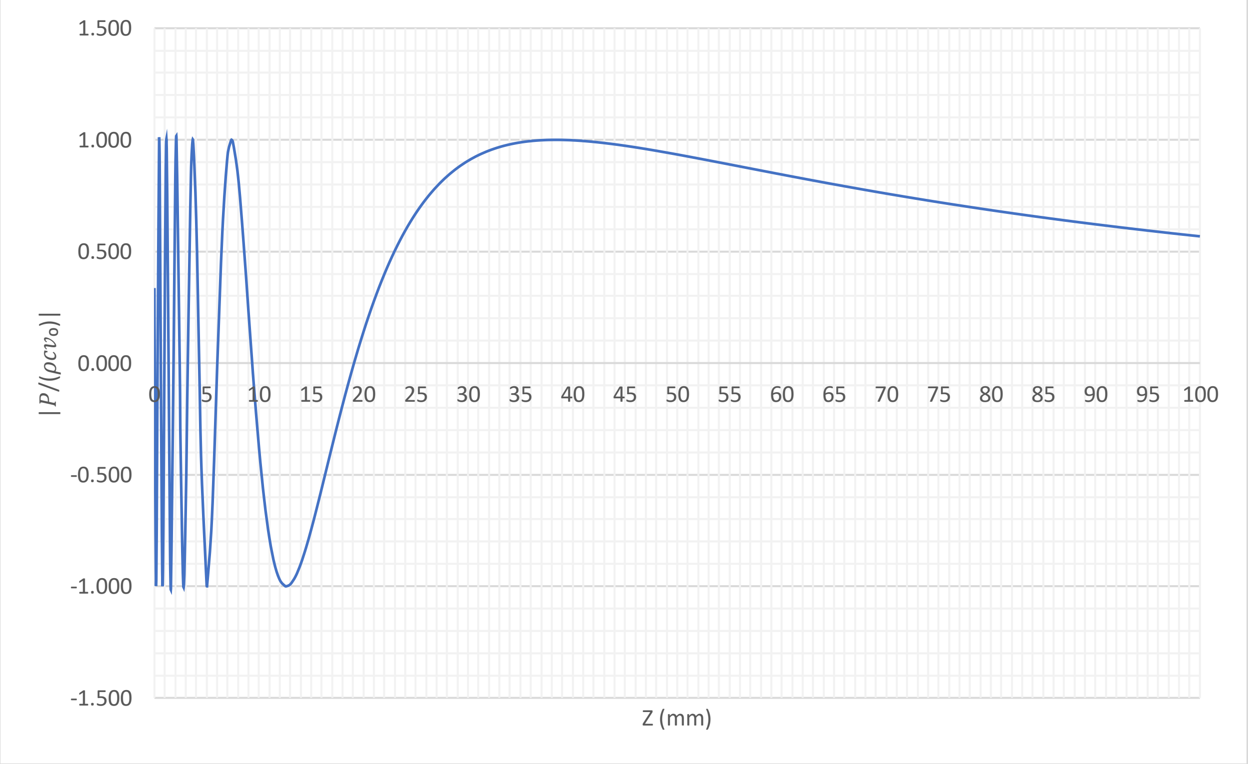

Figure A. 2. Magnitude of the normalized on-axis Pressure for a Plane Piston Transducer in CFRP, f = 10 MHz.

The same method was used to obtain Figure 43, except that the material constants were changed at the appropriate depths to reflect what was happening inside the lap joint. Note that the Y-Axis is only |P|, as the other terms are material specific. Therefore equation A.1 was used to calculate the pressure. The equation for the particle oscillation speed, $v_0$, was obtained in reference [79] and is defined as:

$$v_0 = \frac{p}{c} \frac{k^2 z^2 + 1}{k^2 z^2 + ikz} \tag{A.3}$$

Where p is the pressure calculated in Table A.2, z is from Table A.3, k is the wave number introduced as one of the constants, ρ is the density of the material and c is the speed of sound in the material.

# Appendix 3. Attenuation Coefficients

This appendix explains in greater details the steps shown in Section 6.2. To obtain the attenuation coefficient based on experimental data, an A-Scan must be imported in Excel and set as a plot area. After that, the axes are set to match the ones from the A-Scan. Using this axis, coordinates for each back wall echo can be obtained and plotted on the A-Scan. Figure A. 3 shows the A-Scan of CFRP at 10 MHz, with the peak amplitudes and TOFs, while Table A.4 is used to convert TOFs in distance travelled with equation 4.28.

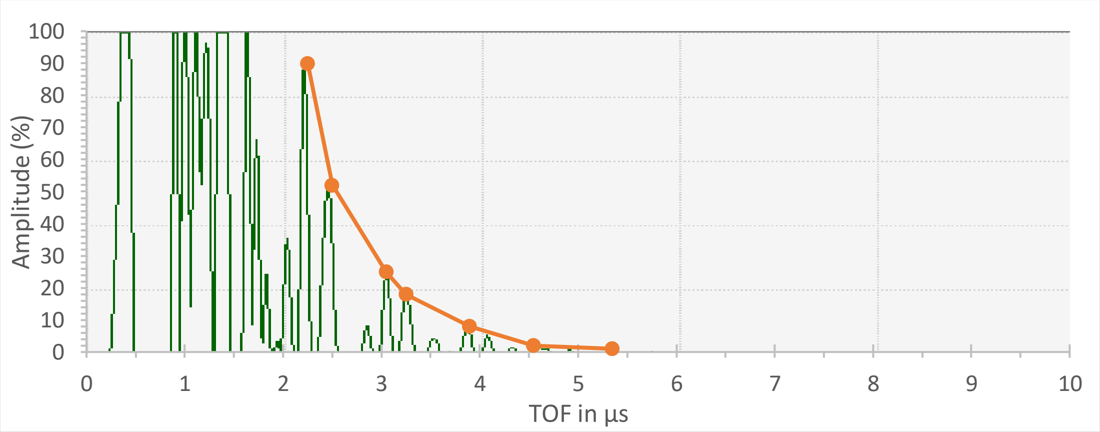

Figure A. 3. Peak amplitude and TOFs extracted from an A-Scan.

Table A.4. Calculation of the distance travelled d, from TOFs obtained on an A-Scan

| Amplitude ±1% | TOF ± 1.5% | Z (cm) ±1.5% |
|---|---|---|
| 90 | 2.25 | 0.29475 |
| 52 | 2.5 | 0.3275 |
| 25 | 3.05 | 0.39955 |
| 18 | 3.25 | 0.42575 |
| 8 | 3.9 | 0.5109 |
| 2 | 4.55 | 0.59605 |
| 1 | 5.35 | 0.70085 |

These two steps were repeated for each A-Scan, at each frequency. All amplitudes and distances Z were then put together, and imported in MATLAB as column vectors called “Amplitude” and “zcm”. The function cftool (zcm, Amplitude) was then called, yielding the graphs shown in Figure 47.